FUNDAMENTAL STUDIES OF THE MECHANISMS AND APPLICATIONS OF FIELD-INDUCED DROPLET IONIZATION MASS SPECTROMETRY AND ELECTROSPRAY MASS SPECTROMETRY

Thesis by

Ronald L. Grimm

In Partial Fulfillment of the Requirements

for the Degree of

Doctor of Philosophy

CALIFORNIA INSTITUTE OF TECHNOLOGY

Pasadena, California

2006

(Defended August 25, 2005)

Acknowledgements

I thank everyone. That’s right. Everyone.

Abstract

This thesis explores the evaporation and Rayleigh discharge dynamics of highly charged micron-sized droplets and explores new methodologies for extracting ions for mass analysis from neutral droplets using strong electric fields in a technique termed field-induced droplet ionization.

A phase Doppler anemometer characterizes individual highly charged droplets moving through a uniform, mild electric field within an ion mobility cell according to size, velocity, and charge. Repeated reversals of the electric field allow multiple characterizations on selected droplets. This “ping-pong” technique provides droplet histories that determine the solvent evaporation and Rayleigh discharge behavior. The ping-pong experiment characterizes volatile droplets of the hydrocarbon solvents *n*-heptane, *n*-octane, and *p*-xylene as well as two-component droplets of either 2-methoxyethanol, *tert*-butanol, or *m*-nitrobenzyl alcohol with methanol. On average, hydrocarbon droplets eject 18% of their net charge into progeny droplets with an undetectable loss in mass. Rayleigh discharge events in the polar, binary droplets release between 20 and 35% of the net charge with a correspondingly undetectable loss in mass.

In other experiments, strong electric fields elongate neutral droplets along the field axis. Field-induced droplet ionization (FIDI) occurs at sufficient field strengths as the droplets eject opposing jets of positively and negatively charged progeny droplets. Images of droplets from a vibrating orifice aerosol generator illustrate this phenomenon, and mass spectrometric sampling of the progeny droplets demonstrates that they are a viable source of desolvated gas-phase ions. Switched electric field experiments relate the timescale of droplet elongation and progeny droplet formation in FIDI to the timescale of oscillations of droplets in sub-critical field strengths. FIDI mass spectra are presented for several species, including tetraheptyl ammonium cation, deprotonated benzene tetracarboxylic acid, and multiply protonated cytochrome *c*.

Droplets may serve as reactors before being sampled by FIDI-MS. FIDI-MS probes the products of heterogeneous reactions between solution-phase oleic acid or a lysophosphatidic acid and gas-phase ozone.

Table of Contents

Appendices

List of Figures

1

2

3

4

5

6

7

8

A

B

List of Tables

2

3

4

5

List of Schemes

8

List of Abbreviations and Terms

EDB	electrodynamic balance
ESI	electrospray ionization
FIDI	field-induced droplet ionization
ICR	ion cyclotron resonance (Typically used in conjunction with MS, i.e. ICR-MS)
IMS	ion mobility spectrometer (instrument context) *or* ion mobility spectrometry (technique context)
LCQ	An ion trap mass spectrometer employed by the Beauchamp group
MS	mass spectrometer (instrument context) *or* mass spectrometry (technique context)
PDA	phase Doppler anemometer (instrument context) *or* phase Doppler anemometry (technique context)
LPA	lysophosphatidic acid Lysophosphatidic acid is a general term for a class of compounds having a similar formula and biological role. This thesis only considers oleoyl-L-a-lysophosphatidic acid.

Chapter 1. Introduction

1.1. Overview

In the past twenty years, charged droplets and strong electric fields have quietly revolutionized chemistry. In combination with an atmospheric-sampling mass spectrometer, charged droplets containing biomolecules or polymers become a source for desolvated, gas-phase ions of these analytes. The process by which charged droplets evaporate is remarkably "soft" in that the process imparts little to no energy to the resulting ions. This thesis explores two techniques for generating these charged droplets. One technique, electrospray ionization (ESI), is commonly employed for biomolecule mass analysis. In the second technique, jets of charged progeny droplets are emitted from neutral parent droplets in strong electric fields in a process we call field-induced droplet ionization, or FIDI.

A cartoon of the electrospray process is shown in Figure 1.1. Here an analyte-containing liquid is pumped through a capillary needle. A high voltage source establishes an electric field between the needle and a plate. Sufficiently high voltages produce strong fields within the liquid itself drawing the liquid to a tip as it exits the needle. From this tip, the liquid sprays outward as charged droplets that are accelerated in the electric field toward the plate. When the plate contains an inlet to a mass spectrometer, analyte within the charged droplets may be mass analyzed.[1] Although Malcolm Dole is commonly credited with the first application of electrospray to mass spectrometry in the

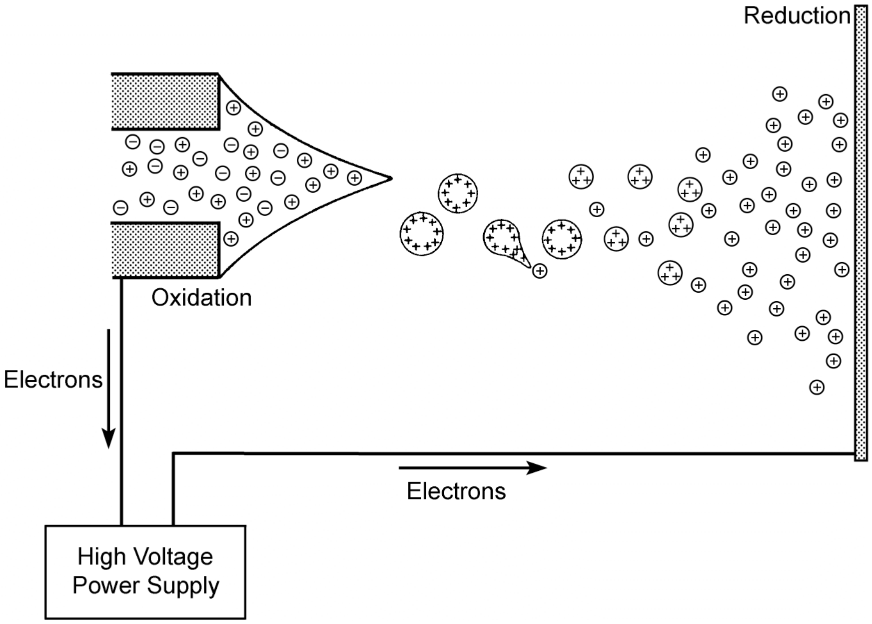

Figure 1.1. Electrospray ionization cartoon. A high voltage power supply establishes an electric field between a solution-filled capillary and a counter electrode. As the liquid is pushed through the capillary, ion migration draws the liquid to a tip that emits a fine spray of charged droplets.

1960s, two decades would pass before the technique would gain wide acceptance. In the 1980s John Fenn and coworkers revolutionized the field of mass spectrometry by making electrospray easy and practical for the analysis of large biomolecules and polymers.[1] Fenn's contributions to the body of knowledge surrounding electrospray culminated in his sharing of the 2002 Nobel prize in chemistry.

Despite the widespread popularity of ESI-mass spectrometry, questions remain regarding the mechanism by which the charged droplets evaporate to ultimately produce gas-phase ions. A more thorough understanding will certainly lead to more efficient ion sources and further unique applications.

Figure 1.2 highlights the current understanding of the "life" of an evaporating charged droplet. Initially, nascent droplets evaporate, losing solvent molecules but not charge. As a result, the surface charge density increases to a point at which the force of Coulomb repulsion at the surface overcomes the cohesive force of surface tension. The droplet releases charge and mass in a concerted "Rayleigh discharge" named after Lord Rayleigh who first predicted the event.[2] Smaller droplets release ions by a mechanism alternatively described by the ion evaporation model and the charge residue model. From there, nanoclusters of solvent and analyte undergo further evaporation yielding desolvated gas-phase ions.

Chapter two summarizes previous research on Rayleigh discharge phenomena in the context of understanding the mechanism of electrospray ionization. Additionally, chapter two discusses how the evaporation and discharge dynamics research presented in later chapters supplements existing research. Previous studies in the Beauchamp group

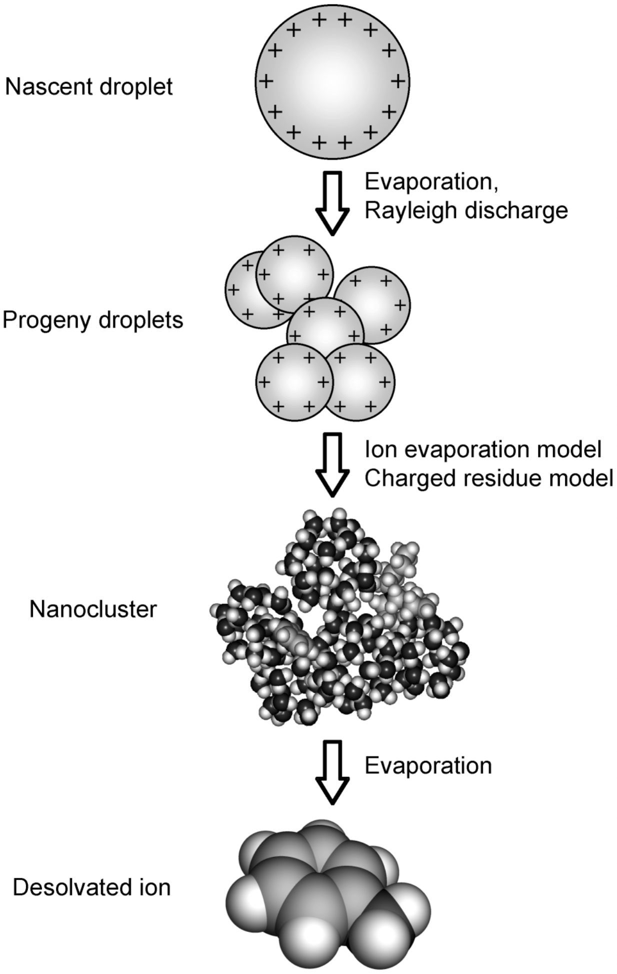

Figure 1.2. Schematic representation of the "life" of an evaporating, charged droplet.

into Rayleigh discharge phenomena focused on traditional solvents employed for electrospray ionization, specifically water, methanol, and acetonitrile.[3,4] This work expands this research by considering nontraditional hydrocarbon solvents and specific binary solvents typically involving methanol and a lower vapor pressure constituent. In this research, solvents are electrosprayed into an ion mobility cell. Within the cell a rapidly reversing electric field allows a phase Doppler anemometer to repeatedly sample the physical characteristics of the charged droplets generated by electrospray. The instrumentation employed for these studies is virtually identical to the original designs and discussed in chapter three. Chapters four and five present the results and implications from the hydrocarbon solvents and the binary solvents, respectively.

While researching Rayleigh discharge phenomena in the literature, our attention was drawn to studies of *neutral* droplets in strong electric fields that were performed between 1917 and Malcolm Dole's original electrospray experiments. Early researchers noted that a strong electric field will cause jetting similar to that seen in electrospray ionization. In the case of a neutral droplet, two opposing jets are observed as shown in Figure 1.3. This figure represents the jetting from a small methanol droplet acquired in preliminary research in our laboratory.

We postulated that such jets might also be a source of charged droplets that would similarly evaporate and discharge to yield gas-phase ions suitable for mass analysis. Indeed, initial studies confirmed that neutral droplets in strong electric fields are a source of gas-phase ions through a process we call field-induced droplet ionization. Chapter Six presents the initial work performed on methanol droplets containing small organic salts,

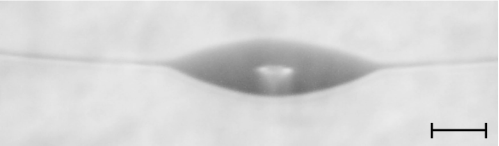

Figure 1.3. Image of a single methanol droplet subjected to a strong electric field. The field destabilizes the droplet resulting in the formation of two opposing conical jets. The bar indicates 100 μm. Adapted from Grimm and Beauchamp.[5]

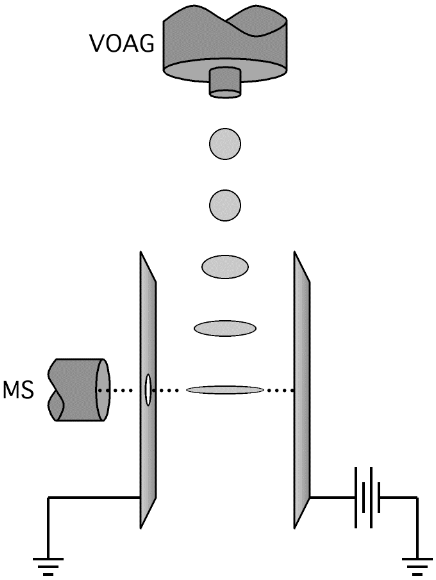

Figure 1.4. Experimental arrangement for FIDI-MS. A vibrating orifice aerosol generator (VOAG) generates a stream of droplets that pass between two parallel plate electrodes. A strong field between the electrodes causes field-induced droplet ionization and jetting of charged progeny droplets that are directed at the capillary inlet of a mass spectrometer for analysis. Adapted from Grimm and Beauchamp.[5]

organic acids, and the protein cytochrome *c*. Here, FIDI-mass spectrometry was accomplished with a relatively simple experimental arrangement shown in Figure 1.4. In this setup a stream of methanol droplets pass between two electrodes that define a region of high electric field. The field elongates the droplets, which eject jets of charged progeny droplets that are directed into the capillary inlet of a mass spectrometer. The resulting mass spectra are consistent with those acquired from a conventional electrospray ionization source.

Following the initial mass spectrometry studies, we developed an experiment to explore the parameter space associated with FIDI in an attempt to better understand and control the technique. Chapter Seven documents the use of switched electric fields for time-resolved studies of the droplet distortion, jetting, and charged progeny droplet formation associated with FIDI. Custom designed high voltage switching circuitry, a high speed flashlamp, and a digital camera-equipped microscope captured sequences of droplets such as those shown in Figure 1.5. These sequences allowed us to observe the nature of FIDI as a function of field strength, exposure duration, and the physical parameters of the droplets studied.

Understanding the dynamics of the process allowed us to develop a practical, single droplet FIDI source. Unlike the initial studies presented in Chapter Six, the single droplet source is an optimized design playing to the natural strengths of FIDI. Because the droplet can be exposed to the atmosphere for a controlled period of time before FIDI, the ability to explore heterogeneous chemistry occurring between components in the atmosphere and analytes within the droplet is a natural strength of the technique.

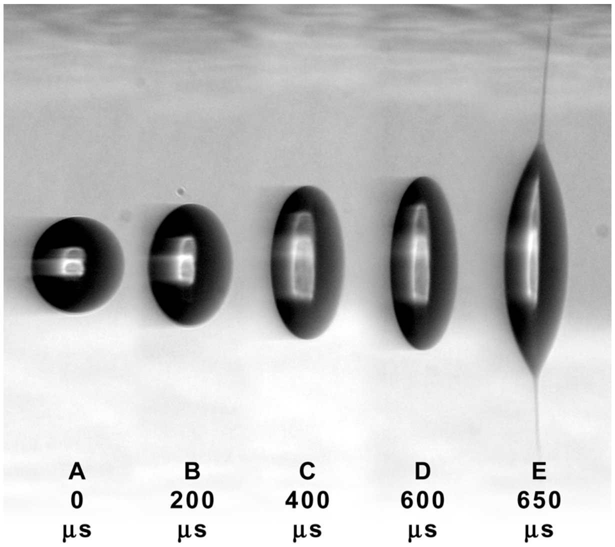

Figure 1.5. Sequence of methanol droplets exposed to a strong electric field for the time indicated in each panel. In this case, FIDI occurs after 650 μs for this field strength and droplet size.

Chapter eight explores the application of single droplet FIDI-MS applications to heterogeneous reaction chemistry between gas phase ozone and solution phase oleic acid and oleoyl-L-α-lysophosphatidic acid, or LPA (18:1). Each of these organic acids contains a carbon-carbon double bond that reacts with ozone in a heterogeneous reaction. When sampled at multiple reaction lengths, the ozone / oleic acid products show a successively increasing ratio between products and reactants indicating that FIDI-MS is a viable technique for kinetic studies of heterogeneous reactions in microdroplets. Reactions between ozone and LPA produce species that unambiguously and correctly localize the position of the double bond along the hydrocarbon chain.

Finally, the appendices present design details and circuit diagrams as an operations manual for constructing and using a single droplet FIDI source (appendix A) and a setup for switched electric field studies of neutral droplets (appendix B).

1.2. References

(1) *Electrospray Ionization Mass Spectrometry*; Cole, R. B., Ed.; John Wiley and Sons: New York, 1997.

(2) Rayleigh, L. *Philos. Mag.* **1882**, *14*, 184.

(3) Smith, J. N. Fundamental Studies of Droplet Evaporation and Discharge Dynamics in Electrospray Ionization, California Institute of Technology, 2000.

(4) Smith, J. N.; Flagan, R. C.; Beauchamp, J. L. *J. Phys. Chem. A* **2002**, *106*, 9957.

(5) Grimm, R. L.; Beauchamp, J. L. *J. Phys. Chem. B* **2003**, *107*, 14161.

Chapter 2. Survey of Previous Research in Charged Particle Dynamics, Droplets in Electric Fields, and Electrospray Ionization

Portions adapted from Grimm, R. L.; Beauchamp, J. L. *J. Phys. Chem. B* **2005**, *109*, 824 and Grimm, R. L.; Beauchamp, J. L. *Anal. Chem.* **2002**, *74*, 6291.

2.1. Introduction

This thesis explores the mechanisms and processes that occur during electrospray ionization as well as explores and develops new applications of field-induced droplet ionization mass spectrometry. Both electrospray and field-induced droplet ionization rely on creating electrical pressure within droplets and liquids. Sufficient electrical pressure drives instabilities and jetting both from charged and neutral droplets as well as liquids flowing from a capillary needle. Within droplets, instability and jetting may be the result of a strong applied electric field, sufficient net charge, or a combination of charge and applied field. The jets that form during these instabilities consist of charged progeny droplets that are a suitable source of desolvated ions for mass analysis.

This chapter reviews the history of electrospray ionization and the subsequent interest in charged droplet instabilities. Although much of the research occurred concurrently, electrospray, evaporation and discharge of highly charged droplets, and electric field-induced droplet ionization are separated for clarity. Section 2.2 presents a historical perspective of electrospray ionization from early experiments with blood through John Fenn's 2002 Nobel prize in chemistry. Understanding the dynamics of charged droplets is paramount to knowing how charged droplets produced by electrospray ultimately yield desolvated, gas-phase ions. Section 2.3 summarizes 120 years of charged droplet research from Lord Rayleigh's initial theories to recent work performed in the Beauchamp group.

Field-induced droplet ionization mass spectrometry (FIDI-MS) fundamentally depends on the behavior and response of a droplet to the application of an external electric field. In FIDI-MS an applied electric field elongates a neutral or lightly charged droplet parallel to the field, ejecting opposite jets of positively and negatively charged progeny droplets. These progeny droplets are directed into the atmospheric sampling capillary inlet of a mass spectrometer where dissolved analytes are mass analyzed. The behavior of neutral droplets in high electric fields is therefore critical to understanding FIDI. A history of the experiments and theoretical investigations on the topic are presented in section 2.4. Finally, section 2.5 discusses outstanding issues and avenues of future research related to charged droplet instability and field-induced droplet ionization.

2.2. A brief history of electrospray ionization

The phenomenon of electrospray was investigated long before it was applied to the study of gas phase ions transferred from solution. In 1750, French clergyman and physicist Jean-Antoine (Abbé) Nollet reported the earliest known reference to electrospray, over two hundred years before the term was coined. He demonstrated that water flowing from a vessel would aerosolize when the vessel was electrified and placed near electrical ground. He also observed that "a person, electrified by connection to a high-voltage generator, would not bleed normally if he were to cut himself; blood would spray from the wound."[1] Roughly one hundred years later, Lord Kelvin designed an apparatus consisting of two liquid nozzles connected to opposite collection reservoirs. Small statistical differences in charging between water dripping from the nozzles quickly led to kilovolt differences and electrosprays at the nozzles.[2]

In the early twentieth century, refined experimental techniques allowed for a more rigorous understanding of electrostatics and electrodynamics. John Zeleny classified the formation of ethanol electrosprays through photographs reprinted in Figure 2.1.[3] The sprays characterized in Zeleny's work are structurally similar to those employed for mass spectrometry today in which liquid is drawn into a conical shape before breaking into a fine mist of droplets. This work was followed by rigorous studies of the field-dependent deformation of soap films over cylindrical tubes by Wilson and Taylor. The conical shape of these films resembled Zeleny's observations of ethanol and indeed has come to be termed the Taylor cone based on later theoretical work by G. I. Taylor.[4,5]

By the middle of the twentieth century, electrospray had become a popular painting technique. Reports by Hines,[6] Tilney and Peabody,[7] and several patents demonstrate the ease with which paint is atomized and applied to vehicles, housewares, and various metal goods. However, it was not until 1968 that electrospray was introduced as a scientific tool. Dole and coworkers transferred high molecular weight polystyrene ions into the gas phase from a benzene/acetone solution.[8] They introduced the combination of electrospray and nozzle skimmer/pumping systems similar to those employed today to transfer the charged species from atmospheric pressure into the vacuum system for analysis. Although a revolutionary technique, Dole did little to develop electrospray into a rigorous experimental methodology.

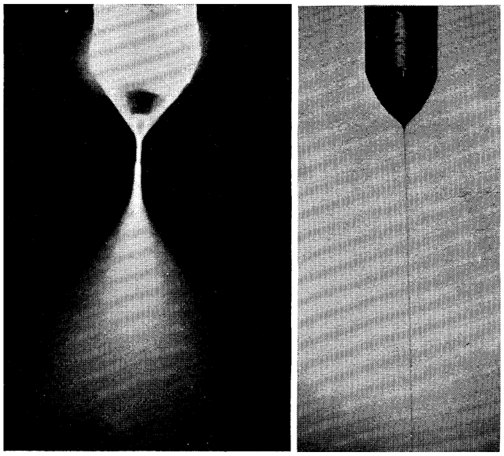

Figure 2.1. Early photographs of ethanol electrosprays. Reprinted Figure 5 and 7 with permission from Zeleny, J. *Phys. Rev.* **1917**, *10*, 1.[3] Copyright 1917 by the American Physical Society.

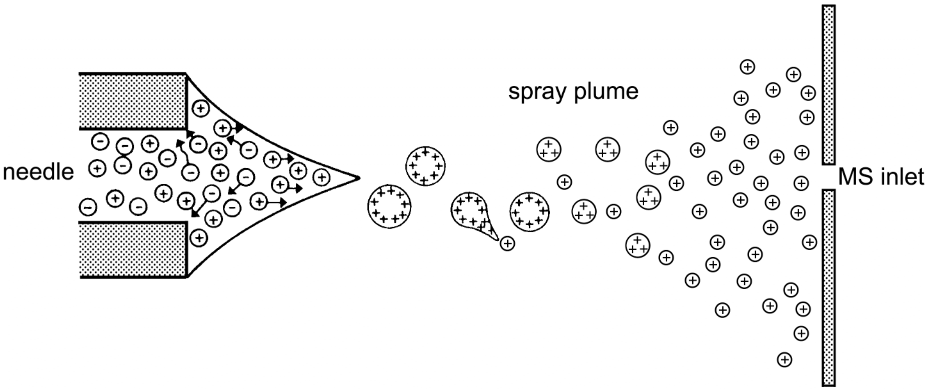

Figure 2.2. Electrospray ionization-mass spectrometry schematic. A high voltage power supply (not shown) establishes an electric field between a solution-filled capillary needle and the mass spectrometer inlet. As the liquid is pushed through the capillary, ion migration draws the liquid to a tip that emits a fine spray of charged droplets. These droplets are directed to an atmospheric-sampling inlet of a mass spectrometer for analysis.

In the 1980's, Fenn and coworkers presented a series of papers that permanently established electrospray as a tool to introduce dissolved analytes into the gas phase for mass analysis. Figure 2.2 shows a schematic cartoon of the electrospray ionization arrangement for mass spectrometry. Electrospray generates charged droplets that are directed towards a capillary sampling inlet of a mass spectrometer for analysis of the dissolved species in the sprayed solution. Their work attracted significant attention through spraying compounds of ubiquitous scientific interest including low molecular weight cationic clusters,[9] negative ions,[10] polyethylene glycol,[11] and several biomolecules.[12] They noted that electrospray imparts multiple charges to large biomolecules and polymers thus lowering the m/z value allowing biomolecule analysis on mass spectrometers having only a modest m/z range. ESI-MS has become a popular tool for studying noncovalent interactions and characterizing biomolecules. Cole reviews the present state and the diverse applications of electrospray ionization.[13]

2.3. Investigations of the behavior of highly charged droplets

The application of electrospray to mass spectrometry by Fenn and coworkers and its subsequent popularity renewed an interest in the process by which charged droplets yield desolvated, gas-phase ions. Because ESI generates charged droplets that ultimately produce gas-phase ions, understanding the processes that govern charged droplet breakup and evaporation is critical for understanding and refining ESI as well as its application to mass spectrometry.

2.3.1. Rayleigh's original conjectures regarding charged droplets

In 1882, Lord Rayleigh first considered the electrical pressure resulting from excess charge q on a droplet of spherical radius r and surface tension σ. His theory predicts that the natural quadrupolar oscillation of a droplet in a field-free environment becomes unstable when q exceeds the limit q_{R}, now known as the "Rayleigh limit", defined in equation (2.1).

$$q_{\mathrm{R}} = 8\pi\varepsilon^{1/2}\sigma^{1/2}r^{3/2} \qquad (2.1)$$

The limit is reached either by evaporation or by application of charge in excess of q_{R}. At $q \geq q_{\mathrm{R}}$, Rayleigh postulated that the droplet would throw out liquid in fine jets.[14] This event is referred to in the literature as Rayleigh discharge[15,16] or Coulomb fission.[17] Despite a rigorous prediction of when the event occurs, Rayleigh's analysis does little to describe the dynamics of the discharge event.

2.3.2. Modern research on Rayleigh discharge phenomena

Recent articles by Cole[18] and by Kebarle and Peschke[19] summarize the research performed to elucidate the dynamics not described by Rayleigh's analysis. Figure 2.3 presents a cartoon summary of the "lifetime" of a charged droplet. In the consensus view, charged, micrometer-sized droplets eject numerous progeny droplets having a diameter roughly one-tenth that of the parent. Other experiments and models such as the ion desorption model and the charge residue model address phenomena involving smaller droplets in the nanometer regime not considered in this thesis. Ultimately the result of ion desorption or the charge residue mechanism is a desolvated ion, or in some cases an ion-bound water cluster.[20]

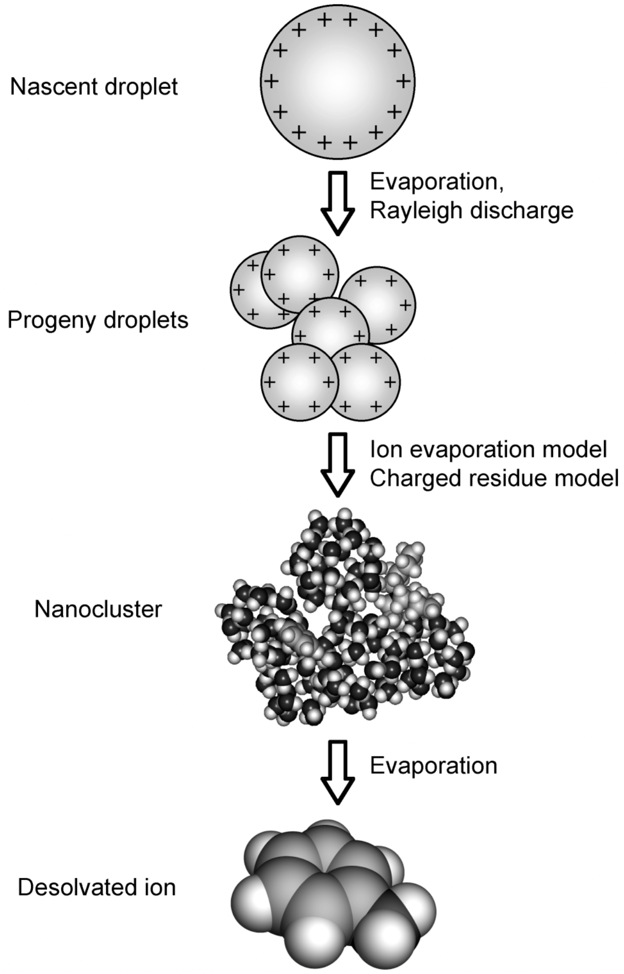

Figure 2.3. Cartoon depiction of the process by which a charged, analyte-containing droplet yields a desolvated, gas-phase ion. This thesis presents research into the Rayleigh discharge phenomenon shown in the first stage of charged droplet dynamics.

Table 2.1 summarizes the conclusions of Rayleigh discharge experiments found in the literature. This list is not inclusive, but rather shows the breadth and scope of the studies and their conclusions. Charged droplets generally undergo Rayleigh discharge while they are at 70-120% of their Rayleigh limit of charge. For instance, Taflin and co-workers found discharge occurring below 90% the Rayleigh limit with charge loss ranging from 10 to 18%, and 1-2% mass loss in dodecaonol, hexadecane, heptadecane, dibromooctane, and bromodecane.[21]

High speed photography by Gomez and Tang support the prevailing theories of Rayleigh discharge. Figure 2.4 shows a charged droplet undergoing jetting in an event attributed to Rayleigh discharge. In this event, it is clear that the parent is elongating and emitting a series of fine progeny droplets. Although they did not measure the charge lost during Rayleigh discharge, they noted the occurrence at ~60 to 80% the Rayleigh limit, and the photograph supports other experimental findings of little mass loss.[22]

More recently, Duft and co-workers explored Rayleigh discharge through accurate measurements of the quadrupolar oscillations in a droplet suspended in an alternating current electric field. Through a calculation of the Coloumb energy and surface energy of a droplet, they determined that ethylene glycol undergoes discharge at 100% q_R without reliance on the bulk surface tension parameter σ to determine q_R.[23] Recent studies in our laboratory focused on the more common electrospray solvents water, methanol, and acetonitrile. This work was performed in a mobility cell with an axial, linear electric field. Thus no field counteracts radial drift. Droplets are measured in a small measurement volume and the electric field reverses following measurement

Author(s)	Solvent	Location	Droplet Diam. (μm)	% q/q_{R} at Rayleigh Discharge	Percent Mass Lost	Percent Charge Lost
Li, Tu, and Ray, 2005[24]	diethyl phthalate	balance	5-25	96	2.3	21
	diethylene glycol			100	< 0.3	38
	triethylene glycol			100	< 0.3	41
	hexadecane			97	1.5	15
Duft et al., 2003[25]	ethylene glycol	balance	48	100	0.3	33
Duft et al., 2002[23]	ethylene glycol	balance	3-25	> 95	n/a	~25
Smith, Flagan, and Beauchamp, 2002[15]	water	IMS	10-60	100	n/a	20-40
	methanol			120		15-20
	acetonitrile			100		15-20
Feng et al., 2001[26]	methanol	balance	20-42	~ 100	n/a	80
Widmann et al., 1997[27]	50 BTD, 50 IDD	balance	25-30	3	24	21
	50 BTD, 50 IDD		17-28	3	75	74
	hexanediol diacrylate		22	64	n/a	n/a
Gomez, Tang, 1994[22]	heptane	ESI plume	32-80	60-80	n/a	n/a
Richardson et al., 1989[28]	*n*-octanol	balance	1-10	102	2.3	15
	sulfuric acid		1-10	84	< 0.1	49
Taflin, Ward, and Davis, 1989[21]	bromododecane	balance	44	72	n/a	12
	dibromooctane		26-40	86	1.8	16
	dibutyl phthalate		20	75	n/a	n/a
	docecanol		36-38	85	2	15
	hexadecane		28-64	73	1.6	17
	heptadecane		28-36	79	1.6	12
Roulleau et al., 1972[29]	water	balance	50-200	~100	n/a	n/a
Schweizer et al.,1971[30]	*n*-octanol	balance	15-40	~100	5	23
Berg et al., 1970[31]	balance	balance	30-250	25-100	n/a	n/a
Ataman et al., 1969[32]	*n*-octanol	balance	30-60	~100	n/a	n/a
Doyle, et al., 1964[33]	n/a	balance	60-200	n/a	n/a	30

Table 2.1. Survey of Rayleigh discharge studies from the literature. Abbreviations: BTD: 1-bromotetradecane, IDD: 1-iodododecane, IMS: ion mobility cell, balance: electrodynamic balance, ESI: electrospray ionization, n/a: not available. Superscripts refer to the references at the end of this chapter.

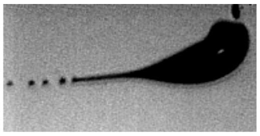

Figure 2.4. Instability and jetting from a charged heptane droplet within an electrospray plume. Reprinted with permission from Gomez, A.; Tang, K. *Phys. Fluids* **1994**, *6*, 404.[22] Copyright 1994, American Institute of Physics.

allowing multiple characterizations and the development of a time profile of droplet size and charge. That droplets are repeatedly characterized in a small measurement volume before and after Rayleigh discharge suggests a “soft” event in which little, if any, momentum is imparted to the parent droplet. This work also suggests a solvent dependence on the charge loss and the percent Rayleigh limit at discharge.[2,15]

2.4. Droplet instabilities driven by an applied electric field

Concurrent with investigations into the electrospray phenomenon, investigators considered the behavior of strong electric fields on *neutral* water droplets. In this case the applied electric field drives droplet instability rather than the charge repulsion due to a net surface charge. Early researchers saw meteorological implications and sought to understand how fields within clouds would affect rain and aerosol drops. In a classic 1931 experiment, Macky dropped ~1 to 5 mm diameter water droplets through a strong electric field with the apparatus shown in Figure 2.5A. Here a voltage difference between plates (i) and (ii) defines a high electric field. Water droplets are produced from reservoir (iii) through a stopcock (v) and field-free region (iv).

Macky observed that strong electric fields caused droplets to elongate into spheroids prolate to the electric field. At a critical field strength E_c^0, droplets developed instabilities resulting in the formation of two symmetrical fine filaments from opposing sides of the droplet. Figure 2.5B shows this elongation and instability in photographs of 5 mm diameter water droplets exposed to a 8250 V cm^{-1} electric field.

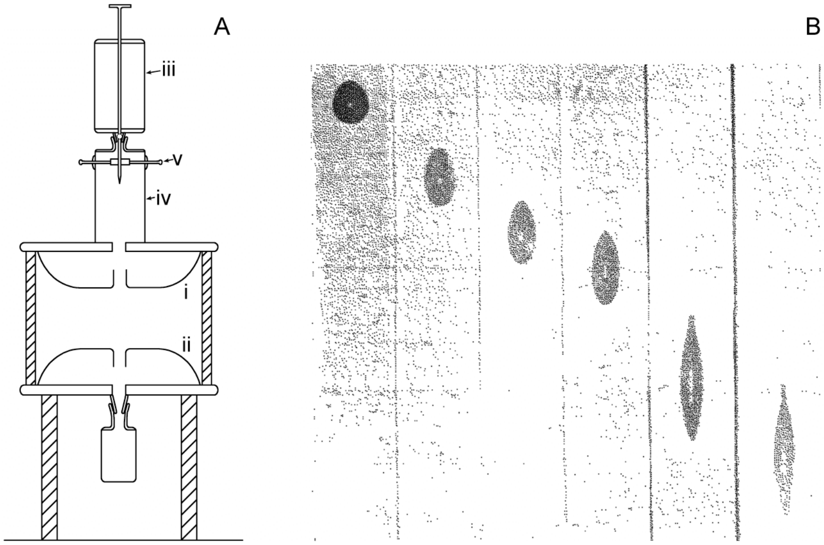

Figure 2.5. Early experimental apparatus (A) and photographs of droplets in strong electric fields (B). Adapted with permission from Macky, W.A. *Proc. Roy. Soc. A* **1931**, *133*, 565. Copyright 1931, the Royal Society.[34]

Macky[34] and other researchers[35,36] noted the relationship between the critical electric field necessary to induce an instability and jetting in neutral droplets was proportional to the square root of σ/r as denoted in equation (2.2).

$$E_c^0 \propto \sigma^{1/2} r^{-1/2} \tag{2.2}$$

This critical limit has become known as the “Taylor limit of field”, or simply “Taylor limit” after Geoffrey Taylor who pioneered the corresponding theory in 1964. He refined the general relationship proposed in (2.2) to the formalized equation (2.3).

$$E_c^0 = \frac{c}{(8\pi)^{1/2}} \left(\frac{2\sigma}{\varepsilon_0 r} \right)^{1/2} \tag{2.3}$$

In equation (2.3), the empirical fitting constant *c* has been determined both experimentally[34-37] and theoretically,[4] and the accepted value is 1.625 for liquid droplets in air. Assuming droplets always distort into spheroidal shapes, Taylor additionally derived (2.4) and (2.5), the general relationship between an applied electric field $E < E_c^0$ and the resulting aspect ratio $\gamma = a / b$ of the major to minor axis of the spheroid.[4]

$$E = I_2 \gamma^{-4/3} \left(2 - \gamma^{-3} - \gamma^{-1} \right)^{1/2} \left(\frac{2\sigma}{\varepsilon_0 r} \right)^{1/2} \tag{2.4}$$

In equation (2.4), the coefficient I_2 is a higher-order function of γ represented by (2.5).

$$I_2 = \frac{1}{2\left(1-\gamma^{-2}\right)^{3/2}} \ln\left[\frac{1+\left(1-\gamma^{-2}\right)^{1/2}}{1-\left(1-\gamma^{-2}\right)^{1/2}} \right] - \frac{1}{1-\gamma^{-2}} \tag{2.5}$$

Equation (2.4) predicts γ increases with increasing E until $\gamma = 1.85$ where the droplet becomes unstable corresponding to $E = E_c^0$. This relationship is supported by experimental and theoretical evidence for neutral droplets and soap films in air.[35,38] Although a simple relation does not exist for $\gamma(E)$ in the spheroidal approximation, equation (2.6) approximates the relationship between γ and E in (2.4) to within 1% for fields less than 55% of the Taylor limit.[39]

$$\gamma(E) = \left(1 + \frac{9r\varepsilon_0 E^2}{16\sigma}\right)\left(1 - \frac{9r\varepsilon_0 E^2}{16\sigma}\right)^{-1} \tag{2.6}$$

Figure 2.6 and Figure 2.7 explore Taylor's spheroidal approximation as applied to droplets relevant to this thesis. Figure 2.6 shows equation (2.4) plotted for 225 μm, 500 μm, and 2.25 mm diameter droplets. Each curve demonstrates that the equilibrium aspect ratio increases with applied field for $0 < E < E_c^0$ and curves inward at higher aspect ratio values. This turning point agrees well with the Taylor limit presented by equation (2.3). At the Taylor limit, the equilibrium aspect ratio is approximately 1.85. Taylor's model was developed through a stability analysis and subsequently fails for higher field values and equilibrium aspect ratios where the droplet is no longer physically stable. Figure 2.6 demonstrates that for a given applied electric field, larger droplets will be more elliptical than smaller droplets and corroborates equation (2.3), which suggests that larger droplets require lower field strengths to become unstable and exhibit jetting.

Figure 2.7 plots the equilibrium aspect ratio for 225 μm diameter droplets of methanol and water. For a specific applied field and droplet size, droplets with a lower surface tension have a greater equilibrium aspect ratio. This plot also shows that 225 μm water droplets do not undergo jetting under standard atmospheric conditions because the necessary field is greater than the 3×10^6 V/m dielectric breakdown limit of air. For this droplet, air will break down and arc before the Taylor limit of field is reached. Indeed, inserting $E_c^0 = 3 \times 10^6$ V/m and $\sigma = 0.072$ N/m into equation (2.3), the smallest water

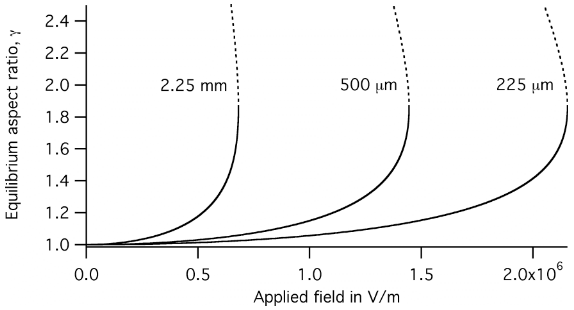

Figure 2.6. Equilibrium aspect ratio versus applied field for methanol droplets of different diameters. Solid lines are physically attainable values for the aspect ratio whereas the dotted lines represent unstable droplet shapes.

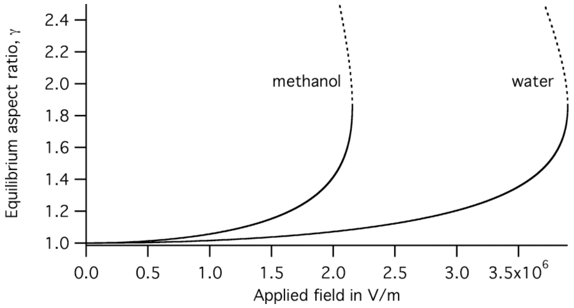

Figure 2.7. Equilibrium aspect ratio as a function of applied field for 225 μm diameter methanol and water droplets.

droplet that demonstrates jetting and FIDI would be ~380 μm in diameter. Practical considerations that lower the breakdown limit of air such as humidity and burrs on the electrodes would most likely raise the minimum water droplet diameter to about 500 μm. Between the Rayleigh limit of charge and the Taylor limit of field exists the general case where excess electrical pressure within a droplet results from both net charge and the externally applied electric field.[38,40,41] Taylor's spheroidal approximation is not as accurate at predicting shapes and critical fields because charged droplets are egg- or tear-shaped, having a higher curvature on the side carrying the net charge.[40] For a droplet of charge q, this shape becomes unstable at a critical electric field, E_c^q, and is characterized by the formation of a single jet from the sharper end.

2.5. Review of unresolved issues in the dynamics of charged droplets and neutral droplets in high electric fields

Research is still needed to develop a complete picture of both electrospray and field-induced droplet ionization mass spectrometry. The physical aspects of Rayleigh discharge have been well studied in the Beauchamp group as well as in the Davis, Agnes, and Leisner laboratories. However, few studies have probed the chemical aspects and implications of charged droplet phenomena. Differing ESI-MS peak heights are rationalized by surface/bulk analyte partitioning in the charged droplets formed by electrospray, but this has not be rigorously proved. Understanding the relationship between solvent and analyte partitioning between the progeny of a Rayleigh discharge and the parent would provide significant insight into the electrospray process and lead to further optimizations of the technique. The Agnes group has begun these studies by using the differential ion mobility within an electrodynamic balance to separate the progeny from the parent. These studies represent the beginning of important investigations that potentially include the characterization of how multiple chemically unique fluorphores partition between the progeny and the parent, mobility studies on multi-component droplets, and mass spectrometric characterization of the progeny relative to the parent droplets.

Similarly, our group has pioneered the use of field-induced droplet ionization as a complimentary technique for transferring analyte molecules from a droplet into a mass spectrometer for analysis. FIDI-MS promises to open new avenues to on-line mass analysis of the progress of chemical reactions within droplets, detection of trace gas-phase species, and mass sampling of a selected droplet from an assembly of multiple droplets. Future work may investigate more efficient mechanisms for directing the charged progeny into the inlet of a mass spectrometer and the subsequent analysis. Additionally, FIDI would benefit from analyses similar to those proposed for charged droplets to develop an understanding of the chemical and physical partitioning of solvent, analyte, and charge carriers between the progeny and the parent.

2.6. References

(1) ORNL Review, State of the Laboratory. vol. 29 no. 1-2 1995. http://www.ornl.gov/info/ornlreview/rev29-12/text/environ.htm (accessed June 16, 2005).

(2) Smith, J. N. Fundamental Studies of Droplet Evaporation and Discharge Dynamics in Electrospray Ionization, California Institute of Technology, 2000.

(3) Zeleny, J. *Phys. Rev.* **1917**, *10*, 1.

(4) Taylor, G. *Proc. R. Soc. London, Ser. A* **1964**, *280*, 383.

(5) Taylor, G. *Proc. R. Soc. London, Ser. A* **1966**, *291*, 159.

(6) Hines, R. L. *J. Appl. Phys.* **1966**, *37*, 2730.

(7) Tilney, R.; Peabody, H. W. *Brit. J. Appl. Phys.* **1953**, *4*, S51.

(8) Dole, M.; Mack, L. L.; Hines, R. L.; Mobley, R. C.; Ferguson, L. D.; Alice, M. B. *J. Chem. Phys.* **1968**, *49*, 2240.

(9) Yamashita, M.; Fenn, J. B. *J. Phys. Chem.* **1984**, *88*, 4451.

(10) Yamashita, M.; Fenn, J. B. *J. Phys. Chem.* **1984**, *88*, 4671.

(11) Wong, S. F.; Meng, C. K.; Fenn, J. B. *J. Phys. Chem.* **1988**, *92*, 546.

(12) Fenn, J. B.; Mann, M.; Meng, C. K.; Wong, S. F.; Whitehouse, C. M. *Science* **1989**, *246*, 64.

(13) *Electrospray Ionization Mass Spectrometry*; Cole, R. B., Ed.; John Wiley and Sons: New York, 1997.

(14) Rayleigh, L. *Philos. Mag.* **1882**, *14*, 184.

(15) Smith, J. N.; Flagan, R. C.; Beauchamp, J. L. *J. Phys. Chem. A* **2002**, *106*, 9957.

(16) Grimm, R. L.; Beauchamp, J. L. *Anal. Chem.* **2002**, *74*, 6291.

(17) Kebarle, P. *J. Mass Spectrom.* **2000**, *35*, 804.

(18) Cole, R. B. *J. Mass Spectrom.* **2000**, *35*, 763.

(19) Kebarle, P.; Peschke, M. *Analytica Chimica Acta* **2000**, *406*, 11.

(20) Lee, S. W.; Freivogel, P.; Schindler, T.; Beauchamp, J. L. *J. Am. Chem. Soc.* **1998**, *120*, 11758.

(21) Taflin, D. C.; Ward, T. L.; Davis, E. J. *Langmuir* **1989**, *5*, 376.

(22) Gomez, A.; Tang, K. *Phys. Fluids* **1994**, *6*, 404.

(23) Duft, D.; Lebius, H.; Huber, B. A.; Guet, C.; Leisner, T. *Phys. Rev. Lett.* **2002**, *89*, art. no. 084503.

(24) Li, K.-Y.; Tu, H.; Ray, A. K. *Langmuir* **2005**, *21*, 3786.

(25) Duft, D.; Atchtzehn, T.; Muller, R.; Huber, B. A.; Leisner, T. *Nature* **2003**, *421*, 6919.

(26) Feng, X.; Bogan, M. J.; Agnes, G. R. *Anal. Chem.* **2001**, *73*, 4499.

(27) Widmann, J. F.; Aardahl, C. L.; Davis, E. J. *Aerosol Science and Technology* **1997**, *27*, 636.

(28) Richardson, C. B.; Pigg, A. L.; Hightower, R. L. *Proc. Roy. Soc. A* **1989**, *422*, 319.

(29) Roulleau, M.; Desbois, M. *J. Atmos. Sci.* **1972**, *29*, 565.

(30) Schweizer, J. D.; Hanson, D. N. *J. Colloid and Interface Sci.* **1971**, *35*, 417.

(31) Berg, T. G. O.; Trainor, R. J.; Vaughan, U. *J. Atmos. Sci.* **1970**, *27*, 1173.

(32) Ataman, S.; Hanson, D. N. *Ind. Eng. Chem. Fundam.* **1969**, *8*, 833.

(33) Doyle, A.; Moffett, D. R.; Vonnegut, B. *J. Colloid Sci.* **1964**, *19*, 136.

(34) Macky, W. A. *Proc. Roy. Soc. A* **1931**, *133*, 565.

(35) Wilson, C. T. R.; Taylor, G. I. *Proc. Cambridge Philos. Soc.* **1925**, *22*, 728.

(36) Nolan, J. J. *Proc. R. Ir. Acad. Sect. A* **1926**, *37*, 28.

(37) Inculet, I. I.; Kromann, R. *IEEE Trans. Ind. Appl.* **1989**, *25*, 945.

(38) Basaran, O. A.; Scriven, L. E. *Phys. Fluids A* **1989**, *1*, 799.

(39) Saville, D. A. *Annu. Rev. Fluid Mech.* **1997**, *29*, 27.

(40) Abbas, M. A.; Latham, J. *J. Fluid Mech.* **1967**, *30*, 663.

(41) Abbas, M. A.; Latham, J. *Q. J. R. Met. Soc.* **1969**, *95*, 63.

Chapter 3. Studying the time-evolution of charged droplets generated by electrospray ionization in an ion mobility cell. The ping-pong experiment revisited

Portions adapted from Grimm, Ronald L.; Beauchamp, J. L. *Anal. Chem*. **2002**, *74*, 6291.

3.1. Introduction

Rather than use an electrodynamic balance to trap and hold droplets where the electric forces balance the force of gravity ($qE = mg$), the Beauchamp group employs an ion mobility spectrometer (IMS). In our IMS, $qE \neq mg$ and droplets are dragged through a linear electric field while being characterized according to size, equilibrium velocity, and net charge using a phase Doppler anemometer (PDA). This chapter reviews the theoretical and practical aspects of the experimental apparatus employed for the fundamental studies of droplet evaporation and discharge dynamics discussed in Chapters 4 and 5.

In this chapter, section 3.2 discusses the advantages and disadvantages of mobility studies. Section 3.3 reviews the instrumentation for these studies. Sections 3.4 and 3.5 introduce the equations of motion for a charged droplet and apply these equations of motion to a model for droplet behavior in the mobility cell. Section 3.5 presents the results from the model for droplets of varying size and charge as well as a discussion of the implication for mobility studies of evaporation and discharge dynamics.

3.2. The benefits of mobility measurements of charged droplets

Lord Rayleigh developed the critical theories of charged droplets, balancing the forces of surface tension and charge repulsion to determine charged droplet stability. His work suggests that, in a droplet of radius r and surface tension σ in a medium of electric permittivity ε, charge repulsion will overcome surface tension at a charge q_{R} given by equation (3.1). When this condition is met, Rayleigh predicts that droplets undergo a disruptive event in which “the liquid is thrown out in fine jets, whose fineness, however, has a limit”. Although this suggests a mechanism for the discharge event, his model lacks a quantitative description of the charge loss and specific relationships between the parent and the progeny drop or droplets.[1]

$$q_{\mathrm{R}} = 8\pi\varepsilon^{1/2}\sigma^{1/2}r^{3/2} \tag{3.1}$$

Many researchers have studied the dynamics of the evaporation, jetting, and progeny droplet formation associated with this event, termed Rayleigh discharge. As Table 2.1 notes, the majority of evaporation and Rayleigh discharge studies have been performed on low vapor pressure solvent droplets suspended in an electrodynamic balance (EDB). These studies generally conclude that charge loss is proportional to droplet surface tension, and the droplet undergoes discharge between 70 and 120% of its predicted Rayleigh limit. Additionally, the studies show that discharge events generally remove 10-40% of the parent droplet charge and only 1-5% of the parent droplet mass. Unfortunately, not all of the results support this conclusion. Indeed, even experiments performed within the past five years have generated vastly diverging results. Feng et al. note the loss of 80% of the net charge in the Rayleigh discharge events of methanol ($\sigma = 0.022$ N m^{-1}) droplets in an electrodynamic balance,[2] whereas Duft and co-workers observe loss of 25 to 33% the net charge on ethylene glycol (σ = 0.048 N m^{-1}) droplets.[3,4] Such results suggest that different techniques are needed to compliment the existing picture of Rayleigh discharge phenomena.

In our laboratory, Smith and coworkers demonstrate that ion mobility spectrometry is an effective tool for Rayleigh discharge studies of higher vapor pressure solvents that are otherwise difficult to analyze in an EDB.[5,6] In the mobility cell, droplets are subjected to a linear, uniform ~50 V cm^{-1} electric field directed parallel or antiparallel to the force of gravity. Such field strengths produce negligible distortions to the droplet. Additionally, there are no fields providing radial trapping as exist in the electrodynamic balance experiments that might affect the droplet behavior.

3.3. Instrumentation

Figure 3.1 presents a schematic of the experimental apparatus. The instrument consists of three parts: the electrospray source that generates charged droplets in the 10-100 μm size range, the mobility cell (often referred to as a drift cell or the drift region), and a phase Doppler anemometer (PDA) that characterizes droplet size, velocity and charge. Smith presents an excellent review of the hardware, experimental procedures and data analysis,[5] and the instrument has been described several times in the literature.[6,7] This section summarizes the critical aspects of the hardware and provides context for the Rayleigh discharge studies presented in Chapters 4 and 5.

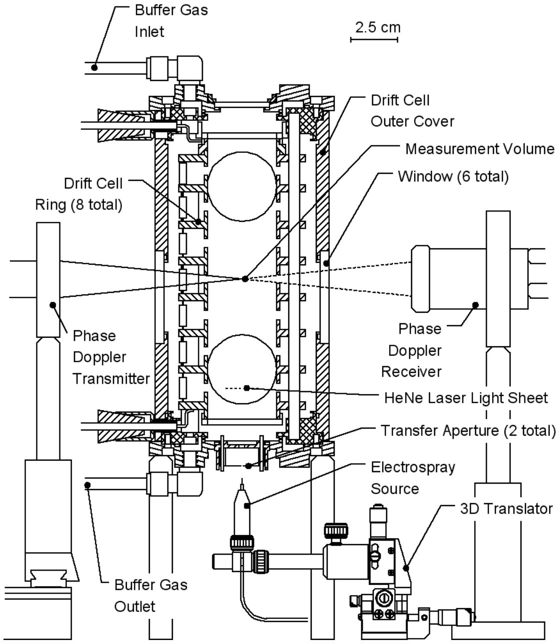

Figure 3.1. Schematic representation of the apparatus employed for droplet evaporation and discharge studies. Droplets are generated by the electrospray source and directed through two apertures into the drift region of the ion mobility cell. Droplet “ping-pong” commences when a droplet passes through the measurement volume of the phase Doppler anemometer. Adapted from Grimm and Beauchamp.[7]

3.3.1. Electrospray ionization source

Droplets are produced at the electrospray ionization source and directed upward through the ion mobility spectrometer (IMS) drift cell for analysis. A polished hypodermic stainless steel needle (R-HTX-35, 64 μm i.d., 150 μm o.d., Small Parts, Inc.) mounted on a three-dimensional stage sprays upward through two sequential apertures on the bottom of the drift cell. The first aperture is 500 μm in diameter and biased at +100 V. One centimeter above the first, the second aperture is 1.5 mm in diameter and maintained at earth ground. To generate positively charged droplets between 10 and 60 μm in diameter, the electrospray needle is biased between +800 and +1200 V, and the distance between the hypodermic needle tip and the first aperture is adjusted between 0.5 and 5 mm. Our experimental arrangement selects droplets close to the axis of the spray. Solvents are used without further purification. In all cases, solution flow rates are 0.2-0.5 μL min^{-1} and dry nitrogen gas flows downward through the cell at 0.3 L min^{-1} or 0.6 cm s^{-1}.

3.3.2. Ion mobility cell and the ping-pong technique

Eight vertically stacked, resistively coupled, stainless steel rings define a 20 cm-long, 4 cm-inner diameter drift region within the IMS. Dry nitrogen gas at ambient temperature (293 K) flows downward through the drift cell to ensure the droplets are evaporating in an environment free from solvent vapor. In the center of the cell, 10 cm above the electrospray source, two intersecting HeNe laser beams form the measurement volume, roughly 150 μm in diameter, of the phase Doppler anemometer (PDA). The phase Doppler anemometer acquires the velocity and diameter of the droplet. These values yield the net droplet charge through a force-balance equation of motion discussed later in this chapter.

A 50.6 V cm^{-1} electric field initially directs positively charged droplets upward through the cell. Droplets initially travel at 50 cm s^{-1} taking ~200 ms to reach the PDA measurement volume discussed in Section 3.3.3. Data used to determine droplet size and velocity are acquired by the PDA and recorded using a digital oscilloscope when a droplet drifts upwards through the measurement volume. The oscilloscope triggers two high-voltage MOSFET switches (MTP1N100E, Motorola) that reverse the cell voltages causing the droplet to travel downward towards the measurement volume. Subsequent PDA detection and field switching repeats at roughly 100 Hz and the droplet undergoes a ping-pong motion through the measurement volume until it is no longer detected, either because of evaporation to an undetectable size (~1 μm) or from radially drifting beyond the measurement volume. The latter is the principle reason for terminating acquisition, as no radial trapping force exists in the cell. Droplet ping-pong and PDA analysis records a history of the diameter, velocity, and charge sampled roughly every 10 ms. Percent Rayleigh limit is determined by the ratio of the charge to q_R, calculated by equation (3.1).

3.3.3. Phase Doppler anemometer

The phase Doppler assembly consists of a transmitter and receiver shown in Figure 3.2. In the transmitter, a Helium-Neon (HeNe) laser generates $\lambda = 632.8$ nm linearly polarized light for the transmitter. The beam passes through a two-lens beam expander followed by a prism that separates the original beam into two parallel beams

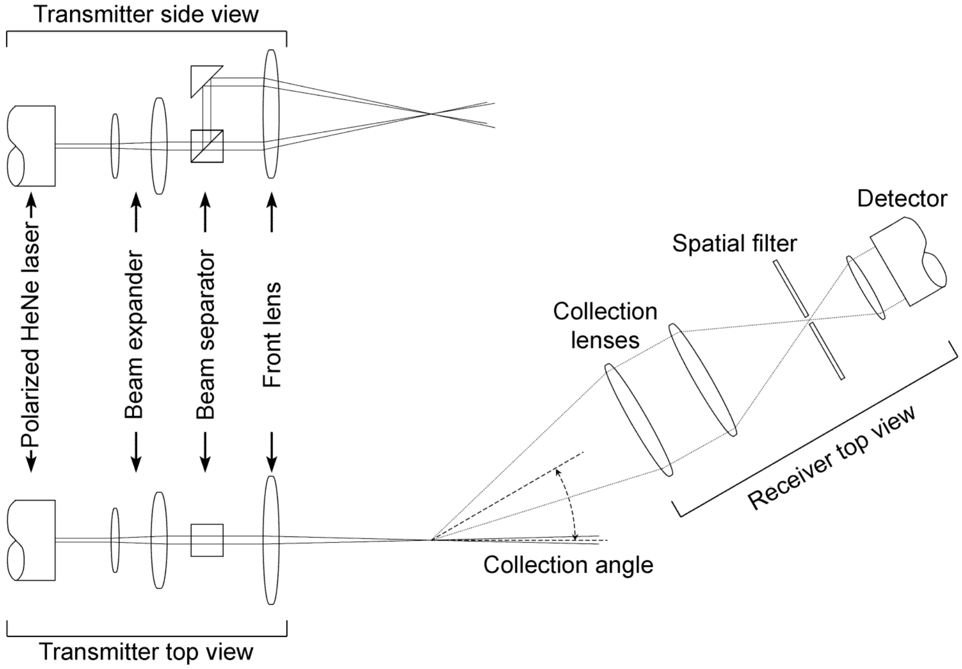

Figure 3.2. Schematic of the phase Doppler anemometer arrangement. In the transmitter array, light generated by a helium neon laser passes through a two-lens beam expander and is split with a beam separator into two parallel beams. The front lens directs the beams together where the interference fringes define the measurement volume. Scattered light is collected by the receiver array where collection lenses direct light through a spatial filter onto a two-element photodiode array.

with a well-defined spacing, s. A focusing lens with focal length F directs the beams to a measurement volume consisting of a series of constructive and destructive interference fringes stacked parallel to the laser propagation plane. When $s << F$, the fringe spacing, δ, is approximated by eq (3.2).

$$\delta \approx \frac{\lambda F}{s} \tag{3.2}$$

The beam waist diameter, D_w, of the laser beams passing through the focusing lens determines the size of the measurement volume, shown in eq (3.3).

$$D_w = \frac{4\lambda F}{\pi D_{beam}} \tag{3.3}$$

In eq (3.3), D_{beam} represents the diameter of the laser beams prior to passing through the focusing lens. In this experiment D_{beam} is twice the diameter of the beam generated by the laser as a result of the 2*x* beam expander. The number of fringes in the measurement volume is approximately D_w / δ. For a typical configuration in which $s = 23$ mm and $F = 250$ mm, the fringe spacing is approximately 6.9 μm and the measurement volume waist diameter is ~200 μm, which provides approximately 29 usable fringes.

Droplets scatter light that is then detected by the PDA receiver assembly. This assembly consists of two collection lenses that direct the scattered light through a spatial filter and onto a detector consisting of two vertically stacked photodiode elements. The receiver assembly is mounted in the scattering plane and 30° off-axis of the laser propagation plane to maximize the Mie-scattered light while minimizing interference from the transmitter itself. As a droplet passes upwards into the measurement volume, the scattered light sweeps upwards past the collection lenses. The signal at the lower photodiode leads the upper photodiode with a phase shift well defined by the curvature of the droplet. The PDA receiver detects velocity information because light scattered from each fringe arrives at the detectors temporally separated. Droplet velocity is computed from this time spacing and the fringe spacing defined in eq (3.2). Droplet size is computed from numerical solutions relating the phase shift of the detector signals to the curvature of the droplet.

3.4. Equations of motion of a droplet in the ion mobility cell

Size and velocity information from the phase Doppler anemometer may be inserted into a force balance equation to determine droplet charge. Deriving equations of motion of a droplet under the influence of multiple forces begins with a generalized force balance eq (3.4) where m_p is the particle mass, v is the velocity, t is time, and F_i is the contribution of the ith force.

$$m_\mathrm{p} \frac{d}{dt} v = \sum_i F_i \tag{3.4}$$

In the case of a droplet with charge $q \neq 0$ under the influence of an electric field, gravity, and atmospheric drag, the force balance equation is represented by eq (3.5).

$$m_\mathrm{p} \frac{d}{dt} v = F_{field} + F_{gravity} - F_{drag} \tag{3.5}$$

For consistency, motion upwards (against gravity) is defined as a positive velocity and motion downwards (with gravity) is defined as negative. When the electric field, E, is aligned antiparallel to gravity, $F_{field} = +qE$ resulting in upwards motion and $-qE$ when parallel to gravity resulting in downwards motion. The force of gravity is always downwards, thus $F_{gravity} = -m_\mathrm{p}g$. Here g is the accelleration due to gravity, E is the electric field strength, and q is the net charge. Since atmospheric drag dampens droplet motion F_{drag} always opposes the direction of velocity. Therefore, the sign of F_{drag} always opposes the sign of v. For the case of spherical droplets between 1 and 100 µm in diameter, the force of drag due to the atmosphere is given by equation (8.31) in Seinfield and Pandis[8] divided by the Cunningham slip correction factor, C_c, shown in eq

$$F_{drag} = \frac{\pi C_\mathrm{D} \rho_{air} d_\mathrm{p}^2 v^2}{8 C_\mathrm{c}} \tag{3.6}$$

In (3.6), where C_D is the drag coefficient, ρ_{air} is the density of air, and d_p is the droplet diameter. Combining the terms, eq (3.7) expresses eq (3.5) with the appropriate force equations for droplets being directed upwards through the drift cell.

$$m_\mathrm{p} \frac{d}{dt} v = qE - m_\mathrm{p} g - \frac{\pi C_\mathrm{D} \rho_{air} d_\mathrm{p}^2 v^2}{8 C_\mathrm{c}} \tag{3.7}$$

When the forces acting on the droplet are in equilibrium and there is no net acceleration, $dv / dt = 0$ and eq (3.7) simplifies to give the velocity of a droplet as a function of size and charge in eq (3.8) or the charge on the droplet as a function of size and velocity in eq (3.9).

$$v = \left[\frac{8 C_\mathrm{c}}{\pi C_\mathrm{D} \rho_{air} d_\mathrm{p}^2} \left(qE - m_\mathrm{p} g \right) \right]^{1/2} \tag{3.8}$$

$$q = \frac{\pi C_\mathrm{D} \rho_{air} d_\mathrm{p}^2 v^2 + 8 C_\mathrm{c} m_\mathrm{p} g}{8 C_\mathrm{c} E} \tag{3.9}$$

Equations (3.8) and (3.9) apply to upwards drift in the cell. Equation (3.10) represents the charge when the electric field is reversed and droplets are directed downwards through the cell.

$$q = \frac{\pi C_\mathrm{D} \rho_{air} d_\mathrm{p}^2 v^2 - 8 C_\mathrm{c} m_\mathrm{p} g}{8 C_\mathrm{c} E} \tag{3.10}$$

3.5. Modeling droplet behavior to determine droplet relaxation time

The assertion of equilibrium is critical to determining droplet charge from the phase Doppler data. For droplets under the influence of drag and gravity, Seinfeld and Pandis calculate the characteristic relaxation time, τ, given by equation (8.38) in their text and equation (3.11) below.[8] Tau represents the time to reach $1 - e^{-1}$ or 63% of the equilibrium velocity as a function of size and drag factors.

$$\tau = \frac{m_{\mathrm{p}} C_{\mathrm{c}}}{3\pi \mu_{air} d_{\mathrm{p}}} \tag{3.11}$$

Figure 3.3 shows a plot of eq (3.11) for water and methanol droplets in the size range studied in the ping-pong experiment. The millisecond order of magnitude is close to the 10 ms sampling time indicating that the droplets might not have reached their equilibrium velocity before being sampled. Additionally, eq (3.11) represents the characteristic relaxation time of a droplet only under the force of gravity and atmospheric drag; the effect of an electric field is not considered. Modeling droplet behavior using equation (3.5) is necessary for a complete understanding of droplet behavior within the cell.

3.5.1. Modeling the droplet motion using Euler's Method

Because the previously discussed relaxation time does not consider the effect of an applied electric field, numerical methods can determine whether droplets passing through the measurement volume have reached their terminal velocity. To apply eq (3.5), Euler's method determines the velocity, *v*, and position, *z*, after *i* timesteps as a function

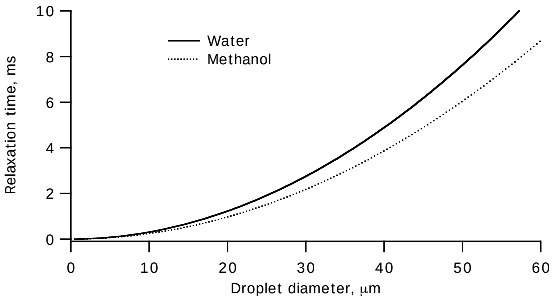

Figure 3.3. Characteristic relaxation time for a droplet under the influence of gravity and atmospheric drag. Both methanol and water droplets in the micron size regime reach their terminal velocity in milliseconds.

of time according to equations (3.12) and (3.13) respectively. The model is applied in Microsoft Excel and Igor Pro (WaveMetrics, Lake Oswego, Oregon).

$$v_{i+1} = v_i + \Delta t \frac{d}{dt} v_i \tag{3.12}$$

$$z_{i+1} = z_i + \Delta t v_i \tag{3.13}$$

In this model dv_i / dt is determined by (3.5). Initially the droplet starts out at the measurement volume defined as $z = 0$ with some initial positive, upward velocity v_0.

Rules for changing the sign of F_{drag} and F_{field} determine the ping-pong behavior of the droplet. The sign of F_{drag} is always opposite of the sign of v since the drag force always opposes droplet motion. Each time the droplet passes through $z = 0$, the electric field reverses. However, because of delays inherent in the electronics, there is always a lag between the droplet passing through the measurement volume and the field reversal. Thus the model field does not switch until a delay time t_{d} after a $z = 0$ event occurs corresponding to the droplet passing through the measurement volume.

This model determines droplet position and velocity for 50 ms using 25 μs timesteps. No significant difference is observed when using a fourth-order Runge-Kutta numerical method to calculate velocity and position rather than Euler's method.[9] This is attributed to the small, 25 μs timestep employed in the method.

3.5.2. Model results as a function of droplet size

Figure 3.4 presents the model results for 50 μm (frame A), 30 μm (frame B) and 10 μm (frame C) diameter water droplets at their Rayleigh limit of charge. In all cases

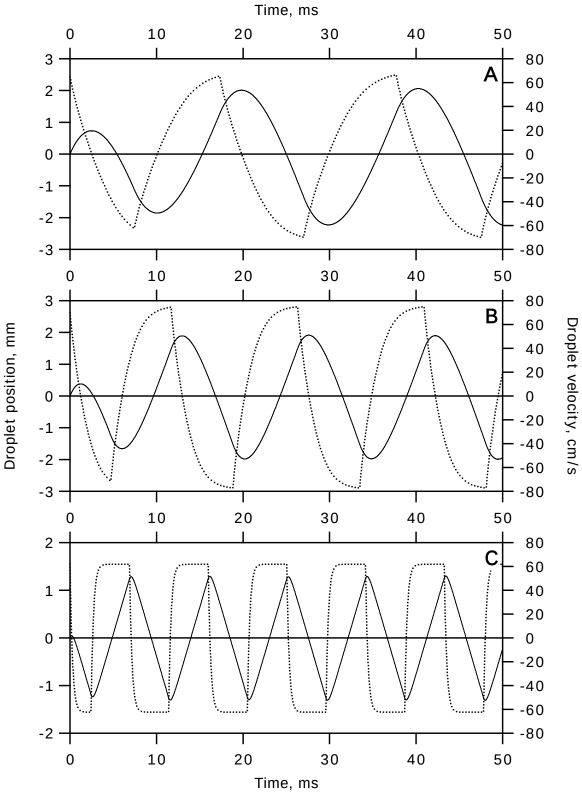

Figure 3.4. Position (solid) relative to the measurement volume and velocity (dotted) versus time for (A) 50 μm, (B) 30 μm, and (C) 10 μm diameter water droplets at their Rayleigh limit in our mobility cell. Because the velocity does not level off at each step, the 50 μm droplets are most likely not at equilibrium when characterized by the PDA. The 10 μm droplets are at equilibrium and the 30 μm droplets are close to equilibrium.

the applied electric field is 50 V cm^{-1} and t_d = 2 ms. The velocity plots (dotted curve) show that 50 μm droplets do not reach their equilibrium velocity before the field is reversed. The relaxation time for 50 μm droplets is estimated to be greater than 10 ms. The 30 μm droplets are closer to reaching their equilibrium velocity, but these too are not at equilibrium when they pass through the measurement volume. The relaxation time for 30 μm droplets is less than 10 ms. Conversely, the 10 μm droplets reach their equilibrium velocity within 2 ms of a field reversal. The results demonstrate that smaller droplets reach equilibrium much more rapidly than larger droplets. This is in agreement with Seinfeld and Pandis for droplets under the influence only of gravity.[8] Because the 50 μm droplets are not yet in equilibrium, eqs (3.9) and (3.10) would introduce significant error in the calculated charge since q is proportional to v^2. Conversely, 10 μm droplets do reach equilibrium and therefore are well modeled by eqs (3.9) and (3.10).

3.5.3. Model results as a function of droplet charge

Figure 3.5 presents the behavior of 50 μm water droplets at 100% (frame A), 50% (frame B), and 10% (frame C) of their Rayleigh limit of charge. The Rayleigh limit for a 50 μm water droplet is 1.57×10^7 elementary charges. In all cases, droplets do not reach their equilibrium velocities indicating that droplet charge is not as important a parameter as diameter. In all cases the droplet's motion is centered below $z = 0$ because the droplets travel downwards faster than they travel upwards as a result of $F_{gravity}$. However, the effect is not as pronounced until low charge values as seen in Figure 3.5C with 10% of the Rayleigh limit of charge. In this case qE is only twice as large as $m_p g$, whereas qE is twenty times larger than $m_p g$ for 50 μm water droplets at the Rayleigh limit (frame A).

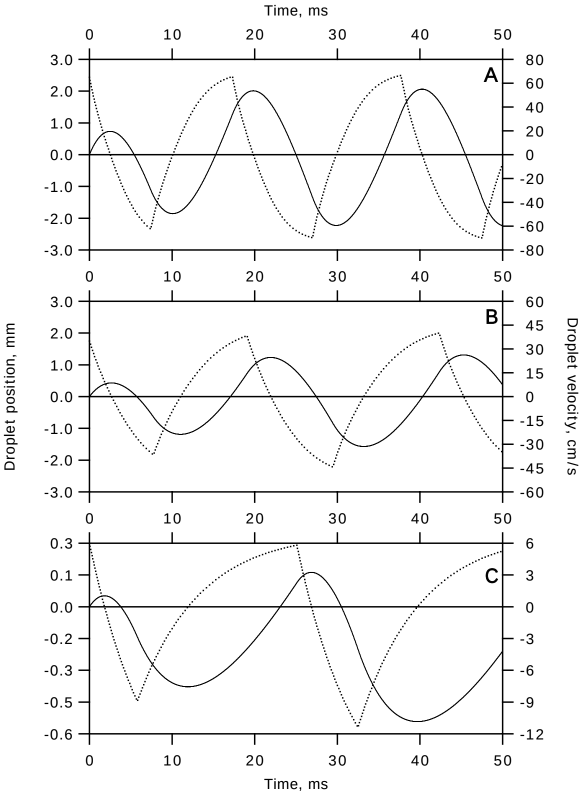

Figure 3.5. Position (solid) relative to the measurement volume and velocity (dotted) versus time for 50 μm diameter water droplets at (A) 100%, (B) 50%, and (C) 10% of their Rayleigh limit of charge. None of these droplets reach equilibrium before reaching the PDA.

3.6. Evaporation of micron-sized droplets within the IMS

For micron-size particles, droplets are significantly larger than the mean free path in air, 0.065 μm. In this continuum regime, evaporation is dominated by the rate at which vapor diffuses away from the droplet surface.[10] Following the notation and derivation similar to Hinds, eq (3.14) determines the evaporation rate for single-component droplets.[10]

$$\frac{d}{dt}d_{\mathrm{p}} = \frac{-4D_{ij}\left(T_{\mathrm{p}}\right)M}{R\rho_{\mathrm{p}}d_{\mathrm{p}}}\frac{p_{\mathrm{p}}\left(T_{\mathrm{p}}\right)}{T_{\mathrm{p}}} \tag{3.14}$$

In eq (3.14), solvent-specific parameters include $D_{ij}(T_{\mathrm{p}})$, the temperature-dependent diffusivity of solvent vapor i in gas j, solvent molar mass M, droplet density ρ_{p}, and equilibrium vapor pressure, $p_{\mathrm{p}}(T_{\mathrm{p}})$, at equilibrium surface temperature T_{p}, while R is the gas constant. This is simplified from a more rigorous model in which solvent vapor in the ambient gas inhibits evaporation. Experimentally, a constant flow of dry nitrogen gas through the apparatus flushes solvent vapor allowing for this simplification. Integrating the evaporation rate yields eq (3.15).

$$d_{\mathrm{p}}^2 = d_{\mathrm{o}}^2 + st \tag{3.15}$$

Equation (3.15) clusters the solvent-specific parameters into a single variable, s, given by eq (3.16).

$$s = -\frac{8D_{ij}(T_{\mathrm{p}})M}{R\rho_{\mathrm{p}}}\frac{p_{\mathrm{p}}(T_{\mathrm{p}})}{T_{\mathrm{p}}} \tag{3.16}$$

Spontaneous evaporation is endothermic, lowering the surface temperature to a size-independent equilibrium value, T_{p}, given by eq (3.17).

$$T_{\mathrm{p}} = T_{\infty} - \frac{D_{ij}(T_{\mathrm{p}})\Delta H_{\mathrm{vap}}(T_{\mathrm{p}})}{Rk_{\mathrm{v}}(T_{\mathrm{p}})} \frac{p_{\mathrm{p}}(T_{\mathrm{p}})}{T_{\mathrm{p}}} \tag{3.17}$$

The surface temperature, T_{p}, is determined by the ambient gas temperature, T_{∞}, and thermodynamic values $\Delta H_{\mathrm{vap}}(T_{\mathrm{p}})$ and k_{v}, the heat of vaporization and the thermal conductivity of the medium, respectively. Equation (3.17) must be iteratively solved for the equilibrium temperature because several parameters are temperature dependent. Heat of vaporization and vapor pressure data from Yaws[11] and diffusivity data from Vargaftik et al.[12] are inserted into eqs (3.15) through (3.17) for the evaporation of the three hydrocarbon solvents described in Chapter 4, as well as for methanol, acetonitrile, and water for comparison with previous studies.[6] The diffusivity for *p*-xylene was approximated by using the value for toluene. Table 3.1 lists the calculated solvent parameters, *s*, for the evaporation of acetonitrile, methanol, water, heptane, octane and *p*-xylene. As suggested by equations (3.15)-(3.17) and Table 3.1, *s* is a useful variable for quickly quantifying the evaporation rate of a particular solvent. Rapidly evaporating solvents have particularly large values of *s* while more slowly evaporating solvents have smaller values.

When ascertaining the timescales of the processes involved in the ping-pong experiment, it is also often useful to know the lifetime of a droplet. This is approximated by equation (3.15) when d_{p} is set to zero. Therefore, the lifetime of a particle is approximately $-d_{\mathrm{o}}^2/s$. Using the values of *s* in Table 3.1, the lifetime of a 50 μm droplet ranges from 210 ms for *n*-heptane to up to 2 seconds for water.

	dielectric constant, ε	surface tension, γ (mN s^{-1})	evaporation temperature, T_p (K)	theoretical slope, s (μm^2 s^{-1})
Acetonitrile	36.64	28.66	270	-6500
Methanol	33.0	22.07	267	-4750
Water	74.6	71.99	278	-1250
n-Heptane	1.921	19.65	278	-11900
n-Octane	1.944	21.14	287	-3670
p-Xylene	2.274	28.01	289	-2200

Table 3.1. Physical parameters for solvents characterized by the "ping-pong" technique. Physical constants at 293K are taken from Lide.[13] Theoretical evaporation parameters are calculated from equations (3.15)-(3.17).

3.7. Conclusions

The ping pong experiment presents a unique way of determining the evaporation and Rayleigh discharge dynamics of micron-sized droplets. Mobility measurements are performed in a mild, uniform, linear, switched DC electric field as opposed to the alternating AC fields employed in an electrodynamic balance experiments. In the ping-pong experiment, the field is repeatedly reversed following characterization of diameter, size, and charge by a phase Doppler anemometer. Repeated PDA characterizations create a history of the droplet in which Rayleigh discharge events are observed.

Modeling droplet behavior shows that larger 50 μm droplets are not well characterized by our ping-pong experiment because they do not reach equilibrium before they are analyzed by the PDA and therefore are not subject to the force-balance equation employed to determine charge. Smaller droplets do reach their equilibrium velocity and are accurately characterized by the PDA and the force-balance equations.

3.8. References

(1) Rayleigh, L. *Philos. Mag.* **1882**, *14*, 184.

(2) Feng, X.; Bogan, M. J.; Agnes, G. R. *Anal. Chem.* **2001**, *73*, 4499.

(3) Duft, D.; Lebius, H.; Huber, B. A.; Guet, C.; Leisner, T. *Phys. Rev. Lett.* **2002**, *89*, art. no. 084503.

(4) Duft, D.; Atchtzehn, T.; Muller, R.; Huber, B. A.; Leisner, T. *Nature* **2003**, *421*, 6919.

(5) Smith, J. N. Fundamental Studies of Droplet Evaporation and Discharge Dynamics in Electrospray Ionization, California Institute of Technology, 2000.

(6) Smith, J. N.; Flagan, R. C.; Beauchamp, J. L. *J. Phys. Chem. A* **2002**, *106*, 9957.

(7) Grimm, R. L.; Beauchamp, J. L. *Anal. Chem.* **2002**, *74*, 6291.

(8) Seinfeld, J. H.; Pandis, S. N. *Atmospheric chemistry and physics*; Wiley-Interscience: New York, 1998.

(9) Gerald, C. F.; Wheatley, P. O. *Applied numerical analysis*, 5th ed.; Addison-Wesley: Reading, MA, 1994.

(10) Hinds, W. C. *Aerosol Technology: Properties, Behaivor, and Measurement of Airborne Particles*, 2nd ed.; John Wiley & Sons, Inc.: New York, 1999.

(11) Yaws, C. L. *Chemical Properties Handbook: Physical, Thermodynamic, Environmental, Transport, Safety, And Health Related Properties for Organic and Inorganic Chemicals*; McGraw-Hill: New York, 1999.

(12) Vargaftik, N. B.; Vinogradov, Y. K.; Yargin, V. S. *Handbook of Physical Properties of Liquids and Gases: Pure Substances and Mixtures,* 3rd ed.; Begell House, Inc., 1996.

(13) *CRC Handbook of Chemistry and Physics*; 76th ed.; Lide, D. R., Ed.; CRC Press: Boca Raton, FL, 1995.

Chapter 4. Evaporation and discharge dynamics of highly charged droplets of heptane, octane, and *p*-xylene generated by electrospray ionization

Adapted from Grimm, Ronald L. and Beauchamp, J. L. *Anal. Chem.* **2002**, *74*, 6291.

4.1. Abstract

We report studies of the evaporation and discharge dynamics of highly charged droplets generated by electrospray ionization from *n*-heptane, *n*-octane, and *p*-xylene doped with Stadis-450, a conductivity enhancing agent. A phase Doppler anemometer (PDA) characterizes individual droplets moving through the uniform electric field within an ion mobility cell according to size, velocity, and charge. Repeated reversal of the electric field allows multiple PDA measurements on selected droplets with diameters ranging from 3 to 60 μm and up to 10^7 elementary positive charges. This "ping-pong" technique provides individual droplet histories from which we determine the dynamics of solvent evaporation and charge loss. On average, *n*-heptane discharges at 101% of the Rayleigh limit of charge, while *n*-octane and *p*-xylene droplets discharge at 87% and 89% of their respective limits. Discharge events release an average of 19% of the charge in *n*-heptane, and 17% of the charge in both *n*-octane and *p*-xylene. Within the limits of the measurements, no detectable change in droplet diameter accompanies observed discharge events, indicating the loss of a relatively small fraction of the total volume. We compare these results to previous experiments, theoretical models for droplet evaporation and discharge, and predictions from the Rayleigh model. We report both Stadis-450 and

triethylamine mass spectra in octane, and discuss issues regarding the use of hydrocarbon solvents in electrospray mass spectrometry.

4.2. Introduction

Polar liquids are the primary solvents for electrospray ionization and their discharge dynamics have been well studied.[1] Lord Rayleigh developed the critical theories of charged droplets, balancing the forces of surface tension and charge repulsing to determine charged droplet stability. His work suggests that, in a droplet of radius r and surface tension σ in a medium of electric permittivity ε, charge repulsion will overcome surface tension at a charge q_R given by eq (4.1). When this condition is met, Rayleigh predicts that droplets undergo a disruptive event in which “the liquid is thrown out in fine jets, whose fineness, however, has a limit”. Although this suggests a mechanism for the discharge event, his model lacks a quantitative description of the charge loss of specific relationships between progeny drop or droplets and the parent.[1]

$$q_{\mathrm{R}} = 8\pi\varepsilon^{1/2}\sigma^{1/2}r^{3/2} \tag{4.1}$$

Recent studies in our laboratory focused on the more common electrospray solvents water, methanol, and acetonitrile. This work suggests a solvent dependence on the charge loss and the percent Rayleigh limit at discharge.[1,2] These results are summarized in Table 4.1.

On the other hand, high-volatility hydrocarbons and similar low-conductivity solvents are not widely employed for electrospray mass spectrometry and their Rayleigh discharge characteristics have received less attention than more commonly used polar solvents such as water and methanol. Several researchers present spectra of crude oils and hydrocarbon fuels dissolved in solutions of polar solvents.[3-5] Rebek and coworkers report the use of benzene and xylene without the addition of polar solvents,[6,7] but few others routinely employ hydrocarbons as solvents for analytical applications of electrospray mass spectrometry. Tang and Gomez generated a stable electrospray of n-heptane, focusing on the dynamics of the spray itself,[8] as well as size determinations and percent Rayleigh limit approximations for droplets within the spray.[9] Most recently Leisner and coworkers have developed experimental methodologies for studying the evaporation and discharge dynamics of low-volatility solvents. They have acquired images of a discharge event from glycerol characterized by simultaneous, symmetrical emission of two fine streams of progeny droplets from opposite sides of the droplet.[10] This contrasts with the previous work of both Gomez and Tang,[9] as well as Kebarle and coworkers[11] who present visual evidence of droplet distortions leading to discharge from a single point on a parent droplet near the Rayleigh limit for heptane and methanol, respectively.

We report the evaporation and discharge dynamics of three volatile hydrocarbon solvents, and relate the dynamics to previously researched solvents widely employed in electrospray mass spectrometry. The present work investigates positively charged 3-60 μm droplets of *n*-heptane, *n*-octane, and *p*-xylene with up to 10^7 elementary charges. To reduce droplet sizes to a range accessible for measurement using our experimental methodology, Stadis-450, a conductivity enhancing agent, is added to each of these solvents. Previous studies demonstrated that Stadis-450 does not significantly affect the surface tension and the dielectric constant of bulk heptane in concentrations up to 3%.[8]

Discharges are characterized by measuring the droplet diameter and charge, as well as the charge loss at the time of the event. We are not able to detect mass loss associated with a discharge event. Overall mass loss due to evaporation is measured and compared against models discussed in chapter three. Table 4.1 lists the calculated solvent parameters, *s*, for the evaporation of acetonitrile, methanol, water, heptane, octane and *p*-xylene. We additionally present data illustrating the use of these hydrocarbon solvents in conventional electrospray mass spectrometry analyses. Spectra are reported for both Stadis-450 and triethylamine in octane.

4.3. Experimental section

The details of the experimental apparatus are described in chapter three. Only deviations and specific implementations are presented.

4.3.1. Experimental conditions

Solvents *n*-heptane (99.5%, Mallinckrodt), *n*-octane (97% GC grade, Alfa-Aesar) and *p*-xylene (99+% HPLC grade, Aldrich) were used without further purification. The conductivity enhancer, Stadis-450 (Octel America), was added in 1% by volume to n-heptane and n-octane and 0.1% to *p*-xylene. The electrospray needle was held 2 mm away from the first aperture of the IMS and maintained at 875 V for n-heptane and n-octane, and maintained at 1060 V for p-xylene. In each case, solution flow rates were 0.2-0.5 μL min^{-1} and dry nitrogen gas flowed downward through the cell at 0.3 L min^{-1} or 0.6 cm s^{-1}.

	dielectric constant, ε	surface tension, γ (mN s^{-1})	percent charge loss	percent Rayleigh limit	evaporation temperature, T_d (K)	theor. slope, s ($\mu m^2\ s^{-1}$)	experim. slope, s ($\mu m^2\ s^{-1}$)
acetonitrile	36.64	28.66	15-20	100	270	-6500	n/a
methanol	33.0	22.07	15-20	120	267	-4750	n/a
water	74.6	71.99	20-40	100	278	-1250	n/a
n-heptane	1.921	19.65	19 (6)	101 (4)	278	-11900	-11000
n-octane	1.944	21.14	17 (10)	87 (8)	287	-3670	-4900
p-xylene	2.274	28.01	17 (6)	89 (3)	289	-2200	-2400

Table 4.1. Physical parameters and experimental charge loss values for solvents characterized by the “ping-pong” technique. Values in parenthesis are standard deviations. Acetonitrile, methanol and water data are taken from Smith and coworkers.[1] Physical constants at 293K are taken from Lide.[12] Theoretical evaporation parameters are calculated from equations in Chapter 3.

4.3.2. Electrospray ionization mass spectrometry

A Finnigan LCQ ion trap quadrupole mass spectrometer acquired the mass spectra. A custom built source using a fused-silica nanospray needle (New Objective, 15 μm I.D. tip) replaced the standard electrospray ion source. During acquisition, the capillary was not heated and the sheath gas was removed. The signal was optimized using the built-in tuning capabilities of the LCQ. Triethylamine (99.5%, Aldrich) was used without further purification.

4.4. Results

Representative data for a single droplet of *p*-xylene are shown in Figure 4.1. Large, simultaneous decreases in velocity and charge signal the occurrence of discharge events, as indicated by arrows. Specifically, plot (a) shows constant evaporation and a steadily decreasing diameter. Initially, constant charge and decreasing mass leads to an increase in the velocity (b) as the electric force, qE, steadily becomes stronger relative to the force of gravity, $m_p g$. The small oscillations in velocity correspond to motion with and against gravity. As a result of constant charge (c) and steadily decreasing mass, the droplet approaches its Rayleigh limit (d). This trend continues for the first 0.14 s of the droplet data acquisition at which point the velocity, charge, and percent Rayleigh limit ($100q\, q_R^{-1}$) decrease dramatically. The sudden decrease in droplet charge results in a similarly large decrease in velocity, as the change in qE is significantly larger than the change in $m_p g$. We interpret this rapid loss of charge to be a Rayleigh discharge event.

Table 4.1 summarizes the discharge and evaporation characteristics of the three solvents studied along with the corresponding data for acetonitrile, water and methanol previously reported from our laboratory.[1] Between discharge events, individual charge values are averaged, which is illustrated by the dotted lines in Figure 4.1(c). Percent charge loss is determined from the difference between the average charge levels before and after a discharge event. The percent Rayleigh limit at discharge is simply the last recorded value before the sharp decrease characteristic of a discharge event. Both the percent charge lost and the percent Rayleigh limit data are explored with histograms for each solvent in Figure 4.2(a) and (b), respectively. As the distribution of each is roughly Gaussian in shape, Table 4.1 lists standard deviations for these data in parentheses. A linear regression of diameter squared versus time generates the parameters that quantify evaporation. Figure 4.3 shows an example of the fitting performed on the diameter measurements from Figure 4.1(a). The resulting slope values are averaged in Table 4.1 for each solvent. Note that this treatment ignores diameter decreases that result from discharge events.

Both *n*-octane and *p*-xylene were often characterized through 30-50 reversals of the electric field. Up to seven discharge events were observed for n-octane, while p-xylene demonstrated up to eight. For example, the acquisition shown in Figure 4.1 contains five well-defined discharge events highlighted by arrows. Heptane rarely exhibited multiple discharges because its higher evaporation rate results in a shorter residence time in the IMS. Size-charge correlations for droplets from these solvents are shown together in Figure 4.4. The data represent the diameter versus charge for each droplet immediately preceding its first recorded discharge event.

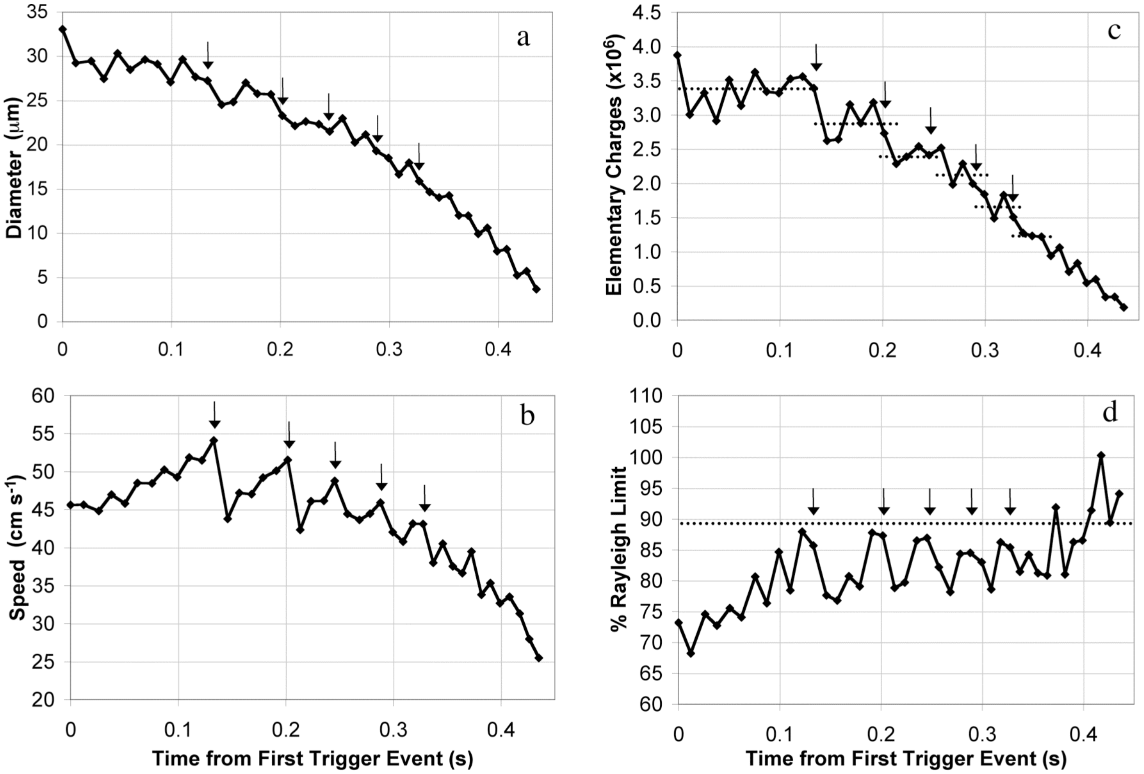

Figure 4.1. Acquired history of a droplet of *p*-xylene including (a) size, (b) velocity, (c) charge, (d) percent Rayleigh limit. As the droplet evaporates its speed increases and charge stays constant until it discharges. Discharge events (indicated by arrows) occur at approximately 90% the Rayleigh limit and are characterized by charge loss of approximately 20% and undetectable mass loss.

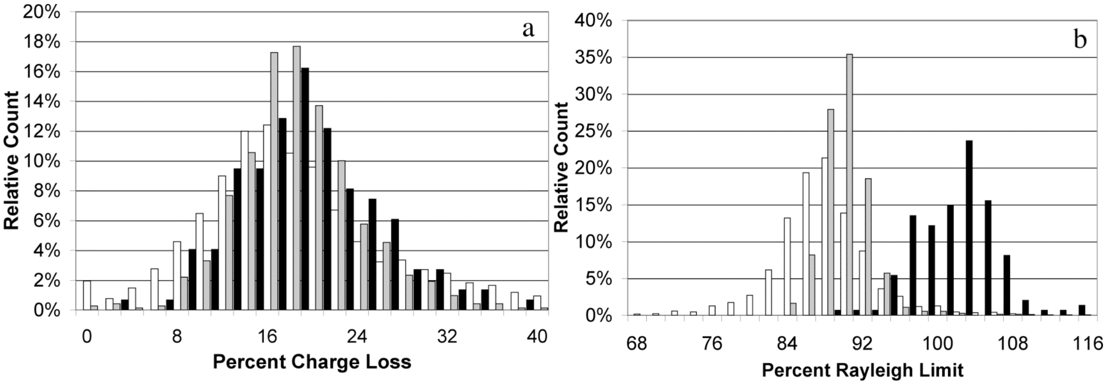

Figure 4.2. Histograms of (a) percent charge lost and (b) percent Rayleigh limit at the point of discharge for each observed discharge event. Due to unequal sample sizes, each histogram is reported as a fraction of the total for each respective solvent. In both histograms, black bars represent n-heptane, white bars represent *n*-octane, and gray bars represent *p*-xylene.

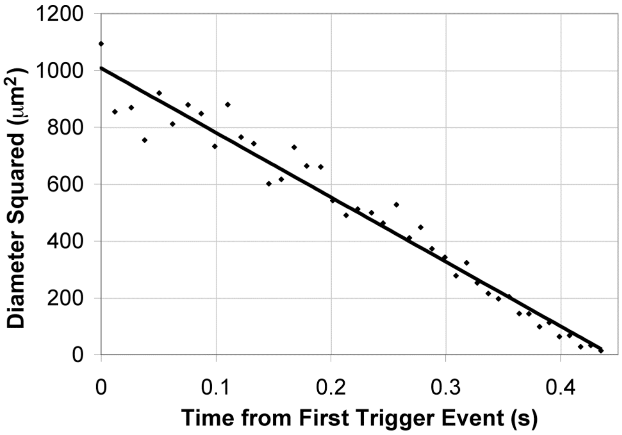

Figure 4.3. Diameter squared versus time for the acquisition shown in Figure 4.1. A linear regression analysis yields a slope $s = -2271\ \mu m^2\ s^{-1}$ that characterizes solvent evaporation. Average experimental values for the slopes of all three solvents are presented in Table 4.1.

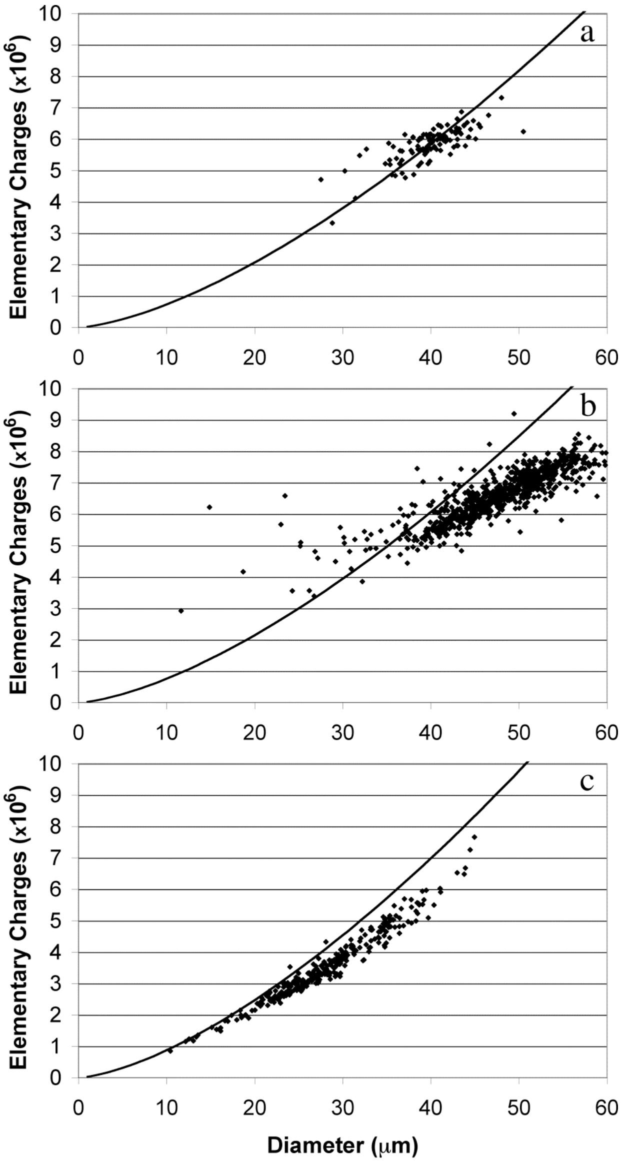

Figure 4.4. Size-charge correlation diagrams for (a) *n*-heptane, (b) *n*-octane, and (c) *p*-xylene for all droplets immediately preceding the first recorded discharge event. Solid lines show the Rayleigh limit for each solvent. The droplet size-charge correlations for heptane and octane are tightly clustered, indicating monodisperse droplet formation for these solvents. In contrast, *p*-xylene droplets are observed over a wide range of size and charge.

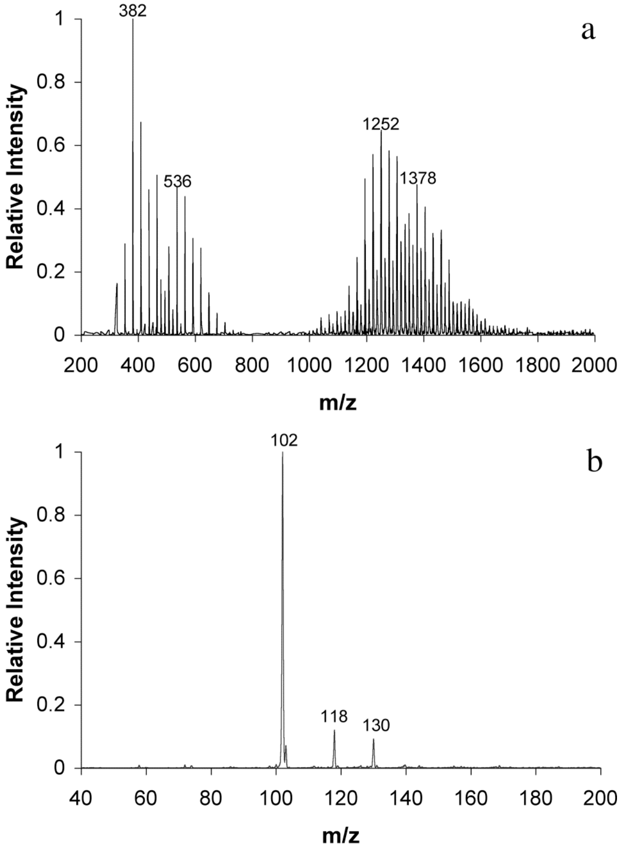

Figure 4.5. Mass spectra of (a) Stadis-450 and (b) triethylamine in octane. Stadis-450 is characterized by two pairs of overlapping distributions centered on 382, 536, 1252, and 1378 m/z. Peaks are separated by 28 m/z units within each distribution are indicative of a hydrocarbon polymer. The protonated triethylamine spectrum (b) shows contaminants at 118 and 130 m/z.

Figure 4.5 shows two mass spectra using n-octane as the electrospray solvent. Spectrum (a) is the averaged mass spectrum showing that a complex array of ions is present when Stadis-450 is added to *n*-octane. Spectrum (b) exhibits the ions observed when triethylamine is added to neat *n*-octane.

4.5. Discussion

4.5.1. Size-charge distributions

Plots in Figure 4.4 show typical diameters of 35-45 μm for heptane (a), 35-60 μm for octane (b), and 10-40 μm for *p*-xylene (c). The droplets in the present study are larger than those produced by common nanospray techniques, but are comparable to the sizes employed in other studies of Rayleigh discharge.[9,13,14] In plotting points immediately preceding the first recorded discharge event for each droplet, Figure 4.4 explores the point at which droplets discharge relative to the Rayleigh limit. Size-charge distributions for latter discharge events resemble those shown in Figure 4.4 and show no additional patterns of interest. Size versus charge does not scale with the Rayleigh limit curves for either heptane or octane as shown on plots (a) and (b), respectively. In both cases, smaller droplets discharge at a higher percent Rayleigh limit than the larger droplets studied. In contrast, *p*-xylene discharges scale with the Rayleigh limit over the size range studied. The distributions in Figure 4.4 support the broader standard deviation in the percent Rayleigh limit at the point of discharge for n-octane and the smaller deviation for *n*-heptane and *p*-xylene listed in Table 4.1 and shown by the histograms in Figure 4.2.

4.5.2. Evaporation and discharge dynamics

The average charge loss in a discharge event for all three solvents is 18 ± 1%. This corresponds favorably with studies by Taflin and coworkers, who reported highly accurate measurements on twelve discharge events of low-volatility oils.[13] Our data for over two thousand discharge events indicate that similar charge loss is observed for high-volatility hydrocarbon solvents as well.

Droplet diameter decreases in time due to solvent evaporation, as is evident in Figure 4.1. Within the accuracy of the measurements, no observable discrete decrease in diameter accompanies the discharge events indicated by arrows. The 4% experimental error in our diameter measurement is significantly larger than that of Taflin and coworkers who report droplet radii between 10-20 μm to within 1 nm.[13] Their observed 2% mass loss would correspond to a 0.7% change in diameter which is significantly below the resolution of our PDA. Therefore we are only able to put an upper bound on the change in diameter at 4%, corresponding to the experimental error in our measurements.

4.5.3. Successive discharges

Earlier “ping-pong” studies in our lab revealed up to five discharge events from a single parent droplet in experiments with methanol.[1] The electric field generated in the IMS is radially uniform and time-independent transverse to droplet motion along the axis of the instrument. This method contrasts with electrodynamic balance experiments, which suspend individual droplets with time-dependent axial and radial fields.[15] To observe multiple discharge events from the same droplet in the IMS, the droplet must not drift radially beyond the 150 μm diameter of the PDA measurement volume. Radial momentum is either a result of a droplet's original path, or from another force imparted on it during its residence time in the IMS. The observation of multiple discharges implies that the net position of the droplet is not significantly affected by a discharge event. On this assumption, Smith discusses the implications for the maximum impulse imparted to the parent droplet.[2] However, recent observations from Leisner and coworkers of simultaneous emission of two progeny droplet streams in opposite directions would be expected to impart little, if any, momentum to the parent droplet.[10]

The decreasing time between successive discharges is consistent with the theoretical treatment by Tang and Smith in which the time between discharges is a function of droplet diameter.[16] Indeed, since q_R is proportional to $r^{3/2}$ according to the Rayleigh limit equation $q_R = 8\pi\varepsilon^{1/2}\sigma^{1/2}r^{3/2}$ and r^2 decreases linearly in time from evaporation, it comes as no surprise that the time between events is decreasing. Beyond the five discharges in Figure 4.1, events occur faster than the 100 Hz data acquisition rate of the experiment. This leads to the observed steady decrease in velocity, as well as the unreliable charge and percent Rayleigh limit information evident in the later period of the acquisition. Further analysis of the multiple discharges in *n*-octane and *p*-xylene reveal that within experimental error, there is no change in the percent charge lost in successive discharge events.

4.5.4. Comparison of discharge characteristics with polar solvents

The data in Table 4.1 for the six solvents studied with the "ping-pong" experiment suggest a correlation between the percent charge lost and both the dielectric constant, ε, and the surface tension, γ, of the solvent. This compares favorably with Fernandez de la Mora's predictions for charge and solvent flow through a discharge event.[17] We assume the electrical conductivity of 4.1×10^{-8} S cm^{-1} measured by Tang and Gomez for 1.2% Stadis-450 in *n*-heptane represents a maximum conductivity for the solutions in the present study. Consequently, there is no correspondence between the discharge characteristics and solution conductivity, which would be significantly higher for the methanol solutions. Previous work in our lab found no significant change in the percent charge lost in a discharge event in methanol solutions with varying concentrations of sodium chloride.[1] This suggests percent charge loss is also dependent on factors not yet explored.

4.5.5. Application to electrospray mass spectrometry

While enhancing the conductivity, Stadis-450 is not a desirable additive for electrospray ionization using hydrocarbon solvents. Figure 4.5(a) shows the mass spectrum of Stadis-450 (1% by volume) in octane. The complex distribution illustrated may be difficult to separate from that of an analyte. The spectrum of Stadis-450 is characterized by two pairs of overlapping distributions with peaks separated by 28 m/z indicating the presence of a polymer with a distribution of polymer chain lengths. Triethylamine was sprayed in octane in a separate experiment without the Statis-450 additive. In positive ion mode, protonated triethylamine appears at 102 m/z. The process leading to protonation of the amine in octane was not investigated, and may have involved trace impurities as the charge carriers in the droplet.

4.6. Conclusions

Heptane, octane, and *p*-xylene have discharge characteristics similar to those found for both large, low-volatility hydrocarbons and for traditional electrospray solvents. Successive discharge events observed for *n*-octane and *p*-xylene demonstrate no significant change in the percent charge lost for both *n*-octane and *p*-xylene. Size-charge correlations for heptane and octane show that smaller droplets discharge at a higher percent Rayleigh limit of charge than larger droplets. Over the size range studied, *p*-xylene discharges at a consistent charge relative to its Rayleigh limit.

The combination of appropriate conductivity and evaporation rates make these solvents attractive for electrospray mass spectrometry. The introduction of these hydrocarbon solvents may be important for mass spectrometry applications for analytes that do not dissolve easily in other solvents, or those already dissolved in a hydrocarbon solvent and not easily extracted into a more traditional electrospray environment. With a complicated spectrum, Stadis-450 is not an appropriate conductivity enhancing agent as it could interfere with the interpretation of analyte spectra.

4.7. Acknowledgements

The authors gratefully acknowledge Dr. J. N. Smith whose experimental designs and insight made the current investigation possible, and Dr. Mona Shahgholi for use of the mass spectrometry facility. This work was funded by grant CHE-9727566 of the National Science Foundation. In addition, we are grateful for support from the Beckman Institute at Caltech.

4.8. References

(1) Smith, J. N.; Flagan, R. C.; Beauchamp, J. L. *J. Phys. Chem. A* **2002**, *106*, 9957.

(2) Smith, J. N. Fundamental Studies of Droplet Evaporation and Discharge Dynamics in Electrospray Ionization, California Institute of Technology, 2000.

(3) Zhan, D.; Fenn, J. B. *Int. J. Mass Spectrom.* **2000**, *194*, 197.

(4) Hughey, C. A.; Rodgers, R. P.; Marshall, A. G. *Anal. Chem.* **2002**, *74*, 4145.

(5) Roussis, S. G.; Proulx, R. *Anal. Chem.* **2002**, *74*, 1408.

(6) Schalley, C. A.; Rivera, J. M.; Martin, T.; Santamaria, J.; Siuzdak, G.; Rebek, J. *Eur. J. Org. Chem.* **1999**, *6*, 1325.

(7) Hof, F.; Rebek, J., Scripps Research Institute, La Jolla, CA. Personal communication regarding the use of xylene as an electrospray solvent, 2001.

(8) Tang, K.; Gomez, A. *J. Colloid Interface Sci.* **1996**, *184*, 500.

(9) Gomez, A.; Tang, K. *Phys. Fluids* **1994**, *6*, 404.

(10) Duft, D.; Atchtzehn, T.; Muller, R.; Huber, B. A.; Leisner, T. *Nature* **2003**, *421*, 6919.

(11) Hager, D. B.; Dovichi, N. J.; Klassen, J.; Kebarle, P. *Anal. Chem.* **1994**, *66*, 3944.

(12) *CRC Handbook of Chemistry and Physics*; 76th ed.; Lide, D. R., Ed.; CRC Press: Boca Raton, FL, 1995.

(13) Taflin, D. C.; Ward, T. L.; Davis, E. J. *Langmuir* **1989**, *5*, 376.

(14) Davis, E. J.; Bridges, M. A. *J. Aerosol Sci.* **1994**, *25*, 1179.

(15) Davis, E. J. *Aerosol Science and Technology* **1997**, *26*, 212.

(16) Tang, K.; Smith, R. D. *International Journal of Mass Spectrometry* **1999**, *185/186/187*, 97.

(17) Fernandez de la Mora, J. *J. Colloid and Interface Sci.* **1996**, *178*, 209.

Chapter 5. Evaporation and discharge dynamics of highly charged two-component droplets generated by electrospray ionization

5.1. Abstract

We report studies of the Rayleigh discharge dynamics of charged two-component droplets consisting principally of methanol with either 2-methoxyethanol, *tert*-butanol, or *m*-nitrobenzyl alcohol. Phase Doppler anemometry (PDA) characterizes droplets generated by electrospray ionization according to size, velocity, and charge as they move through a uniform, linear electric field within an ion mobility cell. Repeated field reversals allow multiple PDA measurements of selected micron-sized droplets with up to 10^7 elementary positive charges. This "ping-pong" technique generates individual droplet histories from which we ascertain solvent evaporation behavior and the dynamics of mass and charge loss to progeny droplets during Rayleigh discharge events. On average, methanol discharges at 127% its Rayleigh limit and releases 25% of its net charge. Binary methanol droplets containing up to 50% *tert*-butanol discharge at a lower point than pure methanol and release a greater fraction of their net charge. Interestingly, methanol / *tert*-butanol droplets evaporate at a similar rate to pure methanol. Droplets of methanol / 2-methoxyethanol release a greater portion of their net charge as the fraction of 2-methoxyethanol in the droplets increase. These droplets evaporate at a rate similar to that of pure 2-methoxyetanol droplets. Mixed 99% methanol / 1% *m*-nitrobenzyl

alcohol droplets possess discharge characteristics similar to methanol, however 2% *m*-nitrobenzyl droplets evaporate down to a fixed size and charge that remains constant with no observable discharges. We compare these results to previous experiments, and discuss implications for the use of binary solvents in electrospray and field-induced droplet ionization mass spectrometry.

5.2. Introduction

Multi-component solvent systems are common in the electrospray mass spectrometry of biomolecules, yet questions remain regarding the mechanisms by which different solvent systems yield unique spectra of otherwise identical analytes. Electrospray ionization[1-3] is a popular tool in mass spectrometry because of its ability to generate low-energy, multiply charged biomolecules and molecular clusters.[4] In the electrospray process, an applied electric field induces charge separation in a solution flowing from a capillary needle. The resulting electrohydrodynamic forces draw the liquid to a point referred to as the Taylor cone that sprays a fine mist of charged droplets.[5] Mass spectrometric applications utilize the subsequent evaporation and discharge processes that ultimately yield desolvated gas phase ions or clusters. Despite the popularity of the technique, recent experiments present conflicting results regarding the dynamics and mechanisms involved.

Our current understanding of charged droplet instability and breakup begins with the seminal work of Lord Rayleigh. In 1882, he proposed that the repulsive force due to the net surface charge destabilizes the natural mode oscillations within a droplet. He postulated that the natural oscillation of a droplet becomes unstable when the net charge,

q, on a droplet of radius r and surface tension σ exceeds a critical value, q_R, given by eq (5.1).

$$q_R = 8\pi\varepsilon^{1/2}\sigma^{1/2}r^{3/2} \tag{5.1}$$

In (5.1), ε is the permittivity of the surrounding medium. He suggests the droplet emits fine jets of charged progeny when q exceeds q_R, but his analysis does little else to describe the dynamics of the event. Significant research has been performed to elucidate these mechanisms. In the consensus view, solvent evaporates from a highly charged micron-sized droplet until $q > q_R$ at which point the droplet distorts and emits jets of small, highly charged progeny droplets. The progeny droplets are typically 1-10% the diameter of the parent droplet. This Rayleigh discharge event has been visually confirmed showing one jet from methanol[6] and *n*-heptane[7] and two jets from ethylene glycol droplets.[8] Discharge events typically release 10 to 40% of a droplet's net charge but only 1 to 5% of a droplet's mass.[4]

In the nanometer size regime, researchers propose two competing mechanisms for discharge events. Dole's original charge residue model (CRM) suggests the process of evaporation and Rayleigh discharge-like events continues until the formation of desolvated ions.[9] Iribarne and Thomson propose the ion evaporation model (IEM) where the surface electric field due to excess charge is sufficient to desorb ions directly from the surface of the nanodroplet.[10]

Recent mass spectrometry studies of analytes dissolved in multi-component solvents have had profound implications for the understanding of these evaporation and discharge mechanisms. Williams and co-workers note a correlation between solution surface tension and the charge-state distribution of electrosprayed polymers and biomolecules in the gas-phase. Terming the phenomenon "supercharging," they note the addition of *m*-nitrobenzyl alcohol ($\sigma \sim 0.050$ N m^{-1}) significantly increases the charge state distributions of poly(ethylene glycol) dendrimers sprayed from methanol ($\sigma = 0.022$ N m^{-1}) yet decreases the charge state distribution of the dendrimers sprayed from water ($\sigma = 0.072$ N m^{-1}).[11-13] In contrasting experiments, Samalikova and Grandori report no change in the charge state distribution of denatured proteins upon the addition of *n*-propanol ($\sigma = 0.072$ N m^{-1}) to aqueous solutions.[14] The conflicting results suggest that more research is necessary to understand the processes that govern charging of analytes in electrospray mass spectrometry. Such studies motivate the present investigation.

We report the evaporation and discharge dynamics of ten binary solvent systems comprised of methanol with either *tert*-butanol, 2-methoxyethanol, or *m*-nitrobenzyl alcohol, shown in Table 5.1. Discharges are characterized by measuring the droplet diameter and charge, the charge lost in the event, and the charge as a function of the Rayleigh limit at the time of the event. Binary droplet evaporation is compared to the single-component evaporation model discussed in Chapter Three. Concisely, evaporation of micron-sized droplets is dominated by the rate at which vapor diffuses away from the droplet surface. Equation (5.2) determines the evaporation rate for single-component droplets.[15]

$$\frac{d}{dt}d_{\mathrm{p}} = \frac{-4D_{ij}\left(T_{\mathrm{p}}\right)M}{R\rho_{\mathrm{p}}d_{\mathrm{p}}}\frac{p_{\mathrm{p}}\left(T_{\mathrm{p}}\right)}{T_{\mathrm{p}}} \tag{5.2}$$

In eq (5.2), solvent-specific parameters include $D_{ij}(T_{\mathrm{p}})$, the temperature-dependent diffusivity of solvent vapor i in gas j, solvent molar mass M, droplet density ρ_{p}, and equilibrium vapor pressure, $p_p(T_p)$, at equilibrium surface temperature T_p, while R is the gas constant. The equilibrium surface temperature is depressed relative to the ambient temperature, T_∞, because evaporation is spontaneous yet endothermic. Equation (5.2) is simplified from a more rigorous model in which solvent vapor in the ambient gas inhibits evaporation. Experimentally, a constant flow of dry nitrogen gas washes through the apparatus flushing solvent vapor allowing this simplification. Integrating the evaporation rate yields eq (5.3).

$$d_p^2 = d_o^2 + st \tag{5.3}$$

Thus a plot of d_p^2 versus time is linear with intercept d_o^2 and slope s containing the solvent-specific parameters given by eq (5.4). Spontaneous evaporation is endothermic, lowering the surface temperature below that of the ambient gas.

$$s = -\frac{8D_{ij}(T_p)M}{R\rho_p}\frac{p_p(T_p)}{T_p} \tag{5.4}$$

Evaporation models of multicomponent droplets require solving the equations for heat and mass transfer at the droplet-gas interface as well as the diffusion through the liquid and convective diffusion of the solvent vapor in air. Diffusion through the liquid is generally orders-of-magnitude slower than diffusion through air suggesting the presence of concentration gradients within the droplet. This is confirmed by calculating the Biot number, Bi, which is the ratio of the time scale for self-diffusion in the liquid to the time scale of convective diffusion of the solvent molecules in air. Following a derivation similar Clark, eq (5.5) estimates the Biot number for the evaporation of methanol from a pure, 40 μm diameter droplet.[16] In eq (5.5), k_c represents the mass transfer coefficient under Stokes flow and is given by eq (5.6).

$$\mathrm{Bi} = \frac{d_{\mathrm{p}} k_c}{2D_{ij}} \tag{5.5}$$

$$k_c = \frac{D_{ij}}{2a}\left[0.92 + 0.991(\mathrm{Sc\ Re})^{1/3}\right] \tag{5.6}$$

In eq (5.6), Re is the Reynolds number and Sc is the Schmidt number. For methanol, $D_{ij} = 0.13$ cm^2 s^{-1}, Sc = 1.13, and Re ~ 0.2 at the terminal settling speed of a 40 μm diameter droplet. As a result, Bi ~ 5000 indicating the time scale of internal diffusion is significantly greater than the time scale of external, convective diffusion.

There are no exact solutions for the general case of binary droplet evaporation. As a result, models of multi-component evaporation frequently employ simplifying assumptions. Davis et al. study low vapor pressure oils that evaporate nearly isothermally.[17-20] Simplified models accurately predict the evaporation behavior of these oils. For the volatile solvents considered in this study, quasi-steady state models approximate the evaporation dynamics. In quasi-steady state evaporation, droplets exposed to air initially undergo a period of unsteady evaporation while the surface temperature decreases to an equilibrium value.[21] At the equilibrium temperature depression, a binary droplet evaporates at a "constant composition mixture."[22] In other words, the composition of the droplet is said to be in a quasi-steady state. The rate of evaporation in this state is proportional to the droplet surface area. Thus eq (5.3) models the droplet size, however *s* becomes a multi-component function of bulk parameters for both components as well as the activity coefficients for the two-component system. We compare the binary component slopes, *s*, from a linear regression of d_{p}^2 versus *t* to the corresponding values for pure droplets of the component species.

5.3. Experimental Section

Rather than use an electrodynamic balance, where the electric forces balance the force of gravity to trap and hold droplets, we employ an ion mobility spectrometer (IMS). In our IMS, $qE \neq mg$ and droplets are dragged through a linear electric field while being characterized according to size, equilibrium velocity, and net charge using a phase Doppler anemometer (PDA).

Chapter Three describes the ping-pong apparatus and equations of motion in detail. Only deviations and specific implementations are discussed. Briefly, the instrument consists of three parts: the electrospray source that generates charged droplets in the 10-100 μm size range, the mobility cell (often referred to as a drift cell or the drift region), and a phase Doppler anemometer (PDA) that characterizes droplet size, velocity and charge. An electric field initially directs positively charged droplets upward through the cell. When the PDA detects a droplet, the electric field reverses and droplets travel downward through the cell. Repeated field reversals cause the detected droplet to “ping-pong” through the measurement volume providing a temporal profile of droplet size, velocity, and charge for that droplet. Following this acquisition, the field resets so that droplets travel upwards for the analysis of another droplet. Typically, highly charged droplets take ~200 ms to travel the 10 cm distance between the electrospray source and the PDA measurement volume, and are subsequently characterized every 10 ms.

The methanol (HPLC grade, EM Science), glycerol (99.5%, EM Science), *tert*-butanol (99%, Sigma Aldrich), 2-methoxyethanol (98%, Sigma Aldrich), and *m*-nitrobenzyl alcohol solvents were used without further purification. The electrospray needle was held 2 mm from the first aperture in the IMS and maintained at 850 V for neat methanol and between 900 and 1150 V for the binary solvent systems. In each case, solution flow rates were 0.5 – 2 mL min^{-1} and dry nitrogen gas flowed downward through the cell at 0.3 L min^{-1} or 0.6 cm s^{-1}. The voltages, needle positions, and flow rates resulted in a metastable electrospray of micron-sized droplets. Higher voltages and electric fields result in cone-jet electrosprays that generate droplets too small for detection by the PDA.

5.4. Results

Binary systems consisting of methanol / 2-methoxyethanol, methanol / *tert*-butanol, and 99% methanol / 1% *m*-nitrobenzyl alcohol showed Rayleigh discharge phenomena. These droplets were initially 30-50 μm in diameter and generally carried a nascent charge of 60-90% q_R from the electrospray source. Droplets consisting of 98% methanol / 2% *m*-nitrobenzyl alcohol showed no discharge events but rather evaporated to down to a size and charge that remained constant for up to 500 ms. These droplets were initially 5-20 μm in diameter with a nascent charge of 40-60% q_R. Because of their different behavior, binary systems showing Rayleigh discharge are presented and discussed separately from the 98% methanol / 2% *m*-nitrobenzyl alcohol droplets.

5.4.1. Droplets with observed Rayleigh discharge events

Figure 5.1 shows a representative history for a single droplet of 75% methanol and 25% 2-methoxyethanol undergoing multiple Rayleigh discharges. When first characterized, the droplet is roughly 32 μm in diameter (frame A) with ~4.2×10^6 elementary charges (C). This corresponds to roughly 95% the Rayleigh limit for methanol (D). In repeated observations through 0.2 s, the droplet's diameter decreases and the speed (B) increases. The speed increase is due to the constant electrical force, qE, becoming proportionally greater than the force of gravity $m_p g$, which is decreasing as the droplet loses mass to evaporation. The small oscillations in speed are due to the droplet traveling upwards against gravity more slowly than traveling downward with gravity. We attribute the diameter oscillations to the change in the relative refractive index between droplets traveling upwards through dry gas and droplets traveling downwards through solvent-saturated gas.

During the first 0.2 seconds of acquisition, the charge remains constant (C) and the percent Rayleigh limit (D) increases due to constant charge and decreasing size. At 0.2 s after the initial characterization, the charge decreases suddenly resulting in a decrease in velocity and the percent Rayleigh limit. Conversely, there is no significant decrease in mass loss at this time. We interpret this sudden charge loss to be a Rayleigh discharge event. The droplet presented in Figure 5.1 shows six such discharges represented by arrows.

Discharge dynamics are classified according to charge loss and the percent Rayleigh limit. The change in average charge between discharge events classifies the charge loss as shown by dotted lines in Figure 5.1C. The percent Rayleigh limit at discharge is simply the last recorded value before the sharp decrease characteristic of a discharge event.

Evaporation dynamics are described by a slope of diameter squared versus time as computed by a linear regression and residual plots of the regressions show no trend. The dotted curve in Figure 5.1A demonstrates this fit corresponding to s ~ 1200 $\mu m^2 s^{-1}$.

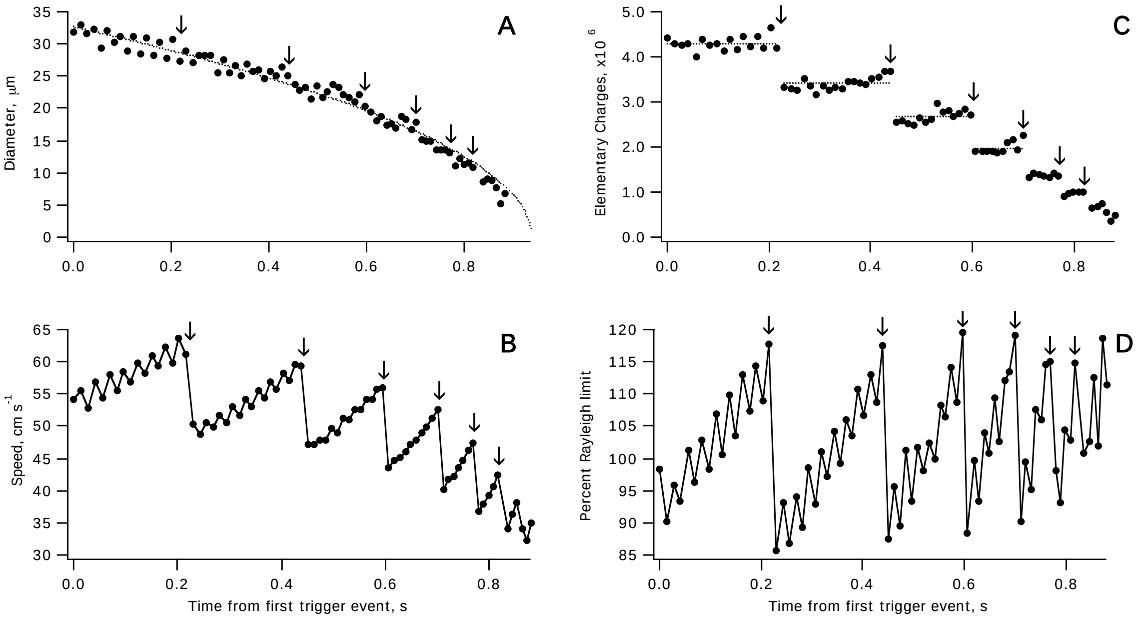

Figure 5.1. Acquired history of a 75% methanol 25% 2-methoxyethanol droplet including size (A), velocity (B), charge (C), and percent Rayleigh limit (D). As the droplet evaporates, its speed increases and charge stays constant until a discharge event. The six observed events (indicated by arrows) occur at ~120% the Rayleigh limit for methanol and are characterized by loss of ~25% of the droplet charge and an undetectable mass loss.

Table 5.1 summarizes the charge loss and evaporation characteristics of the nine binary systems showing Rayleigh discharge events. Previous results for single-component droplets of hydrocarbon solvents *n*-heptane, *n*-octane, and *p*-xylene[23] and of traditional electrospray solvents methanol, water, and acetonitrile,[24] show no correlation between droplet size and the percent charge lost in a Rayleigh discharge event. Binary droplets do demonstrate a correlation as is illustrated in Figure 5.2 for methanol / *tert*-butanol, in Figure 5.3 for methanol / 2-methoxyethanol, and in Figure 5.4 for 99% methanol / 1% *tert*-butanol. In each of these binary systems, smaller droplets eject a larger percent of their net charge than the larger droplets. As a result of the size – charge loss correlation, the average charge loss values reported in Table 5.1 are not rigorous but rather serve as a rapid summary of the Rayleigh discharge phenomena for binary systems.

Percent Rayleigh limit data for the binary systems is reported as the percent Rayleigh limit of methanol because the droplet composition is not known *a priori*. The unknown density and refractive index each introduce a small ~5% error in the diameter and charge assignments, however the unknown surface tension prohibits an exact determination of q_R by eq (5.1) and the percent Rayleigh limit at a discharge event. For all binary systems, surface tension is taken as bulk methanol value, $\sigma = 0.022$ N m^{-1}. All other components have $\sigma > 0.022$ N m^{-1} so computed q_R values are a *lower* bound and the reported percent Rayleigh limit at discharge, $100\% \times q/q_R$, in Table 5.1 and Figures Figure 5.2 through Figure 5.4 represents an *upper* bound.

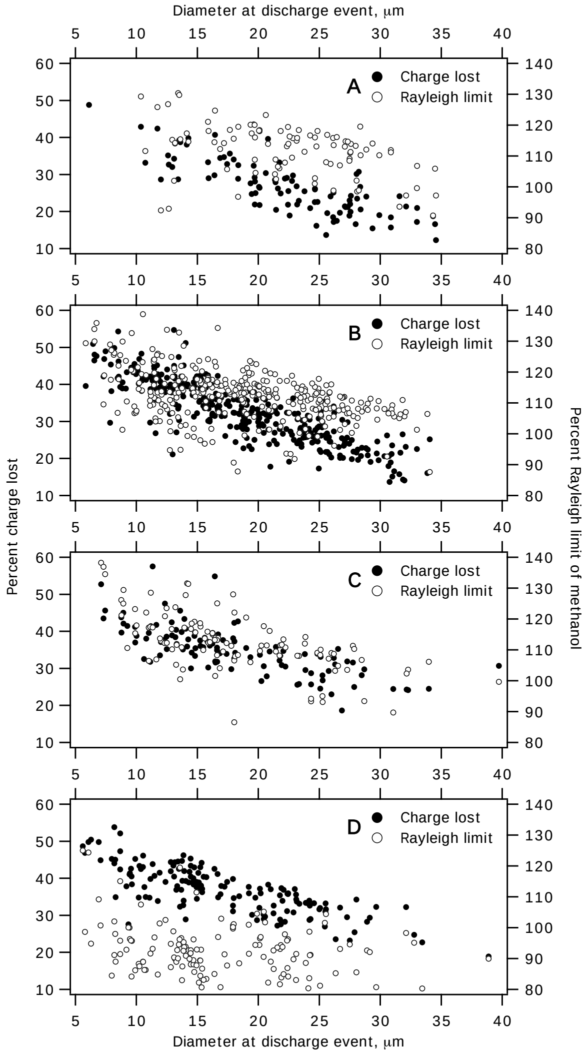

Figure 5.2. Percent charge lost (closed circle) and percent Rayleigh limit (open circles) versus the diameter at discharge for 5% (A), 10% (B), 25% (C) and 50% (D) *tert*-butanol droplets. The distribution in each system shows a dependence on droplet size with larger droplets ejecting less of their net charge than the smaller droplets.

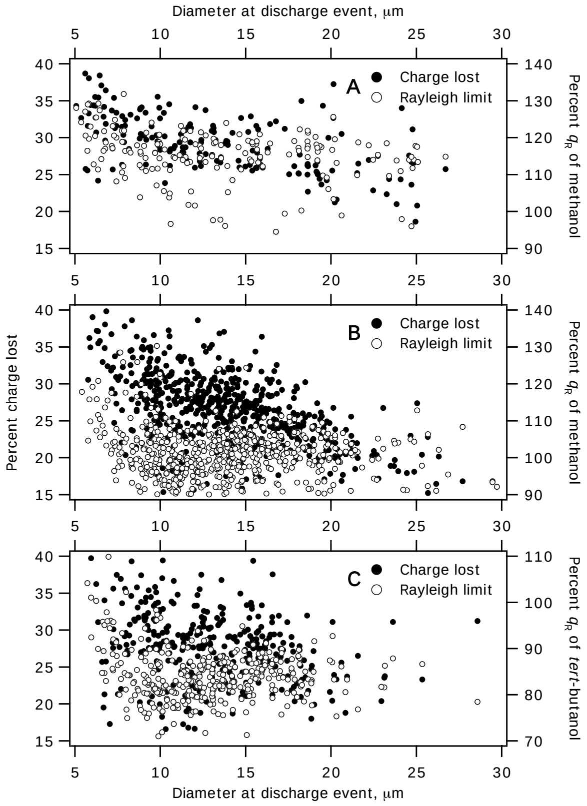

Figure 5.3. Percent charge lost (closed circle) and percent Rayleigh limit (open circles) versus the diameter at discharge for 25% (A), 50% (B), and 100% (C) 2-methoxyethanol droplets. The distribution in each the binary systems (A) and (B) shows a dependence on droplet size while pure 2-methoxyethanol (C) shows no correlation between charge loss and droplet size.

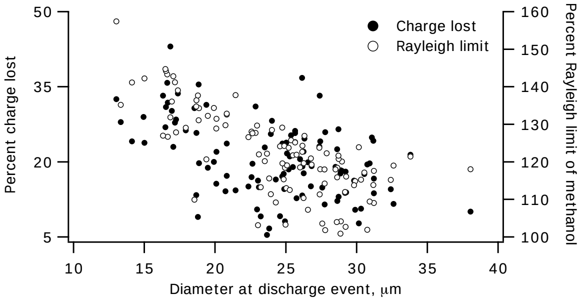

Figure 5.4. Percent charge lost (closed circle) and percent Rayleigh limit (open circles) versus the diameter at discharge for 99% methanol / 1% *m*-nitrobenzyl alcohol droplets. The distribution in each system shows a dependence on droplet size with larger droplets ejecting less of their net charge than the smaller droplets.

5.4.2. Droplets with no Rayleigh discharge events

Droplets of 98% methanol / 2% *m*-nitrobenzyl alcohol show no Rayleigh discharge events, but rather evaporation down to a size that remained fixed for the duration of the characterization. Figure 5.5 shows representative data for a droplet with 2% *m*-nitrobenzyl alcohol. Droplet size (Figure 5.5A) decreases steadily for the first 0.25 s while both the velocity (B) and the percent Rayleigh limit (D) increase consistently with solvent evaporation. For the remainder of the acquisition, all values remain constant. Droplet charge (C) is constant for the entire acquired lifetime of the droplet.

5.5. Discussion

5.5.1. Evaporation dynamics and mass loss in a discharge event

Droplet diameter decreases in time due to solvent evaporation as is evident in Figure 5.1. Within the accuracy of the measurements, no observable additional decrease in size accompanies the discharge events. Based on uncertainties in the diameter measurements, previous studies in our laboratory bound the maximum change in diameter in a Rayleigh discharge event at 4%.[23]

Table 5.1 shows the evaporation of pure methanol droplets (s = -4350 μm^2 s^{-1}) and pure 2-methoxyethanol droplets (s = -2300 μm^2 s^{-1}) agree well with the theoretical values. In the case of the methanol / *tert*-butanol droplets, calculated s values are remarkably similar to pure methanol. In contrast, droplets of methanol / 2-methoxyethanol show evaporation rates similar to pure 2-methoxyethanol. In all cases, plots of d^2 are linear with respect to time indicating that eq (5.3) accurately models the droplets, which are undergoing quasi-steady state evaporation.

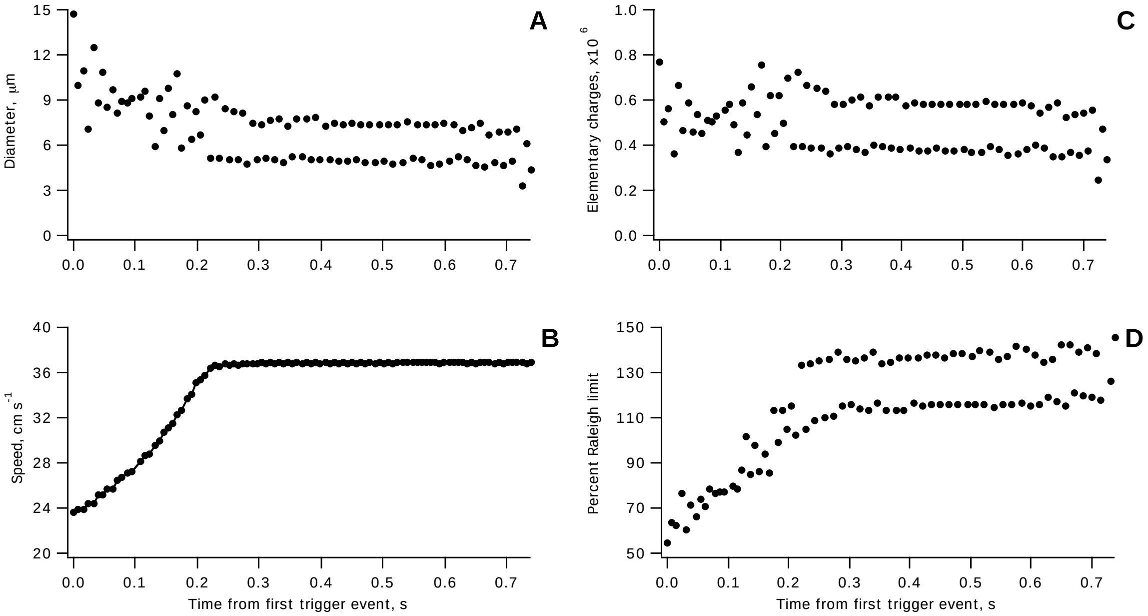

Figure 5.5. Acquired history of a methanol droplet with 2% *m*-nitrobenzyl alcohol. The droplet is initially charged at 50% of its Rayleigh limit and evaporates for ~0.25 s after the initial acquisition. With the droplet no longer evaporating after ~0.25 s, all values remain constant for the remainder of the acquisition sequence.

5.5.2. Correlation between droplet size and charge loss

The percent charge loss for the binary droplets studied is generally between 5 and 40%. When *tert*-butanol and 2-methoxyethanol are added to methanol the percent charge lost in a discharge event increases. Table 5.1 demonstrates that the average charge loss for pure methanol droplets is ~25%, however the addition of *tert*-butanol increases the average charge loss up to ~37%. The surface tension of pure *tert*-butanol is 0.020 N m^{-1} compared to 0.022 N m^{-1} for methanol indicating that surface tension is not a decisive parameter for this change. On the other hand, the addition of 2-methoxyethanol results in a small increase to 27-29% charge lost which is roughly identical to the ~28% charge lost from pure 2-methoxyethanol droplets.

Figure 5.2 through Figure 5.4 show a correlation between the size of the droplet and the percent charge lost in a discharge event. For binary systems, larger droplets consistently lose a lower fraction of their net charge than smaller droplets. For droplets that undergo sequential discharge events such as the droplet in Figure 5.1, we generally observe an average increase of 15%. Previous studies on pure droplets demonstrate that the percent charge loss in an event is roughly proportional to the surface tension of the liquid. Generally, hydrocarbon solvents eject ~18% of their net charge[23], alcohols and glycols eject ~20-30% of their charge,[8,24,25] and water ejects 20-40% of its net charge.[24] The percent of charge lost from droplets of pure solvents is consistent over the range of sizes studied, both in previous investigations,[23,24] and for pure methanol and 2-methoxyethanol in this experiment.

The size dependence of charge loss indicates the physical parameters controlling charge loss are changing as the droplets evaporate and discharge. We attribute this to one of two possible explanations. First, droplets may not be in a quasi-steady state as they evaporate even though their diameter is well described by (5.3). Future work may address this with a rigorous theoretical treatment regarding the evaporation of the droplets studied in this experiment. The other, more likely, possibility is that the discharge events are disrupting the quasi-steady state evaporation. Before a discharge event, the composition of the surface is significantly different from that of the bulk. As a result, the discharge events remove a small amount of mass from the surface disrupting the steady state and changing the overall physical parameters of the droplet. This too may be simulated through theoretical models of binary droplet evaporation with the periodic removal of surface mass from a simulated, evaporating droplet. This would also predict how the components fractionate between the parent and progeny from a discharge event, which is not measured in this experiment.

5.5.3. Droplets with no Rayleigh discharge events

Droplets of 98% methanol and 2% *m*-nitrobenzyl alcohol show no discharge events, but rather, they evaporate to a constant size and charge. These droplets are generally smaller than other droplets studied and carry significantly lower initial net charge relative to the Rayleigh limit. Droplets initially possess 40-60% the Rayleigh limit of charge and stop evaporating before reaching the 125% q_R point at which methanol droplets undergo Rayleigh discharge in our apparatus.

The small nascent charge results in correspondingly small initial velocities of ~20 cm/s suggesting droplets travel for 500 ms between production and their initial characterization. If the droplets evaporate at $s = –4350\ \mu m^2\ s^{-1}$, the nascent droplet diameter would be ~60 μm. Thus droplets that "freeze" have lost roughly 90% of their diameter which corresponds to 99.9% volume loss. This indicates that these droplets evaporate to a "core" comprised almost entirely of the low volatility *m*-nitrobenzyl alcohol component.

5.5.4. Implications for electrospray mass spectrometry

Iavarone and Williams suggest that the supercharging phenomenon manifests itself late in the droplet evaporation and discharging process when discharge is explained by the CRM or IEM.[11-13] However, observations of size-dependent charge loss in this experiment indicate that the Rayleigh discharge events of nascent electrospray droplets may have an effect on those droplets. Thus the entire lifetime of evaporation and discharge is important for explaining charge state distributions of analytes of multi-component solutions as well as the supercharging phenomenon.

The Rayleigh discharge dynamics for 99% methanol / 1% *m*-nitrobenzyl alcohol resemble that of pure methanol whereas observations of the 98% / 2% mixture shows profoundly different behavior. This indicates that small changes in the *m*-nitrobenzyl alcohol concentration have a profound impact on droplet dynamics. This agrees well with the supercharging phenomenon which results in a significant change in the charge state distribution of biomolecules and poly(ethylene glycol) dendrimers with the initial addition of 1 to 5% *m*-nitrobenzyl alcohol. Exploring the discharge dynamics of the 98% / 2% system at elevated temperatures and longer acquisitions may reveal the Rayleigh discharge dynamics relevant to electrospray mass spectrometry.

5.6. Conclusions

Understanding the evaporation and discharge dynamics of binary droplets is critical to knowing and controlling the charge state distributions of biomolecules and clusters studied in electrospray mass spectrometry. Many studies demonstrate that the charge state distribution of biomolecules changes depending on the solvent system that is electrosprayed. Studies of Rayleigh discharge in droplets of methanol and *tert*-butanol demonstrate an increase in the charge lost in a discharge event with increasing initial quantities of *tert*-butanol. Conversely, droplets of methanol and 2-methoxyethanol show evaporation and discharge dynamics similar to that of pure 2-methoxyethanol.

Methanol evaporates significantly more rapidly than *m*-nitrobenzyl alcohol. Evaporation of 99% methanol / 1% *m*-nitrobenzyl alcohol shows evaporation and discharge dynamics similar to those of pure methanol, however 98% / 2% droplets show no observable Rayleigh discharge events. Thus small changes in the initial concentrations of *m*-nitrobenzyl alcohol have profound implications for the discharge dynamics and electrospray mass spectrometry.

5.7. Acknowledgements

The authors gratefully acknowledge Dr. J. N. Smith whose experimental designs and insight made the current investigation possible, and Dr. Richard Flagan for his valuable discussions. This material is based on work supported by the National Science foundation under grants CHE-9727566 and CHE-0416381 and support from the Beckman Institute at Caltech.

system	percent charge lost	percent Rayleigh limit*	experim. slope, *s* ($\mu m^2\ s^{-1}$)
methanol	25 ± 7	127 ± 12	-4350 (-4750)
95% methanol 5% *tert*-butanol	27 ± 7	112 ± 9	-4400
90% methanol 10% *tert*-butanol	32 ± 9	113 ± 9	-4300
75% methanol 25% *tert*-butanol	35 ± 7	113 ± 11	-4400
50% methanol 50% *tert*-butanol	37 ± 7	91 ± 10	-4500
75% methanol 25% 2-methoxyethanol	29 ± 4	116 ± 7	-1500
50% methanol 50% 2-methoxyethanol	27 ± 7	102 ± 13	-2000
100% 2-methoxyethanol	28 ± 7	85 ± 7	-2300 (-1925)
99% methanol 1% *m*-nitrobenzyl alcohol	21 ± 8	123 ± 14	-4500

Table 5.1. Experimental charge loss, percent Rayleigh limit at discharge, and evaporation values for binary systems characterized by the "ping-pong" technique. Evaporation slope values in parenthesis represent calculated values from thermodynamic parameters.

5.8. References

(1) Yamashita, M.; Fenn, J. B. *J. Phys. Chem.* **1984**, *88*, 4451.

(2) Yamashita, M.; Fenn, J. B. *J. Phys. Chem.* **1984**, *88*, 4671.

(3) Fenn, J. B.; Mann, M.; Meng, C. K.; Wong, S. F.; Whitehouse, C. M. *Science* **1989**, *246*, 64.

(4) *Electrospray Ionization Mass Spectrometry*; Cole, R. B., Ed.; John Wiley and Sons: New York, 1997.

(5) Taylor, G. *Proc. R. Soc. London, Ser. A* **1964**, *280*, 383.

(6) Hager, D. B.; Dovichi, N. J.; Klassen, J.; Kebarle, P. *Anal. Chem.* **1994**, *66*, 3944.

(7) Gomez, A.; Tang, K. *Phys. Fluids* **1994**, *6*, 404.

(8) Duft, D.; Atchtzehn, T.; Muller, R.; Huber, B. A.; Leisner, T. *Nature* **2003**, *421*, 6919.

(9) Dole, M.; Mack, L. L.; Hines, R. L.; Mobley, R. C.; Ferguson, L. D.; Alice, M. B. *J. Chem. Phys.* **1968**, *49*, 2240.

(10) Thomson, B. A.; Iribarne, J. V. *J. Chem. Phys.* **1979**, *71*, 4451.

(11) Iavarone, A. T.; Jurchen, J. C.; Williams, E. R. *J. Am. Soc. Mass Spectrom.* **2000**, *11*, 976.

(12) Iavarone, A. T.; Williams, E. R. *Int. J. Mass Spectrom.* **2002**, *219*, 63.

(13) Iavarone, A. T.; Williams, E. R. *J. Am. Chem. Soc.* **2003**, *125*, 2319.

(14) Samalikova, M.; Grandori, R. *J. Am. Chem. Soc.* **2003**, *125*, 13352.

(15) Hinds, W. C. *Aerosol Technology: Properties, Behaivor, and Measurement of Airborne Particles*, 2nd ed.; John Wiley & Sons, Inc.: New York, 1999.

(16) Clark, M. M. *Transport Modeling for Environmental Engineers and Scientists*; Wiley Interscience: New York, 1996.

(17) Ravindran, P.; Davis, E. J. *J. Colloid Interface Sci.* **1982**, *85*, 278.

(18) Buehler, M. F.; Allen, T. M.; Davis, E. J. *J. Colloid and Interface Sci.* **1991**, *146*, 79.

(19) Allen, T. M.; Taflin, D. C.; Davis, E. J. *Ind. Eng. Chem. Res.* **1990**, *29*, 682.

(20) Widmann, J. F.; Davis, E. J. *Aerosol Sci. Technol.* **1997**, *27*, 243.

(21) Newbold, F. R.; Amundson, N. R. *AIChE J.* **1973**, *19*, 22.

(22) Ray, A. K.; Venkatraman, S. *AIChE J.* **1995**, *41*, 938.

(23) Grimm, R. L.; Beauchamp, J. L. *Anal. Chem.* **2002**, *74*, 6291.

(24) Smith, J. N.; Flagan, R. C.; Beauchamp, J. L. *J. Phys. Chem. A* **2002**, *106*, 9957.

(25) Duft, D.; Lebius, H.; Huber, B. A.; Guet, C.; Leisner, T. *Phys. Rev. Lett.* **2002**, *89*, art. no. 084503.

Chapter 6. Neutral droplets in high electric fields as a source of ions. Introduction to field-induced droplet ionization mass spectrometry

Adapted from Grimm, R. L. and Beauchamp, J. L. *J. Phys. Chem. B.* **2003**, *107*, 14161.

6.1. Abstract

A neutral droplet elongates along the axis of a strong electric field, ejecting opposing jets of positively and negatively charged progeny droplets. Images of droplets from a vibrating orifice aerosol generator illustrate this phenomenon, and mass spectrometric sampling of the progeny droplets demonstrates that they are a viable source of desolvated gas-phase ions. Field induced droplet ionization (FIDI) mass spectra are presented for several species, including tetraheptylammonium cation, deprotonated benzene tetracarboxylic acid anion, and multiply protonated cytochrome *c*.

6.2. Letter

We report a method for generating desolvated ions in the gas phase, based on neutral droplet instability in strong electric fields. This experimental methodology facilitates new applications of mass spectrometry to problems in chemistry and biology. In a sufficiently high electric field, neutral droplets elongate parallel to the field, developing two opposing conical tips that emit fine jets. These jets break up into droplets that we assume are charged opposite of the electrode to which they are attracted. We demonstrate that the progeny droplets formed by field-induced droplet ionization (FIDI) comprise a viable source of ions for mass spectrometric analysis.

Early explorations into the effect of electric fields on water droplets and soap films led to eq (6.1) for the electric field E necessary to induce an instability leading to a discharge event in a drop or film of radius r.[1-5] In eq (6.1), σ is the surface tension of the liquid, ε_o is the permittivity of free space, and c is an experimentally determined parameter. Seminal theoretical work on droplets in electric fields is due to Taylor.[5,6] His leaky dielectric model predicts that droplets elongate into prolate ellipsoids, axisymmetric with the applied electric field. At a critical electric field referred to as the Taylor limit, the prolate shape becomes unstable leading to the formation of fine jets.

$$E^2 = c\frac{\sigma}{4\pi\varepsilon_0 r} \tag{6.1}$$

Elaborating the simplified analysis that led to eq (6.1) and theoretically modeling droplet deformation and breakup phenomena is still an active field of research in fluid dynamics.[7-11] Experimental investigations of suspended droplets are in general agreement with Taylor's theoretical predictions.[12,13] Small experimental deviations from theory are evident in the independent investigations due to Nolan[3] and Macky[4] of water droplets passing through an electric field. Both observed discharge events occurring at electric field strengths somewhat lower than predicted theoretically. Taylor suggested aerodynamic effects might have been responsible for the discrepancies[5] since the droplets were falling in air. With theoretical and experimental investigations focused on parent droplets and their instability in strong electric fields, the properties of progeny droplets formed in the process have been largely ignored.

In the present study, we demonstrate that progeny droplets are a viable source of both positively and negatively charged gas-phase ions for mass spectrometric analysis. Droplets are imaged using a pulsed xenon flashlamp in combination with a high-resolution CCD camera while the emitted jets are characterized using mass spectrometry. Figure 6.1 shows a schematic of the experimental arrangement. We chose methanol because equation (6.1) suggests its lower surface tension (0.022 N m^{-1} versus 0.072 N m^{-1} for water) requires lower electric fields to reach the Taylor limit. A vibrating orifice aerosol generator (VOAG) generates ~170 μm diameter methanol droplets at 17.3 kHz. Droplets pass between two parallel plate electrodes spaced 1.4 mm apart that define the electric field. The left hand electrode is electrically grounded while the right hand electrode is held at high voltage. The xenon flashlamp is synchronized with the VOAG to illuminate the droplets at fixed positions.

Figure 6.2 shows the deformation of a methanol droplet with jet formation in a 2.2×10^6 V m^{-1} electric field. This is similar to the 2.3×10^6 V m^{-1} field suggested from Macky's analysis[4] but lower than the 2.5×10^6 V m^{-1} field calculated from Taylor's theory[5] when applied to 170 μm methanol droplets. We do not explain this difference except to note that our experiment is conducted on moving droplets similar to Nolan[3] and Macky.[4] The field stretches the droplets into prolate ellipsoids with two opposing conical tips ejecting oppositely charged jets of methanol progeny droplets. This is visually similar to the symmetrical Rayleigh discharge process observed by Leisner and coworkers for ethylene glycol droplets,[14] although that event results in the ejection of

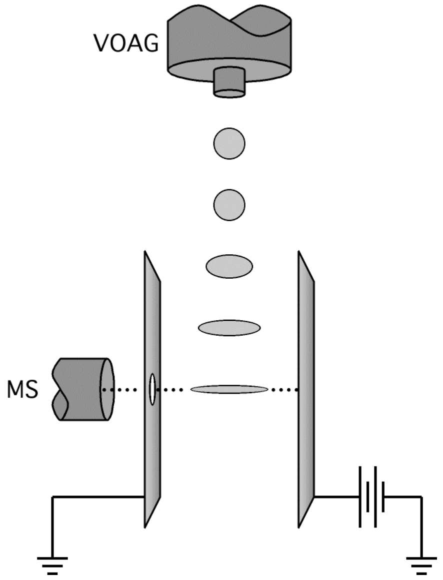

Figure 6.1. Experimental arrangement for FIDI-MS. A vibrating orifice aerosol generator (VOAG) produces droplets that pass through an electric field defined by two parallel plate electrodes. The electrode on the left is held at ground while the one on the right is held at high voltage. Droplets elongate and symmetrically emit two oppositely charged jets towards the electrodes. The jet directed at the left hand plate passes through an aperture to be sampled by a mass spectrometer (MS).

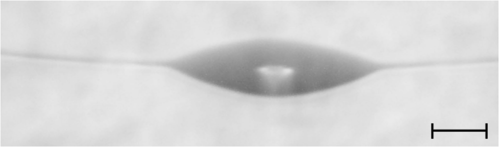

Figure 6.2. Image of a single 170 μm diameter methanol droplet illustrating jets formed at conical tips with a field strength of 2.2×10^6 V m^{-1}. The droplet, moving downward in the figure, is illuminated by a single pulse from a xenon flashlamp and imaged through a microscope onto a high-resolution CCD camera. Aerodynamic drag is responsible for the slight upward curvature of the two progeny jets. The bar indicates 100 microns.

similarly charged jets from a parent droplet with an overall net charge. This contrasts with unsymmetrical Rayleigh discharge events observed for droplets charged by a corona discharge[15,16] or electrospray ionization[17] in high electric fields.

Mass spectrometry supports the conjecture of the formation of oppositely charged jets. An aperture within one plate allows an aligned desolvation capillary inlet of a mass spectrometer (Figure 6.1) to sample the progeny droplets. In principle, a pair of mass spectrometers may simultaneously sample the positive and negative progeny droplets. In the single mass spectrometer configuration, positive ions are sampled using positive high voltage on the right hand plate. Similarly, the mass spectrometer samples negative progeny when the right hand plate is held at negative high voltage. A Finnigan LCQ Classic ion trap mass spectrometer with a custom-built desolvation capillary extension is employed for mass analysis.

To demonstrate that both positive and negative ions may be sampled from the same droplet, we tested a combined solution of 100 μM tetraheptylammonium bromide (THAB) and 100 μM 1,2,4,5 benzene tetracarboxylic acid (BTCA) in methanol under identical VOAG conditions and identical but reversed electric fields for both positive and negative ions. In positive ion mode (Figure 6.3a), the mixed THAB/BTCA solution mass spectrum exhibits the tetraheptylammonium ion peak at 410 m/z and the bromide-bound tetraheptylammonium dimer at 900 m/z. In negative ion mode (Figure 6.3b), we observe a peak at 253 m/z indicative of singly deprotonated BTCA, and a peak at 662 m/z attributed to a doubly deprotonated BTCA anion complexed to a tetraheptylammonium cation. Each spectrum is consistent with mass spectra acquired for this solution with a

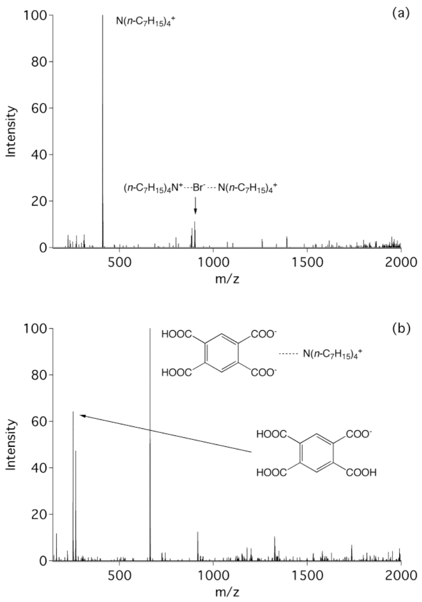

Figure 6.3. Positive ion (a) and negative ion (b) mass spectra of a solution of 100 μM THAB and 100 μM 1,2,4,5 BTCA. The positive ion spectrum consists of the tetraheptylammonium ion at 410 m/z and the bromide-bound tetraheptylammonium dimer at 900 m/z. The singly deprotonated BTCA species at 253 m/z and a doubly deprotonated BTCA - tetraheptylammonium cation adduct at 662 m/z dominate the negative ion mass spectrum.

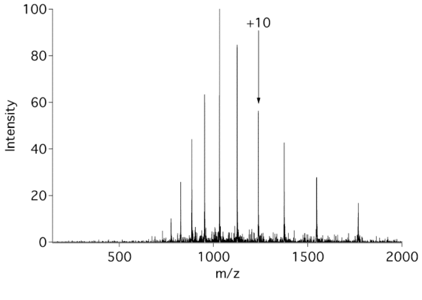

Figure 6.4. Horse heart cytochrome *c* mass spectrum of a 20 μM solution in 80% methanol, 20% water, and 0.1% acetic acid. The broad distribution of charge states acquired with the FIDI-MS technique closely resembles the positive-mode ESI mass spectrum of the same solution.

conventional electrospray ionization (ESI) source, including the expected isotopic distributions. We additionally tested a 20 μM solution of horse heart cytochrome *c* in 80% methanol, 20% water, and 0.1% acetic acid (Figure 6.4). The peak distribution in Figure 6.4 resembles that observed in an ESI mass spectrum of the same solution.

Droplet discharge events induced by strong electric fields are a route to charged progeny droplets and gas phase ions through a process we call field induced droplet ionization, or FIDI. Other methods used to sample ionic components of neutral droplets include injecting them into a corona discharge, where they become highly charged,[16] or allowing them to fuse with highly charged droplets formed by electrospray.[18] In both instances, subsequent events leading to desolvated ions are the same as in ESI. The mass spectra from FIDI-MS resemble ESI mass spectra. However, the possibility of simultaneously extracting both positive and negative ions from a neutral droplet, without the constraint of the capillary needle required for ESI-MS, opens avenues in chemical and biological research unavailable with current techniques. For example, environmental studies involving the real-time analysis of liquid aerosols can benefit from the simultaneous sampling of both positively and negatively charged species from the same droplet. Variations may involve the analysis of a single droplet, repeated sampling of an individual droplet, or the use of pulsed electric fields to analyze specifically selected droplets. Ongoing investigations in our lab are exploring the parameter space related to FIDI, with the goal of quantifying the role of droplet size, charge carriers and their mobility, and bulk solvent characteristics such as dielectric constant and viscosity. The ultimate sensitivity of the method will depend on the development of an optimized interface for efficient ion transfer to the mass spectrometer.

6.3. Acknowledgements

The authors gratefully acknowledge Drs. Nathan Dalleska and Mona Shahgholi for the assistance with and use of their mass spectrometry facilities. The Beckman Institute at Caltech has provided facilities and financial support for these investigations. Studies of droplet evaporation and discharge processes associated with ESI have been supported by National Science Foundation grant CHE-9727566.

6.4. References

(1) Zeleny, J. *Phys. Rev.* **1917**, *10*, 1.

(2) Wilson, C. T. R.; Taylor, G. I. *Proc. Cambridge Philos. Soc.* **1925**, *22*, 728.

(3) Nolan, J. J. *Proc. R. Ir. Acad. Sect. A* **1926**, *37*, 28.

(4) Macky, W. A. *Proc. Roy. Soc. A* **1931**, *133*, 565.

(5) Taylor, G. *Proc. R. Soc. London, Ser. A* **1964**, *280*, 383.

(6) Taylor, G. *Proc. R. Soc. London, Ser. A* **1966**, *291*, 159.

(7) Miksis, M. J. *Phys. Fluids* **1981**, *24*, 1967.

(8) Basaran, O. A.; Scriven, L. E. *Phys. Fluids A* **1989**, *1*, 799.

(9) Basaran, O. A.; Patzek, T. W.; Benner, R. E.; Scriven, L. E. *Ind. Eng. Chem. Res.* **1995**, *34*, 3454.

(10) Stone, H. A.; Lister, J. R.; Brenner, M. P. *Proc. R. Soc. London, Ser. A* **1999**, *455*, 329.

(11) Zholkovskij, E. K.; Masliyah, J. H.; Czarnecki, J. *J. Fluid Mech.* **2002**, *472*, 1.

(12) Vizika, O.; Saville, D. A. *J. Fluid Mech.* **1992**, *239*, 1.

(13) Eow, J. S.; Ghadiri, M. *Chem. Eng. Process.* **2003**, *42*, 259.

(14) Duft, D.; Atchtzehn, T.; Muller, R.; Huber, B. A.; Leisner, T. *Nature* **2003**, *421*, 6919.

(15) Hager, D. B.; Dovichi, N. J. *Anal. Chem.* **1994**, *66*, 1593.

(16) Hager, D. B.; Dovichi, N. J.; Klassen, J.; Kebarle, P. *Anal. Chem.* **1994**, *66*, 3944.

(17) Gomez, A.; Tang, K. *Phys. Fluids* **1994**, *6*, 404.

(18) Chang, D.-Y.; Lee, C.-C.; Shiea, J. *Anal. Chem.* **2002**, *74*, 2465.

Chapter 7. Dynamics of field-induced droplet ionization. Time resolved studies of distortion, jetting, and progeny formation from charged and neutral methanol droplets exposed to strong electric fields

Adapted from Grimm, R.L. and Beauchamp, J.L. *J. Phys. Chem. B.* **2005**, *109*, 8244.

7.1. Abstract

We recently reported that strong electric fields may be employed to directly extract positive and negative ions for mass analysis, including intact proteins, from neutral droplets. The present study investigates the dynamics of this process using switched high electric fields to enable time-resolved studies of droplet distortion, Taylor cone formation, and charged progeny droplet extraction from neutral and charged 225 micron methanol droplets. After a specific time in the field, a flashlamp is triggered to record droplet distortions using shadow photography. At a critical field strength E_c^0 corresponding to the Taylor limit, neutral droplets exhibit a prolate elongation along the field axis forming symmetric cone-jets of positive and negatively charged progeny droplets, approximately 10 microns in diameter. This process is termed field-induced droplet ionization (FIDI). Because the timescale of FIDI is related to the frequency of shape oscillations that occur below the Taylor limit, models of field-dependent oscillation become an important predictor of the timescale for progeny jet formation. Droplets with a net charge q distort into asymmetric tear shapes and emit a single charged jet of progeny at a critical field E_c^q that is less than E_c^0. The measured decrease in droplet stream charge indicates that total charge loss can be greater than the original charge on the droplet, resulting in oppositely charged droplets. Interestingly, above E_c^0, charged droplets sequentially emit a jet of the same polarity as the net charge followed by a jet of reverse polarity emitted in the opposite direction. For both neutral and charged droplets, increasing the electric field decreases the time to form jets and the combination of net charge and higher-than-critical fields has a compound effect in accelerating progeny formation. The implications of our results for using switched fields in FIDI-mass spectrometry for on-demand ion sampling from neutral and charged droplets are discussed.

7.2. Introduction

Recent advances in understanding the effect of high electric fields on droplets have created new analytical methodologies for extracting and mass analyzing biomolecules from solution. In a sufficiently strong electric field, droplets elongate parallel to the field and develop two opposing Taylor cones that emit oppositely charged jets of small progeny droplets. When an analyte is dissolved in the droplets, the jets are a viable source of gas-phase analyte ions for mass spectrometry.[1] Termed field-induced droplet ionization (FIDI), the practical application of this experimental methodology will rely on detailed investigations of the dynamics of the process and a more complete understanding of the parameter space associated with the phenomenon. For example, given the specific size, composition, and charge of an individual droplet, mass spectrometric sampling by FIDI requires knowledge of the magnitude of the electric field required to produce jetting, the timescale of the event, and the efficiency with which analyte species are converted into the gas-phase ions and sampled by a mass spectrometer.

Droplet response to both electric fields and excess charge has been investigated for over a century. Although early motivations focused on the effect of electric fields on droplets within clouds,[2-4] more recent research has considered a broad range of applications from the technologically important processes of electrostatic spraying[5] to the revolution in mass spectrometric studies of biological molecules made possible by electrospray ionization.[6-11] Lord Rayleigh first considered the electrical pressure resulting from excess charge q on a droplet of spherical radius r and surface tension σ. He surmised that the natural quadrupolar oscillation of a droplet in a field-free environment becomes unstable when q exceeds the limit q_R, now known as the Rayleigh limit, defined in equation (7.1).

$$q_\mathrm{R} = 8\pi\left(\sigma\varepsilon_0 r^3\right)^{1/2} \tag{7.1}$$

Equation (7.1) and all later equations are reported in MKS units and ε_0 is the permittivity of free space. Non-dimensional electric fields used in the literature[12,13] are dimensionalized as appropriate by the characteristic field strength $(2\sigma/\varepsilon_0 r)^{1/2}$ and non-dimensional frequencies are divided by the characteristic time $(\rho r^3/\sigma)^{1/2}$ where ρ is the droplet density. At $q \geq q_\mathrm{R}$, a limit reached when a charged droplet evaporates to a sufficiently small size, Rayleigh postulated that the droplet would throw out liquid in fine jets[14] in an event alternatively referred to as Rayleigh discharge[10,11] or Coulomb fission.[9] The Rayleigh limit has been researched extensively and is widely used to explain the behavior of highly charged droplets formed by electrospray ionization.[9,15,16]

The FIDI process results from the distortion and jetting of droplets subjected to a high electric field. Early experimental[3,4,17,18] and theoretical[19,20] work showed that neutral droplets symmetrically elongate parallel to the electric field as polarization-induced charge densities develop at opposite ends of the prolate spheroid. This shape becomes unstable when the applied electric field reaches a critical limit, ${E_\mathrm{c}}^0$, given by (7.2). This

$${E_\mathrm{c}}^0 = \frac{c}{(8\pi)^{1/2}}\left(\frac{2\sigma}{\varepsilon_0 r}\right)^{1/2} \tag{7.2}$$

critical field is known as the Taylor limit named for G. I. Taylor who pioneered the corresponding theory. In equation (7.2), the fitting constant c has been determined both empirically[3,4,18,21] and theoretically,[20] and the accepted value is 1.625 for liquid droplets in air.[20] Assuming droplets always distort into spheroidal shapes, Taylor additionally derived (7.3) and (7.4), the general relationship between an applied electric field $E < {E_\mathrm{c}}^0$

$$E = I_2\gamma^{-4/3}\left(2-\gamma^{-3}-\gamma^{-1}\right)^{1/2}\left(\frac{2\sigma}{\varepsilon_0 r}\right)^{1/2} \tag{7.3}$$

and the resulting aspect ratio $\gamma = a / b$ of the major to minor axis of the spheroid.[20] In equation (7.3), the coefficient I_2 is a higher-order function of γ represented by (7.4).

$$I_2 = \frac{1}{2\left(1-\gamma^{-2}\right)^{3/2}}\ln\left[\frac{1+\left(1-\gamma^{-2}\right)^{1/2}}{1-\left(1-\gamma^{-2}\right)^{1/2}}\right]-\frac{1}{1-\gamma^{-2}} \tag{7.4}$$

Although a simple relation does not exist for $\gamma(E)$ in the spheroidal approximation, equation (7.5) approximates the relationship between γ and E in (7.3) to within 1% for

$$\gamma(E) = \left(1+\frac{9r\varepsilon_0 E^2}{16\sigma}\right)\left(1-\frac{9r\varepsilon_0 E^2}{16\sigma}\right)^{-1} \tag{7.5}$$

fields less than 55% of the Taylor limit.[22] Equation (7.3) predicts γ increases with increasing E until $\gamma = 1.85$ where the droplet becomes unstable corresponding to $E = E_c^0$. This relationship is supported by experimental and theoretical evidence for neutral droplets and soap films in air.[3,12]

Between the Rayleigh limit of charge and the Taylor limit of field exists the general case where excess electrical pressure within a droplet results from both net charge and the externally applied electric field. Taylor's spheroidal approximation is not as accurate at predicting shapes and critical fields because charged droplets are shown to be egg- or tear-shaped,[12,23,24] having a higher curvature on the side carrying the net charge. For a droplet of charge q, this shape becomes unstable at a critical electric field, E_c^q, and is characterized by the formation of a single jet from the sharper end. The critical field is a function of net charge as increasing charge reduces the field necessary to create an instability, or $0 \leq E_c^q \leq E_c^0$ for $0 \leq q \leq q_R$. Recent investigations of jetting, fissioning, and Taylor cones focus on droplets suspended in an ambient liquid.[25-27] This work bears little application to FIDI, which is performed in an ambient gas so that the progeny jets may be directed towards the inlet of an atmospheric-sampling mass spectrometer.

In the present investigation, we characterize the temporal evolution of droplet shapes leading to FIDI events as a function of electric field strength and droplet net charge following exposure of the droplet to a rapidly switched electric field. A vibrating orifice aerosol generator (VOAG)[28] generates a monodisperse stream of 225 μm methanol droplets whose Taylor limit from (7.2) is 2.16×10^6 V/m, somewhat close to the breakdown limit of air.

This work partitions the study of droplets into three specific cases. The first case considers the time-dependent shape oscillations of neutral droplets at fields below $E_c^{\,0}$. The oscillation frequency is field-dependent and is a useful predictor for the timescale for FIDI as E approaches $E_c^{\,0}$. Fitted experimental $\gamma(t)$ values are compared to literature models discussed in the experimental section.

The second case considers neutral droplets in fields at and above $E_c^{\,0}$. FIDI events are characterized by the highly elliptical shape and presence of jetting from conical tips as a function of time in and strength of the applied electric field. Field strengths required for FIDI are compared to eq (7.2) and the timescale for jetting to occur is related to droplet oscillation frequencies from the first case.

The third case investigates droplets between 4% and 13% of their Rayleigh limit of charge in fields at and above their critical field, $E_c^{\,q}$. The decrease in $E_c^{\,q}$ as a function of q is explored and related to models developed by Basaran and Scriven[12] and by Abbas and Latham.[24]

7.3. Experimental section

7.3.1. Droplet production and charging

Figure 7.1 shows a schematic of the experimental apparatus. A vibrating orifice aerosol generator (VOAG) creates a monodisperse droplet stream. HPLC-grade methanol (EMD Chemicals Inc.) is used without further purification. A nitrogen-backed solution reservoir (not shown) delivers methanol to the VOAG. Nitrogen gas (1 - 3 psig) pumps the methanol giving a smoother flow rate and a more stable stream than a syringe pump. A 130 μm I.D. ceramic orifice (4P480-0016-343; Kulicke and Soffa Inc., Willow

Grove, PA, USA) is mounted within an annular piezoelectric actuator vibrating in the direction of the methanol flow at 11.4 kHz. The ~5 m s^{-1} stream breaks into droplets that pass through a grounded aperture.

Droplet charge is governed by the local electric field at the point at which the stream breaks into droplets. Before the orifice, the methanol passes through a metal charging ring connected to a voltage supply, V_C, establishing a field between the stream and the grounded aperture. Setting V_C to ground generates neutral droplets while increasing V_C between 0 and 600 V linearly increases the net charge between 0% and 13% of the Rayleigh limit. Higher net charge results in excessive space-charge repulsion between the droplets causing a disruption of the stream. A digital picoammeter (model 485, Keithley Instruments, Inc.) measures the total current to ground resulting from the droplets impacting a metal collector. Individual droplet charge is calculated from this current and the droplet production rate. A step-function drop in the picoammeter current indicates the amount of charge droplets lose during FIDI by comparing the current from droplets both before and after FIDI events. Droplet charging is not affected by other electric fields in the experiment.

7.3.2. Pulsed field experiment

The droplets pass between two 6.5 mm long parallel-plate electrodes spaced 1.4 mm apart that define the FIDI region. Calculations in SIMION[29] verify the field gradient approximates a parallel-plate capacitor to within 4% over 88% of its length when the droplet path bisects the electrodes. In our earlier experiments, this field was

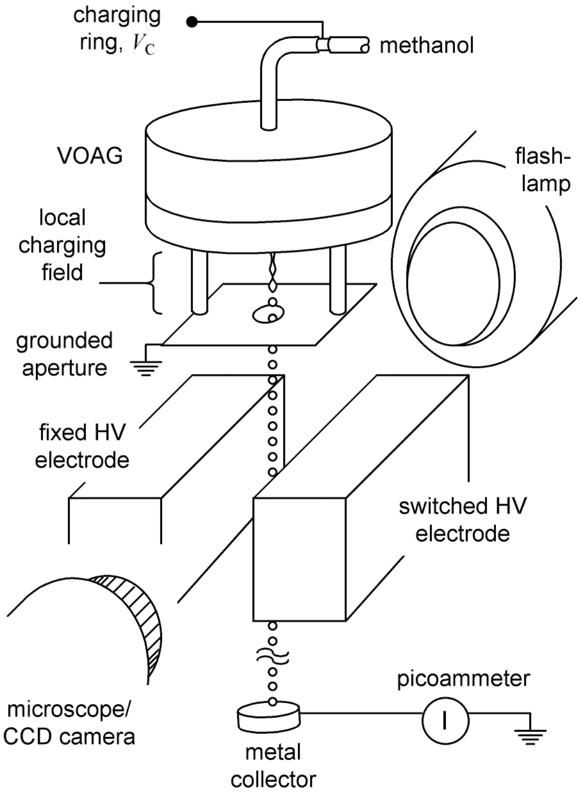

Figure 7.1. Schematic diagram of the experiment. Methanol is delivered to a vibrating orifice aerosol generator (VOAG) that breaks a liquid stream into monodisperse 225 μm droplets at 11.4 kHz. A voltage applied to the stream by a charging ring held at V_C relative to the grounded aperture determines droplet net charge. Droplets pass between the parallel electrodes that define the high-field region. The left electrode is held at a fixed high voltage (HV) while the opposing electrode is switched from HV to ground. After exposure to the high field for a time *t*, a flashlamp behind the stream illuminates the droplets and a microscope fitted with a CCD camera records the resulting shadowgraph. A metal collector intercepts the droplet stream and a picoammeter quantifies droplet charge.

fixed by holding one electrode at high voltage (HV) and the other at ground, resulting in a gradual increase in the field experienced by droplets as they entered the high-field region.[1] In the present experiment, droplets enter this region when both electrodes are held at an identical high voltage between 2.8 and 3.4 kV creating a field-free region. The left electrode maintains a fixed HV while a stacked circuit of MTP1N100E MOSFETs switches the right-hand plate from HV to ground and remains there for a variable time $t = 10 - 900$ μs before returning to high-voltage. As a result, droplets are in a well-defined electric field until they are photographed. Based on similar circuits from the literature,[30,31] this in-house design is capable of switching up to 4 kV to ground in less than 1 μs. Rather than using an avalanche transistor[30] or a transmission line[31] to drive the FETs, a 6N135 optoisolator drives each FET and isolates the remainder of the electronics from a possible surge or breakdown.

After the variable time, t, following exposure to the high field, a sub-microsecond xenon flashlamp illuminates the droplets. The flashlamp is mounted behind the FIDI region and directs a collimated beam directly at a microscope focused on the droplets. Using a 10x objective, a 10x wide-angle eyepiece adapter (MaxView Plus, Scopetronix, Cape Coral, FL, USA) and an afocally-coupled CCD camera (C-5060 wide zoom, Olympus), the optical train resolves 5 μm features. Acquiring images of droplets and progeny for t ranging from 10 to 900 μs generates a time-history of droplet response to a specific high electric field.

7.3.3. Determining the aspect ratio and model comparison

Each shadowgraph contains 3-5 droplets. For each droplet image, a custom LabView-based edge analysis program developed by the Leisner research group[32] fits an ellipsoid that provides aspect ratio and size information. The program verifies the monodispersity of the droplets and computes aspect ratios of 10-20 droplets for each t and electric field strength. The time-dependent aspect ratio, $\gamma(t)$ is fitted to a damped sine function (7.6). In eq (7.6), ν is the fitted oscillation frequency in s^{-1}, A is the amplitude, ϕ is the phase, γ_∞ is the equilibrium aspect ratio or $\gamma(t = \infty)$, and g is the exponential dampening constant. Oscillation frequencies are compared to numerical solutions by Basaran and co-workers[13] and to analytical solutions by Feng and Beard[33] and by Brazier-Smith and co-workers.[34] Feng and Beard found the field-dependent oscillation frequency ν^{FB} to be eq (7.7). They suggest the frequency decreases proportionally with E^2 until reaching $E_{\mathrm{c}}^{\;0}$ where the frequency is given by eq (7.8). Brazier-Smith and co-workers derived the oscillation, ν^{BS}, as a function of the equilibrium aspect ratio, (7.9).

$$\gamma(t) = \gamma_\infty + A\sin(2\pi\nu t + \phi)\exp(-gt) \tag{7.6}$$

$$\nu^{\mathrm{FB}} = \frac{8^{1/2}}{2\pi}\left[1 - 2.764E^2\left(\frac{\varepsilon_0 r}{2\sigma}\right)\right]\left(\frac{\sigma}{r^3\rho}\right)^{1/2} \tag{7.7}$$

$$\nu^{\mathrm{FB}}(E_{\mathrm{c}}^{\;0}) = \frac{8^{1/2}}{2\pi}\left[1 - 2.764\frac{1.625^2}{8\pi}\right]\left(\frac{\sigma}{r^3\rho}\right)^{1/2} \tag{7.8}$$

$$\nu^{\mathrm{BS}} = \frac{8^{1/2}}{2\pi}x^{1/2}\left(\frac{\sigma}{r^3\rho}\right)^{1/2} \tag{7.9}$$

In eq (7.9), x is a multi-component function of γ. Combining the relationships between γ and ν^{BS} in eq (7.9) and γ and E in eq (7.3), Brazier-Smith and co-workers predict ν^{BS} decreases to 0 as E approaches E_{c}^{0}.[34] Equations (7.7) and (7.9) reduce to the natural $l = 2$ mode shape oscillation at $E = 0$.

The LabView program determines the aspect ratio assuming a spheroidal shape, which limits rigorous analysis to neutral droplets. Since charged droplets in electric fields are tear-shaped, analysis of the aspect ratio is limited to qualitative comparisons. While this study explores neutral droplets below E_{c}^{0}, we do not consider charged droplets below E_{c}^{q}.

7.4. Results and discussion

7.4.1. Case One. Neutral droplets below the critical field

Droplets in fields below E_{c}^{0} undergo damped oscillation. Figure 7.2 highlights a sequence of droplets in a 2.00×10^{6} V/m electric field. Initially, $\gamma(0\ \mu\mathrm{s}) = 1$ corresponding to the spherical droplet (A). A damped shape oscillation is marked by increasing aspect ratios in (B)-(E), decreasing aspect ratios in (E)-(I), and increasing again in (J). Figure 7.3 highlights this trend in plots of γ versus the time in the electric field for four field strengths below E_{c}^{0}. Each point represents the average aspect ratio for approximately ten images at each respective time, and is fit to the exponentially damped sine function (7.6). The fitted equilibrium aspect ratios, γ_{∞}, strictly increase as the electric field increases and are in excellent agreement with Taylor's theoretical model, (7.3), for each respective electric field.

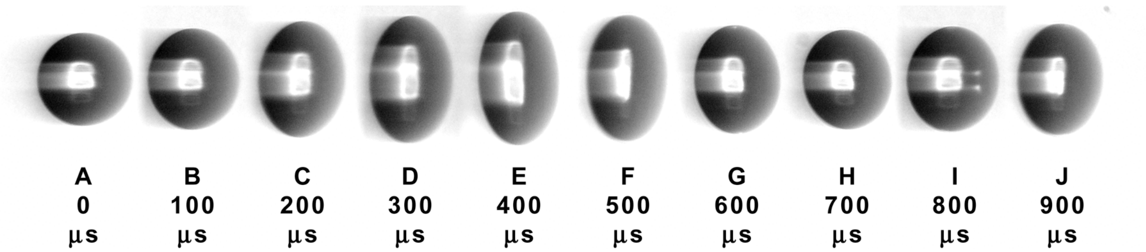

Figure 7.2. Neutral 225 µm diameter methanol droplets are exposed to a 2.00×10^6 V/m electric field for the indicated time period. Initially, droplets are spherical (A). Through 400 µs, droplets distort into prolate ellipsoids with increasing aspect ratios. Between 400 (E) and 800 µs (I), the aspect ratios decrease, only to increase again beginning at 900 µs (J). This shape oscillation is characteristic of neutral droplets in fields below their Taylor limit.

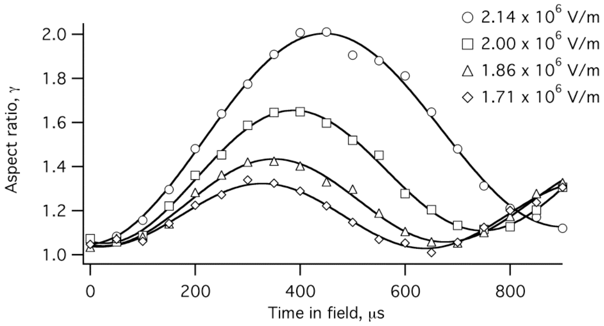

Figure 7.3. Average aspect ratio, γ, versus time for 225 µm diameter methanol droplets in fields below E_c^0 where the spheroid shape oscillates until reaching equilibrium. This shape is characterized by γ, the ratio of the major to minor axis of the spheroid. As the applied electric field increases, the amplitude of the oscillation increases and the frequency decreases in qualitative agreement with theoretical models.

Figure 7.4 compares the fitted oscillation frequencies from this work (round markers) with the Feng and Beard frequency ν^{FB} (solid line), the Brazier-Smith and co-workers frequency ν^{BS} (dashed line), and the numerical simulations of Basaran and co-workers (triangle markers, dotted line) which are each dimensionalized for 225 micron methanol droplets. Error bars represent how the uncertainty in the aspect ratio data is reflected in the oscillation frequency. For each electric field strength, uncertainty in the frequency is bounded by fitting the damped sine function to plots of the average aspect ratio minus the standard deviation and plus the standard deviation. The maximum error in the fitted frequency values is 7%. The fitted values from this work follow each of the theoretical trends with decreasing frequencies as the applied field increases. The initial values closely match ν^{FB} but diverge to lower frequencies at higher field strengths.

7.4.2. Case Two. Neutral droplets above the critical field

Figure 7.5 shows 225 μm diameter droplets symmetrically elongating and jetting at two field strengths. Droplets oscillate at 2.14×10^6 V/m as shown by Figure 7.3 and undergo FIDI in a 2.18×10^6 V/m field, in good agreement with the value of E_{c}^{0} predicted by (7.2). In a 2.18×10^6 V/m field, jetting begins after 650 μs (Figure 7.5E), whereas jetting occurs as early as 350 μs in a 2.46×10^6 V/m field (Figure 7.5J). Thus, the 13% increase in the electric field above E_{c}^{0} accelerates the elongation and reduces the time to form jets by 46%. Figure 7.6 graphs $\gamma(t)$ for fields between 2.18 and 2.42 x 10^6 V/m as well as the fitted oscillation $\gamma(t)$ at 2.14×10^6 V/m reproduced from Figure 7.4. Figure 7.6 illustrates this reduction in time to achieve jetting which results

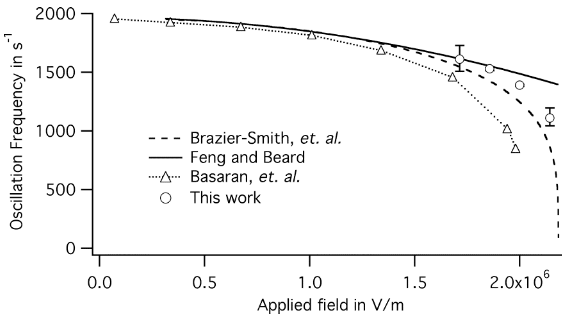

Figure 7.4. Comparison of fitted oscillation frequencies to predictions of Brazier-Smith and co-workers (dashed line), of Feng and Beard (solid line), and of Basaran and co-workers (triangle markers, dotted line) applied to 225 μm methanol droplets. Error bars represent the frequency of damped sine fits to the average aspect ratio values plus and minus the respective standard deviations, respectively. Fitted values from this work (round markers) follow the theoretical trends in all models, most closely matching the predictions of Brazier-Smith and co-workers.

from increasing the applied field. For droplets at E_c^0, conical shapes begin to form at aspect ratios between 2.5 and 3 following exposure to the high field. At the onset of jetting, the aspect ratio is approximately 3.2. This is consistent over the range of electric fields employed indicating that only the time to reach jetting is affected by field strength, and the shape at the onset remains consistent.

Figure 7.6 highlights a fundamental relationship between the droplet oscillation in fields below E_c^0, and the elongation leading to FIDI in the critical field. Through 450 μs, or half the oscillation period, the oscillation closely tracks the aspect ratio of droplets undergoing FIDI at E_c^0. Beyond 450 μs, the aspect ratio of oscillating droplets decreases while the aspect ratio of droplets undergoing FIDI continues to increase. This pattern corroborates the non-dimensional calculations of Basaran and coworkers.[13] Therefore the response of a droplet in fields slightly below and at E_c^0 are proportionally linked and the shape oscillation of a droplet near the critical field becomes an important predictor for the timescales for progeny jet formation at E_c^0. Equation (7.10) empirically relates both the 650 μs time to initiate FIDI, τ_{FIDI}, to the 900 μs oscillation period, ν^{-1}, for 225 μm droplets and τ_{FIDI} = 575 μs to ν^{-1} = 800 μs for similar investigations on 200 μm droplets.

$$\tau_{\mathrm{FIDI}} \approx 0.75\left(\nu_{E \to E_c^0}\right)^{-1} \tag{7.10}$$

Equation (7.10) is comparable to non-dimensional calculations that show a ratio of ~0.6 between the timescale for a droplet to elongate to $\gamma = 3.2$ in fields above E_c^0 to the oscillation period slightly below E_c^0.[13]

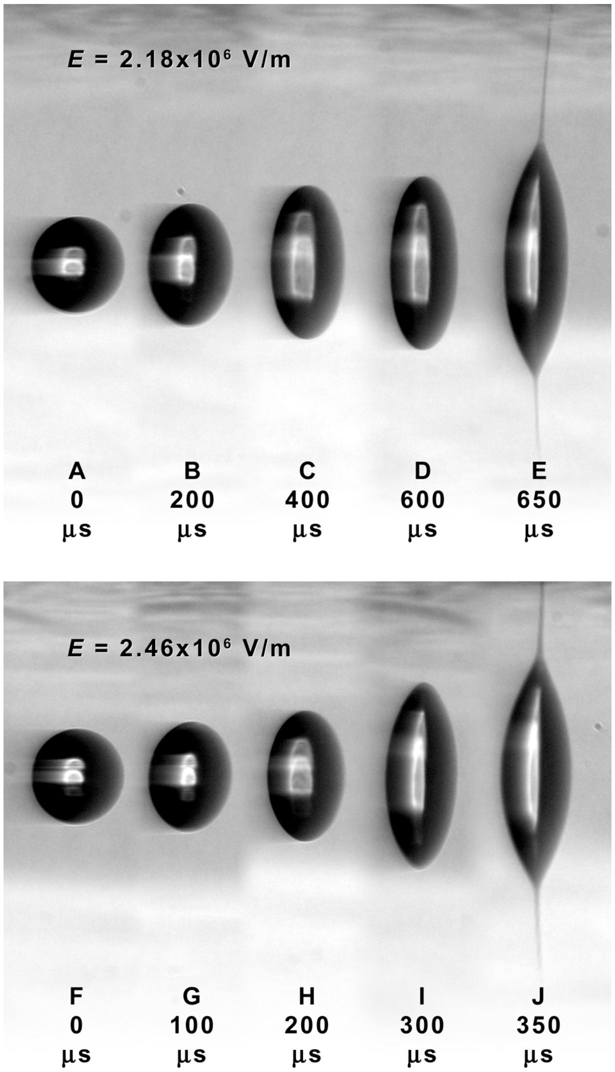

Figure 7.5. Sequences of 225 μm droplets exposed to an electric field for the indicated time period. Frames (A)-(E) represent droplets in a 2.18×10^6 V/m field while frames (F)-(J) demonstrate FIDI in a 2.46×10^6 V/m field. Each sequence is characterized by symmetrical elongation as exposure to the field increases, culminating in the formation of two conical tips and oppositely charged progeny jets characteristic of FIDI. At 2.18×10^6 V/m, FIDI develops after 650 μs in (E) while the stronger field results in accelerated elongation and progeny formation after 350 μs in (J).

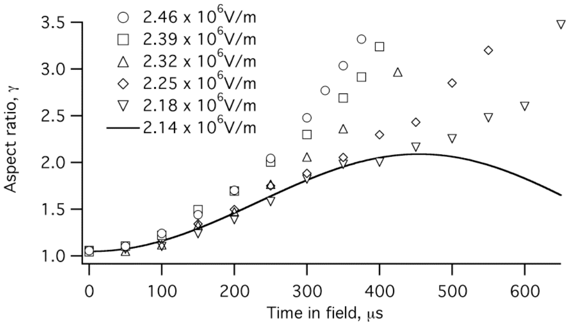

Figure 7.6. Average aspect ratio, γ, versus time for 225 μm diameter methanol droplets in fields sufficiently high for FIDI. The oscillation fit from droplets in a 2.14 x 10^6 V/m field is included for comparison. Because the droplets oscillate at 2.14 x 10^6 V/m and undergo FIDI at 2.18 x 10^6 V/m, the latter is taken as E_c^0. The shape of droplets undergoing FIDI at E_c^0 (▽) resembles the shape of oscillating droplets through half a period as is noted by the similar values of $\gamma(t)$ through 450 μs. This shows that oscillation frequencies may be employed to predict FIDI timescales. Above E_c^0 the elongation is accelerated, resulting in a decrease in the time needed to reach jetting and progeny formation.

Figure 7.6 also provides insight regarding the fitted oscillation frequency values shown in Figure 7.4. Although the fitted oscillation frequency values most closely match the trend of Brazier-Smith and coworkers, ν^{BS}, that theory predicts the shape oscillation decreases to zero as the applied field reaches E_{c}^{0}. The similarity between the oscillating droplet and the aspect ratio of droplets undergoing FIDI at E_{c}^{0} in Figure 7.6 demonstrates that sub-critical oscillations decrease to a finite, non-zero value. The analytical model of Feng and Beard and the numerical model of Basaran and co-workers provide the closest theoretical match with our measured oscillation frequencies. In using equation (7.10) to predict the FIDI behavior of a droplet of known physical parameters, equation (7.8) currently provides the best approximation of the timescale for progeny drop formation at E_{c}^{0}.

7.4.3. Case Three. Charged droplets above the critical field

Figure 7.7 and Figure 7.8 show asymmetrical stretching and jetting from charged 225 μm methanol droplets. Figure 7.7A-E shows droplets carrying a charge 0.04 q_{R} in a 2.16 x 10^{6} V/m field and 0.09 q_{R} droplets in a 2.14 x 10^{6} V/m field in frames (F)-(J). In both cases, droplets are exposed to the minimum field required for jetting, E_{c}^{q}, for each respective q. Similarly, Figure 7.8A-H displays a sequence of 0.13 q_{R} droplets at their critical field of 2.09 x 10^{6} V/m. The non-linear trend in decreasing critical fields agrees with finite-element calculations[12] and disagrees with the linear dependence on charge determined by Abbas and Latham.[24] Similarly, the time to initiate jetting decreases as

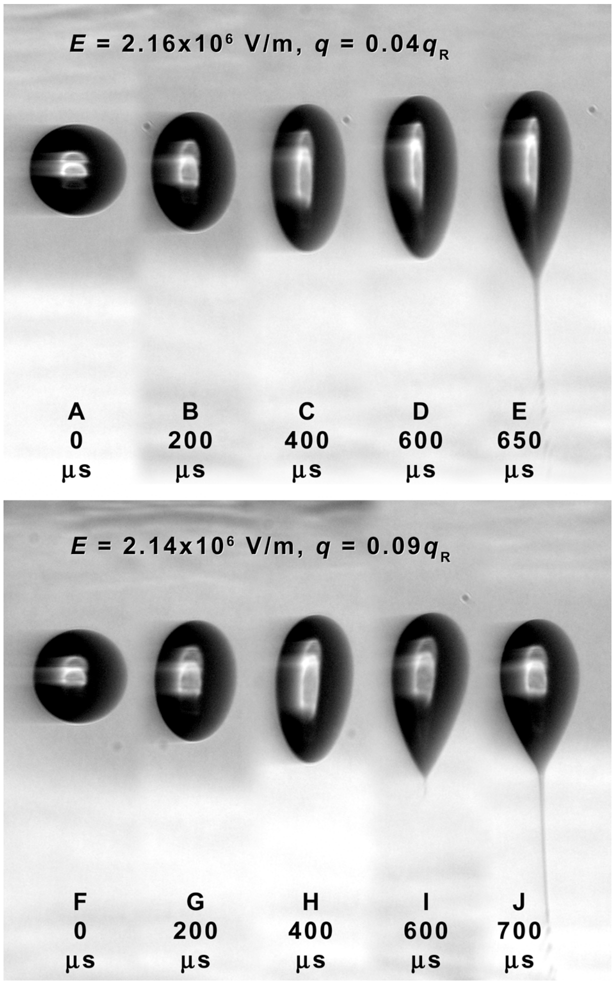

Figure 7.7. Sequences of 225 μm methanol droplets with $q = 0.04\ q_{\mathrm{R}}$ droplets undergoing asymmetrical distortions at $E = 2.16 \times 10^6$ V/m and $q = 0.09\ q_{\mathrm{R}}$ droplets at $E = 2.14 \times 10^6$ V/m. In both cases, these fields represent the minimum for which FIDI is observed, E_{c}^{q}. For 0.04 q_{R}, the 650 μs time to begin jetting (E) is identical to the corresponding neutral droplet at E_{c}^{0} (Figure 5E) while 0.09 q_{R} droplets exhibit a nascent jet at 600 μs (I). The jets in (E) and (J) demonstrate capillary instability and the formation of ~10 μm progeny droplets.

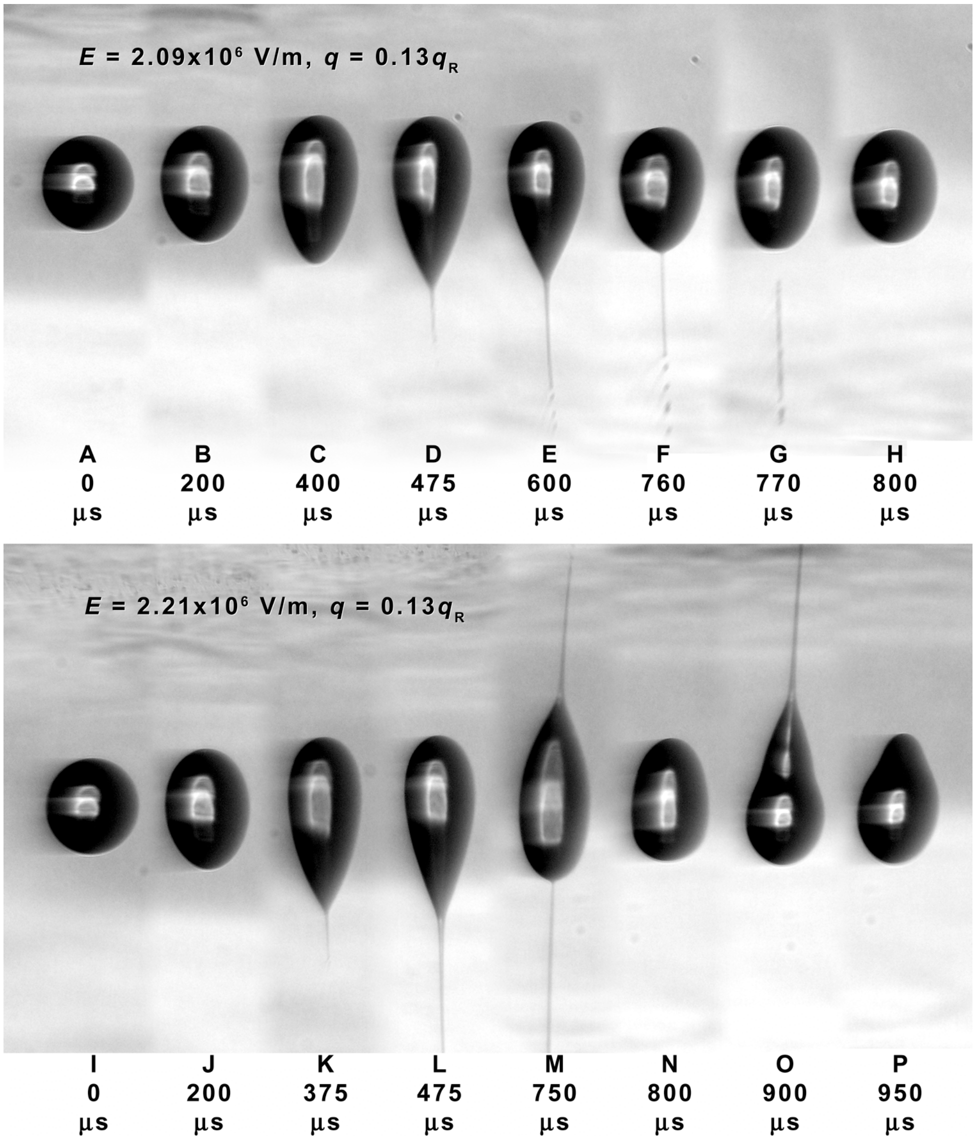

Figure 7.8. Sequences of 225 μm methanol droplets with $q = 0.13\ q_R$ in a 2.09 x 10^6 (A)-(H) and a 2.21 x 10^6 V/m field (I)-(P). For these droplets E_c^q = 2.09 x 10^6 V/m. Extended observation at E_c^q demonstrates the entire FIDI process from distortions (A)-(C), jetting (D)-(G), and back to a spheroidal shape (H). Drops (E) through (G) distinctly show the formation of fine progeny. As the jetting concludes in (F)-(G), both the aspect ratio and the size of the Taylor cone decrease. The 2.21 x 10^6 V/m field in (I)-(J) is greater than E_c^0 for neutral droplets and results in sequential jetting of a positive jet from 375 μs (K) through 750 μs (M) where a short-lived negative jet appears. Following initial jetting, droplets develop non-conical distortions and emit an additional short-lived negative jet at 900 μs (O). The non-conical shape and second negative jet are attributed to higher-order vibrations caused by the initial asymmetric flow within the droplet.

net charge increases. At 0.04 q_R, jet formation occurs at 650 μs as shown in Figure 7.7E which is the same timescale observed for neutral droplets at E_c^0 (Figure 7.5E). As the charge increases, the timescale decreases to 600 μs at 0.09 q_R (Figure 7.7I) and 475 μs at 13% q_R (Figure 7.8D).

Figure 7.8 includes photographs illustrating the behavior of droplets beyond the initial jetting process. Figure 7.8D shows a sharp Taylor cone emitting a progeny jet at 475 μs. The initial stages of jetting correspond to the sharpest cones. By 760 μs (Figure 7.8F), the cone has receded as the jet is emitted from a roughly spheroidal droplet. In frame (G), ten microseconds later, the progeny jet has separated from the completely spheroidal parent. In this case, the duration of the FIDI event is approximately 285 μs.

At higher fields, charged droplets exhibit sequential jetting. Figure 7.8I-P illustrates the response of 0.13 q_R charged droplets to a 2.21 x 10^6 V/m electric field that is 6% higher than E_c^q and 2% greater than E_c^0 for neutral droplets of the same size. Droplets distort asymmetrically and emit a *positive* jet from 375 μs (Figure 7.8K) through 750 μs (M). Unique to this case, droplets develop a second conical tip that emits a short-lived *negative* progeny jet at 750 μs (M). After this sequential jetting, droplets relax into a spade-shaped configuration (frame N) before emitting an additional short-lived negative jet at 900 μs (frame O) from a non-conical tip. We attribute the spade and non-conical shapes of the second negative jet in Figure 7.8N-P to higher-order, $l > 2$, mode vibrations within the droplet where $l = 2$ is the fundamental mode.[35,36] Higher-order vibrations are most likely to due to asymmetric flow within the droplet during the initial asymmetric elongation in frames (A)-(D) and the corresponding relaxation in (F)-(H).

7.4.4. Progeny droplet and parent charge loss

Figure 7.7 and Figure 7.8 show progeny droplets separating from the charged droplet jet. Progeny droplets appear at the end of jets from both charged and neutral parents and form due to capillary instability and breakup of the jet. These progeny droplets are approximately 10 μm across or roughly 5% of the diameter of the 225 μm parent droplets. The present experiment is unable to quantify a decrease in size of the parent droplet after a FIDI event such as the sequence in Figure 7.8A-H, and therefore observations of mass loss are below the measurement limits of the optical train. If the upper limit of mass loss were bounded at 5%, then 600 progeny droplets, each 10 μm in diameter, would result. The lower bound is the volume within a cylindrical jet at any instant. Jets extend 600 μm to the electrodes, and a 10 μm diameter cylinder of liquid methanol would form ninety 10 μm progeny droplets.

Measurements of the current associated with the droplets stream provide information relating to the droplet charge. Droplets carrying a +0.03 q_R net charge produce a 4.5 nA current with $E = 0$. When the electric field is applied, the timing cycle relative to the droplet flow is such that only 5% of the droplets produced undergo FIDI at a sufficiently high field strength. The remainder of the droplets pass between the electrodes when they are both at high voltage and there is no field between them. The droplets undergoing FIDI lead to a decrease in the picoammeter current of 1.0 nA, indicating that an individual droplet experiences a 1.8 pC loss or 0.13 q_R per FIDI event. Because the droplets initially carried a +0.03 q_R charge, the FIDI event leaves the droplets *oppositely* charged -0.10 q_R. This observation is consistent with the data in Figure 7.8I-P where following the initial jetting process, the droplets emit jets in the opposite direction.

7.4.5. Droplet images in the literature

The images of symmetrical neutral droplet jetting in Figure 7.5 and asymmetrical charged droplet jetting in Figure 7.7 and Figure 7.8 can be related to previous photographs of droplet instabilities and jetting. Hager and co-workers imaged jetting from charged methanol droplets in the high electric field used to generate a corona discharge.[37,38] Droplets distorted asymmetrically and emitted a single jet of progeny directed away from the corona needle along the field lines. Reported figures were overlays of 3000 individual photographs indicating a highly reproducible jetting phenomenon. Gomez and Tang captured heptane droplets undergoing asymmetrical jetting in an electrospray plume.[39] The images of heptane droplets are single events not consistently oriented with the electric field within the electrospray plume. They attribute this to aerodynamic effects. In both the Hager and co-workers and the Gomez and Tang experiments, the droplets carried a net charge before jetting as a result of being ionized by the corona discharge or the electrospray process, respectively. Similarly, both were observed in high fields, specifically a corona discharge and an electrospray plume. While both sets of images are inferred to be the result of Rayleigh discharge events,[8] the asymmetrical nature contrasts with the symmetrical event observed by Duft and co-workers for charged ethylene glycol droplets suspended in an electrodynamic balance (EDB).[16] The droplets studied by Hager and co-workers droplets most likely exhibit jetting induced by an electric field, corresponding to Case 3, rather than a pure Rayleigh discharge process. The situation is less clear with the Gomez and Tang experiments. In the dense electrospray plume, the electric fields of nearby charged droplets may also affect the jetting process when droplets approach the Rayleigh limit.

7.4.6. Implications for FIDI-mass spectrometry

The neutral and charged droplet studies in Cases 2 and 3 suggest new methods of sampling in FIDI-MS. The minimum field necessary for neutral droplet FIDI is given by (7.2) and the timescale of the event is predicted by (7.10). Charged droplets develop instabilities and undergo FIDI sooner than their neutral counterparts, and increasing the applied electric field above the critical value also decreases the timescale. For example, the time needed to induce jetting and charged progeny formation from 225 μm methanol droplets is reduced by almost half when the field is raised from E_c^0 to 6% higher than E_c^q and the charge is increased from 0 to 0.13 q_R (Figure 7.8). This may be applied to analyze the composition of a specific droplet out of a larger collection selectively charged in a manner similar to flow cytometry experiments, or a single charged droplet held in an EDB. Takeda and co-workers recently demonstrated that electric fields lift water droplets off of a superhydrophobic surface in a process that imparts a net charge to the droplet.[40] These droplets can subsequently be directed into a high-field region for FIDI-MS analysis. This technique may be applied to sample the composition of droplets from a microfluidic device or an LC column.

7.5. Conclusions

A droplet stability diagram in Figure 7.9 summarizes the behavior of droplets as a function of charge and applied electric field. Neutral droplets (Figure 7.9A) experience prolate shape oscillations in fields below a critical strength, $E_c^{\,0}$. Above $E_c^{\,0}$ (Figure 7.9B), droplets form symmetric cone-jets of positive and negative progeny at a rate that may be predicted from the frequency of the sub-critical shape oscillations. Thus theoretical models of shape oscillations are important for studying new systems, as the timescale for the onset of jetting at $E_c^{\,0}$ is approximately 75% the oscillation period slightly below $E_c^{\,0}$.

The critical limit for charged droplets, $E_c^{\,q}$, decreases as charge is increased. This non-linear limit is represented by the solid curve in Figure 7.9 and qualitatively follows the shape predicted both by numerical analysis and Taylor's spheroidal approximation.[12] Below $E_c^{\,q}$, tear-shaped oscillations are found in charged droplets (Figure 7.9C) while above $E_c^{\,q}$ droplets emit a single charged jet of progeny droplets (Figure 7.9D). At fields above $E_c^{\,0}$ a new behavior is observed in which charged droplets sequentially emit a jet of the same polarity as the net charge followed by a jet of reverse polarity from the opposing side (Figure 7.9E). The critical limit for sequential jetting is noted by the dashed curve whose specific shape remains unexplored over a wide range of q-E space.

Increasing the electric field decreases the time to form jets from both neutral and charged droplets, and the combination of net charge and higher-than-critical electric fields has a compound effect in accelerating progeny formation. Therefore the period of neutral droplet shape oscillations represents a maximum timescale for the onset of FIDI. Understanding the FIDI characteristics for a droplet of given size and charge in a specific applied field, one may apply rapidly switched fields to directly mass analyze the components of a specific droplet or a single droplet held in an electrodynamic balance.

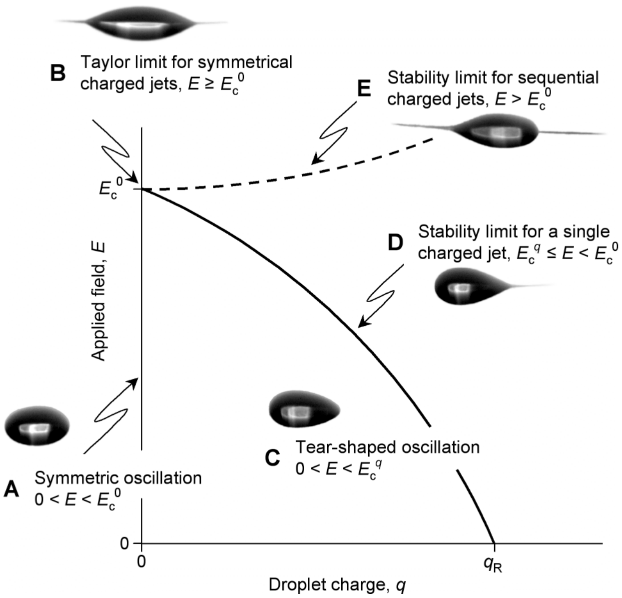

Figure 7.9. Summary of droplet stability as a function of net charge and applied electric field. Uncharged droplets below the critical field E_c^0 (A) undergo symmetric shape oscillations. Above E_c^0, uncharged droplets in fields above E_c^0 symmetrically elongate and simultaneously emit positive and negative progeny jets (B). The critical field for progeny formation from charged droplets decreases with increasing charge, represented by E_c^q (solid curve). Below E_c^q, charged droplets oscillate with asymmetric, tear shapes (C). Above E_c^q, droplets emit a single jet of charged progeny (D). At fields greater than E_c^0, a second critical field exists above which charged droplets emit sequential jets (E). The curve of this stability limit is unknown and represented with a dashed line.

7.6. Acknowledgements

The authors thank Dr. Richard Flagan for his discussions and Dr. Thomas Leisner for the LabView-based droplet analysis software. This material is based on work supported by the National Science Foundation under grant No. CHE-0416381 and a grant from the Beckman Institute at Caltech.

7.7. References

(1) Grimm, R. L.; Beauchamp, J. L. *J. Phys. Chem. B* **2003**, *107*, 14161.

(2) Wilson, C. T. R. *Phil. Trans. A* **1921**, *221*, 104.

(3) Wilson, C. T. R.; Taylor, G. I. *Proc. Cambridge Philos. Soc.* **1925**, *22*, 728.

(4) Nolan, J. J. *Proc. R. Ir. Acad. Sect. A* **1926**, *37*, 28.

(5) Bailey, A. G. *Electrostatic spraying of liquids*; Wiley: New York, 1988.

(6) Fenn, J. B.; Mann, M.; Meng, C. K.; Wong, S. F.; Whitehouse, C. M. *Science* **1989**, *246*, 64.

(7) Yamashita, M.; Fenn, J. B. *J. Phys. Chem.* **1984**, *88*, 4451.

(8) *Electrospray Ionization Mass Spectrometry*; Cole, R. B., Ed.; John Wiley and Sons: New York, 1997.

(9) Kebarle, P. *J. Mass Spectrom.* **2000**, *35*, 804.

(10) Grimm, R. L.; Beauchamp, J. L. *Anal. Chem.* **2002**, *74*, 6291.

(11) Smith, J. N.; Flagan, R. C.; Beauchamp, J. L. *J. Phys. Chem. A* **2002**, *106*, 9957.

(12) Basaran, O. A.; Scriven, L. E. *Phys. Fluids A* **1989**, *1*, 799.

(13) Basaran, O. A.; Patzek, T. W.; Benner, R. E.; Scriven, L. E. *Ind. Eng. Chem. Res.* **1995**, *34*, 3454.

(14) Rayleigh, L. *Philos. Mag.* **1882**, *14*, 184.

(15) Davis, E. J.; Bridges, M. A. *J. Aerosol Sci.* **1994**, *25*, 1179.

(16) Duft, D.; Atchtzehn, T.; Muller, R.; Huber, B. A.; Leisner, T. *Nature* **2003**, *421*, 6919.

(17) Zeleny, J. *Phys. Rev.* **1917**, *10*, 1.

(18) Macky, W. A. *Proc. Roy. Soc. A* **1931**, *133*, 565.

(19) O'Konski, C. T.; Thacher, H. C. *J. Phys. Chem.* **1953**, *57*, 955.

(20) Taylor, G. *Proc. R. Soc. London, Ser. A* **1964**, *280*, 383.

(21) Inculet, I. I.; Kromann, R. *IEEE Trans. Ind. Appl.* **1989**, *25*, 945.

(22) Saville, D. A. *Annu. Rev. Fluid Mech.* **1997**, *29*, 27.

(23) Abbas, M. A.; Latham, J. *J. Fluid Mech.* **1967**, *30*, 663.

(24) Abbas, M. A.; Latham, J. *Q. J. R. Met. Soc.* **1969**, *95*, 63.

(25) Vizika, O.; Saville, D. A. *J. Fluid Mech.* **1992**, *239*, 1.

(26) Ha, J. W.; Yang, S. M. *J. Fluid Mech.* **2002**, *405*, 131.

(27) Eow, J. S.; Ghadiri, M. *Chem. Eng. Process.* **2003**, *42*, 259.

(28) Chen, B. T.; John, W. Instrument Calibration. In *Aerosol Measurement: Principles, Techniques, and Applications*; Baron, P. A., Willeke, K., Eds.; Wiley-Interscience: New York, 2001; pp 627.

(29) Dahl, D. A. *SIMION 3D*; Idaho Natl. Eng. and Environ. Lab.: Idaho Falls, Idaho, 2000.

(30) Baker, R. J.; Johnson, B. P. *Rev. Sci. Instrum.* **1992**, *63*, 5799.

(31) Continetti, D. M.; Cyr, D. R.; Neumark, D. M. *Rev. Sci. Instrum.* **1992**, *63*, 1840.

(32) Leisner, T. *Spindle analysis program*; Technische Universität Ilmenau: Ilmenau, Germany, 2004.

(33) Feng, J. Q.; Beard, K. V. *Proc. R. Soc. London, Ser. A* **1990**, *430*, 133.

(34) Brazier-Smith, P. R.; Brook, M.; Latham, J.; Saunders, C. P.; Smith, M. H. *Proc. R. Soc. London, Ser. A* **1971**, *322*, 523.

(35) Becker, E.; Hiller, W. J.; Kowalewski, T. A. *J. Fluid Mech.* **1991**, *231*, 189.

(36) Basaran, O. A.; Scriven, L. E. *Phys. Fluids A* **1989**, *1*, 795.

(37) Hager, D. B.; Dovichi, N. J.; Klassen, J.; Kebarle, P. *Anal. Chem.* **1994**, *66*, 3944.

(38) Hager, D. B.; Dovichi, N. J. *Anal. Chem.* **1994**, *66*, 1593.

(39) Gomez, A.; Tang, K. *Phys. Fluids* **1994**, *6*, 404.

(40) Takeda, K.; Nakajima, A.; Hashimoto, K.; Watanabe, T. *Surf. Sci.* **2002**, *519*, L589.

Chapter 8. Online field-induced droplet ionization mass spectrometry probes heterogeneous reaction chemistry at the air – droplet interface: soft-sampling the products of the oleic acid – ozone reaction from single droplets

8.1. Abstract

Mechanically suspended droplets undergo chemical reactions and field-induced droplet ionization – mass spectrometry (FIDI-MS) characterizes the reaction products. Droplets containing either 10 μM oleic acid or 100 μM oleoyl-L-α-lysophosphatidic acid, LPA (18:1), react with gas-phase ozone for a specified reaction time up to one minute. At the droplet surface, ozone reacts with the double bonds generating intermediate ozonides before forming aldehydes and organic acids. Following a specified reaction time, a high electric field is rapidly applied to induce FIDI, generating jets of highly charged progeny that are characterized by mass spectrometry. When sampled at multiple reaction times, the spectra show a successively increasing ratio between the products and reactants. Reactions between ozone and LPA produce species that unambiguously localize the position of the double bond along the hydrocarbon chain. These studies indicate that FIDI-MS is a viable technique for kinetic studies of heterogeneous reactions on microdroplets.

8.2. Letter

Single droplet mass spectrometry represents an ideal solution to the challenges presented by the analysis of microliters of sample and the on-line characterization of heterogeneous reaction chemistry occurring on individual droplets. Researchers consider the reaction of gas-phase ozone with oleic acid as a model system for heterogeneous reaction chemistry and its implications for atmospheric chemistry.[1-5] Scheme 8.1 summarizes the reaction and expected products from the ozonolysis of oleic acid droplets. Briefly, ozone adds across the oleic acid (**1**) double bond forming a primary ozonide (**2**). This ozonide dissociates to an aldehyde and an energetic Crigee intermediate. In the presence of inert solvents, the intermediate may transfer energy and recombine with the aldehyde forming a secondary ozonide (**3**).[6,7] The secondary ozonide subsequently dissociates forming 9-oxononanoic acid (**4**), 1-nonanoic acid (**5**), azelaic acid (**6**), and nonanal (**7**).[1] The short (~10 nm) characteristic diffusion distance of ozone into oleic acid before reaction supports the model of a heterogeneous reaction at the air-droplet interface.[4,5] This reaction is well-studied but questions remain regarding the partitioning of products and the relative yields from the ozonolysis in Scheme 8.1.[1]

Recently our laboratory pioneered field-induced droplet ionization – mass spectrometry (FIDI-MS).[8] In a critically high electric field, E_c^0, given by eq (8.1), neutral droplets elongate parallel to the field, developing two opposing conical tips that emit jets of oppositely charged progeny droplets.[9-11]

$$E_c{}^0 \approx \left(\frac{5.28\sigma}{8\pi\varepsilon_0 r} \right)^{1/2} \tag{8.1}$$

This critical field is known as the Taylor limit, named for G. I. Taylor, where ε_0 is the permittivity of free space while r and σ are the droplet radius and surface tension, respectively. Using a constant stream of droplets generated by a vibrating orifice aerosol generator, we demonstrated that the charged progeny droplets are a viable source of gas-phase ions for mass analysis.[8] Rapidly switched electric fields and synchronized visualization allowed us to characterize the dynamics of the FIDI process. The timescale of droplet elongation, tip formation, and progeny droplet generation slightly above E_c^0 is related to the timescale of the natural harmonic oscillations slightly below E_c^0. Equation (8.2) approximates the timescale for FIDI, τ_{FIDI}, and is a function of bulk solution parameters including the density, ρ.[12]

$$\tau_{\text{FIDI}} = 2.3\left(\frac{r^3\rho}{\sigma}\right)^{1/2} \qquad (8.2)$$

Understanding the critical field and the timescale for FIDI enables new applications of mass analysis to chemical reactions. For instance, droplets can serve as miniature reaction cells prior to FIDI-MS. During this time, suspended droplets may undergo heterogeneous reactions in an electric field-free environment whose products are mass analyzed when the electric field is rapidly applied. Such applications motivate the present study where gas-phase ozone reacts with unsaturated analyte molecules within the droplets.

Individual droplets are mechanically suspended between a switched high voltage electrode and the capillary inlet to a Finnigan LCQ Deca ion trap mass spectrometer as shown in Figure 8.1. Under the initial conditions, the capillary, tubing, and electrode are maintained at electrical ground. Reactant solutions manually fed through the tubing establish a ~1 mm diameter droplet in an electric field-free environment. A UV pen-ray lamp generates ~30 ppm ozone in air that continually washes through the FIDI region. Heterogeneous reactions between ozone and solution-phase analytes occur for a time 0-60 s between the point the droplet is established and sampled by FIDI-MS. A high voltage pulse on the electrode applies a strong electric field to the droplet resulting in the ejection of jets of small, highly charged progeny droplets. The high voltage pulse establishes a 1.5×10^6 V m^{-1}, ~5 ms field to achieve jetting and FIDI as required by eqs (8.1) and (8.2). After FIDI-MS, pushing additional solvent through the tubing causes the existing droplet to fall off and establishes a fresh droplet for reaction.

Figure 8.2 shows the negative ion FIDI-MS spectra for the reaction between 10 μm oleic acid in 90% DMF and 10% methanol with 30 ppm ozone delivered by 500 mL min^{-1} air. The singly deprotonated dimer at 563 m/z dominates the FIDI-MS spectrum of oleic acid in the absence of ozone (frame A). Upon exposure to ozone, the droplets react with the ozone for a variable length of time before FIDI-MS samples the contents of the droplets. Frames (B)-(E) show varying relative concentrations of the reactants (563 m/z) and the products after instantaneous (< 1 s), 5 s, 20 s, and 60 s, respectively. Reaction products include deprotonated azelaic acid (**6**), at 187 m/z, doubly hydrated azelaic acid at 223 m/z and an unknown cluster containing azelaic acid at 250 m/z. Collision-induced dissociation (CID) reactions of the 187 m/z ion are identical to the CID spectra from pure azelaic acid purchased from Sigma Aldrich. Low energy CID spectra of the 223 m/z and 250 m/z ions principally produce singly deprotonated azelaic acid indicating cluster parent ions. Deprotonated 9-oxononanoic acid (**4**), is principally observed at 453 m/z complexed to oleic acid. After 60 s, spectra show a small quantity of deprotonated 9-

oxononanoic acid at 171 m/z. Deprotonated nonanoic acid (**5**), is not observed as expected at 157 m/z. Peaks due to nonanal are not expected because negative ion soft-sampling produces poor signal from aldehydes and previous research shows nonanal partially partitioning into the vapor phase.[5] Figure 8.2 demonstrates that mass sampling the droplet by FIDI-MS is a viable route to the kinetics of heterogeneous chemistry with a soft-sampling analysis. Ongoing studies seek to quantify rate constants for reactions sampled by FIDI-MS.

In addition to heterogeneous reaction kinetics, the reaction between ozone and solution-phase analytes and FIDI-MS characterization localizes carbon-carbon double bonds within a molecule. We verify this with the reaction between ozone and 100 μm oleoyl-L-a-lysophosphatidic acid, or LPA (18:1), in methanol. Scheme 8.2 shows LPA (18:1) (**8**), and the expected aldehyde (**9**), and acid (**10**), reaction products based on the FIDI-MS results for the oleic acid / ozone reaction. Figure 8.3A shows the negative ion FIDI-MS spectrum of LPA (18:1) in the absence of ozone. Primary peaks are due to deprotonated LPA (18:1) at 453 m/z, a deprotonated dimer at 871 m/z, a doubly deprotonated sodium-bound adduct at 893 m/z, and a deprotonated ester cleavage product at 153 m/z. Figure 8.3B shows the FIDI-MS spectrum for droplets exposed to ozone for 5 s. The strong peak at 325 m/z confirms the deprotonated aldehyde reaction product (**9**). Additionally, the deprotonated acid product (**10**), appears as a weak signal at 341 m/z in addition to a strong, unknown peak at 373 m/z.

Deprotonated reaction products at 325 m/z and 341 m/z respectively correspond to the formation of an aldehyde and an organic acid at the 9th carbon atom in the ester. This is indeed the location of the double bond in LPA (18:1) indicating that FIDI-MS successfully localizes double bonds and characterizes the reaction products with a soft-sampling ionization method.

FIDI-MS allows for real-time monitoring of the reaction chemistry in single droplets. Such reactions may include environmental studies involving online characterization of the kinetics of heterogeneous reactions between gas-phase and solution-phase species, and solution-phase photoinitiated reactions whose products are sampled by FIDI-MS after a predetermined reaction time. The applications may also be extended to include the examination of free droplets suspended in an electrodynamic balance or acoustically levitated.

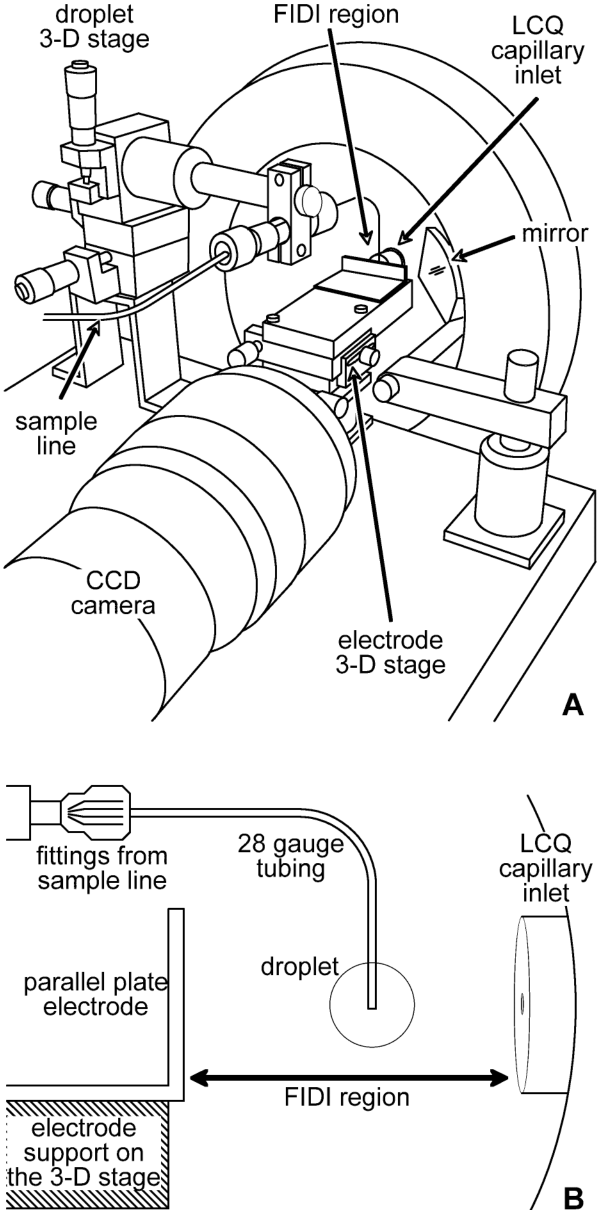

Figure 8.1. Schematic of the single droplet FIDI-MS apparatus (A) and the FIDI region (B). A droplet is mechanically suspended in the high field FIDI region defined by a parallel plate electrode and the LCQ capillary inlet. Independent three-dimensional translation stages align the droplet and the electrode. A CCD camera visualizes the FIDI region and the droplet is oriented such that the charged progeny jets are directed into the MS capillary for mass analysis.

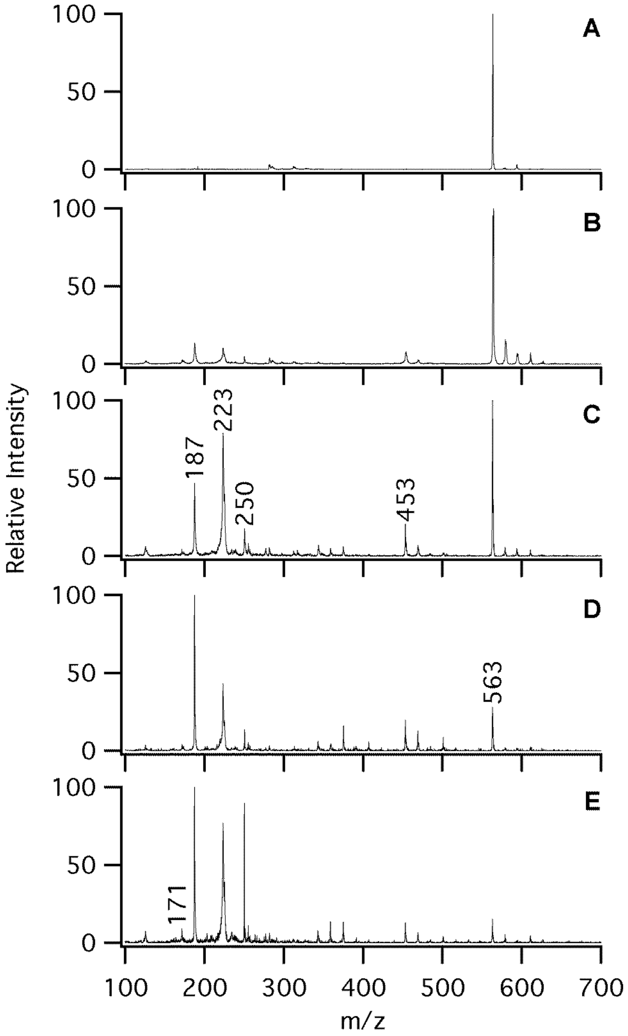

Figure 8.2. Oxidation of oleic acid by ozone as a function of time. In the absence of ozone, the negative ion FIDI-MS spectrum of oleic acid is dominated by the singly-deprotonated dimer peak at 563 m/z. Successive frames show reaction with (B) <1 s, (C) 5 s, (D) 20 s, (E) 60 s, exposures. Oxidation products are dominated by deprotonated azelaic acid at 187 m/z, doubly hydrated deprotonated azelaic acid at 223 m/z, an unknown cluster containing azelaic acid at 250 m/z, and a deprotonated oleic acid / azelaic acid cluster at 453 m/z.

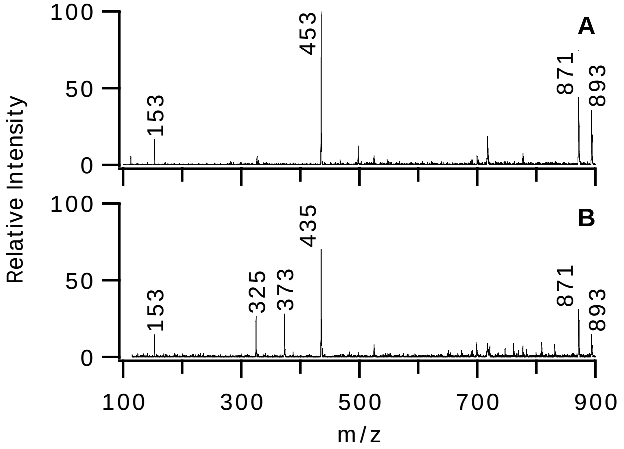

Figure 8.3. Oxidation of LPA (18:1) by ozone unambiguously demonstrates the location of the double bond along the hydrocarbon tail. In the absence of ozone (A), the singly-deprotonated monomer at 453, the singly deprotonated dimer at 871, and the sodium-bound dianion peak at 893 m/z dominate the negative ion FIDI-MS spectrum of LPA (18:1). Frame (B) shows the FIDI-MS spectrum containing the reaction products following 5 second exposures to ozone including the aldehyde product peak at 325 m/z, a weak signal at 341 m/z from the acid product, and an unknown peak at 373 m/z.

Scheme 8.1. Oxidation of oleic acid (**1**) by ozone on surfaces proceeds through primary (**2**) and secondary (**3**) ozonides before forming 9-oxononanoic acid (**4**), nonanoic acid (**5**), azelaic acid (**6**), and nonanal (**7**).

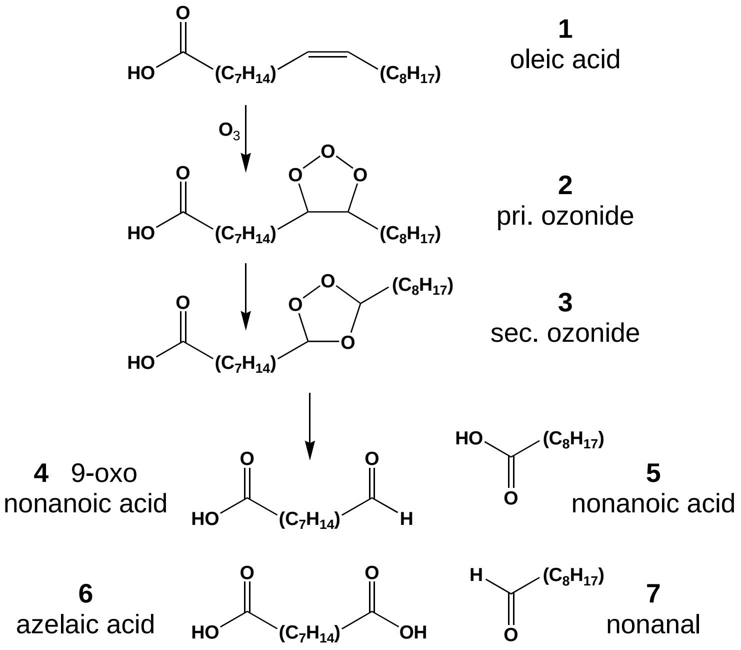

Scheme 8.2. Expected products in the ozonolysis of LPA (18:1) (**8**) are the aldehyde reaction product (**9**) and the acid reaction product (**10**).

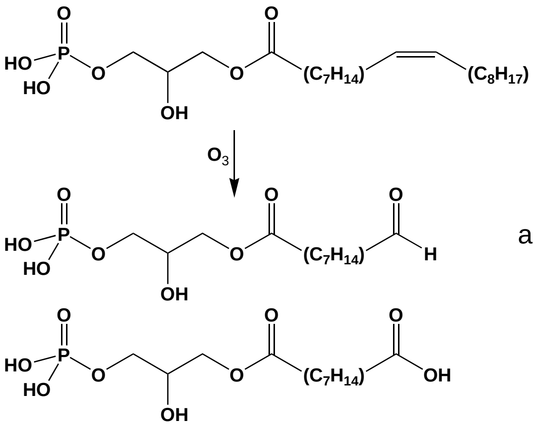

8
LPA (18:1)

9
aldehyde product

10
acid product

8.3. References

(1) Hung, H. M.; Katrib, Y.; Martin, S. T. *J. Phys. Chem. A* **2005**, *109*, 4517.

(2) Knopf, D. A.; Anthony, L. M.; Bertram, A. K. *J. Phys. Chem. A* **2005**, *109*, 5579.

(3) Katrib, Y.; Martin, S. T.; Hung, H. M.; Rudich, Y.; Zhang, H. Z.; Slowik, J. G.; Davidovits, P.; Jayne, J. T.; Worsnop, D. R. *J. Phys. Chem. A* **2004**, *108*, 6686.

(4) Smith, G. D.; Woods, E.; DeForest, C. L.; Baer, T.; Miller, R. E. *J. Phys. Chem. A* **2002**, *106*, 8085.

(5) Moise, T.; Rudich, Y. *J. Phys. Chem. A* **2002**, *106*, 6469.

(6) Wadia, Y.; Tobias, D. J.; Stafford, R.; Finlayson-Pitts, B. J. *Langmuir* **2000**, *16*, 9321.

(7) Finlayson-Pitts, B. J.; Pitts Jr., J. N. *Chemistry of the Upper and Lower Atmosphere: Theory, Experiments, and Applications*; Academic Press: San Diego, 2000.

(8) Grimm, R. L.; Beauchamp, J. L. *J. Phys. Chem. B* **2003**, *107*, 14161.

(9) Macky, W. A. *Proc. Roy. Soc. A* **1931**, *133*, 565.

(10) Taylor, G. *Proc. R. Soc. London, Ser. A* **1964**, *280*, 383.

(11) Basaran, O. A.; Scriven, L. E. *Phys. Fluids A* **1989**, *1*, 799.

(12) Grimm, R. L.; Beauchamp, J. L. *J. Phys. Chem. B* **2005**, *109*, 8244.

Appendix A. The design and implementation of a single-droplet source for field-induced droplet ionization mass spectrometry

A.1. Introduction

Single droplet mass spectrometry (MS) is achieved through field-induced droplet ionization. Applications of single droplet MS are discussed in Chapters 8 and 9, but these experiments represent only the initial stages of exciting and new applications for chemistry and the subsequent analysis of single droplets. This appendix is written with the intention that others may employ and even improve the designs and explore single droplet chemistry. Design considerations and safety requirements are presented and discussed for the single droplet FIDI source.

A droplet is mechanically suspended between a plate electrode and the sampling capillary of an ion trap mass spectrometer. A high voltage pulse on the electrode applies a strong electric field to the droplet resulting in the ejection of jets of charged progeny droplets. The design of an idealized single droplet FIDI source requires knowledge of the dynamics of the event including field strengths and the timescale over which FIDI occurs. Section A.2 discusses the theory and equations governing design considerations. Section A.3 presents drawings of the instruments, relevant electronic schematics, and mass spectrometer modifications. Sample positive ion mass spectra from a single droplet containing α lactalbumin are shown in Section A.4.

A.2. Theory and factors affecting design

As is mentioned throughout this thesis, field-induced droplet ionization occurs in droplets upon the application of a strong applied electric field. This field need not be constant or linear, and investigations into the FIDI dynamics establishes the critical field strength and duration for a droplet of known size and bulk physical constants. Excess electrical pressure leading to FIDI develops in droplets of radius r and surface tension σ when the applied field exceeds a critical value, E_c known as the Taylor limit eq (A.1), named for G. I. Taylor who pioneered the corresponding theory.[1-3]

$$E_c = \frac{1.625}{(8\pi)^{1/2}}\left(\frac{2\sigma}{\varepsilon_0 r}\right)^{1/2} \qquad \text{(A.1)}$$

Above the Taylor limit, droplets develop two opposing conical tips that emit fine jets of oppositely charged progeny droplets. Below the Taylor limit, droplets undergo field-dependent shape oscillations that dampen out to an equilibrium prolate elliptical shape as predicted by Taylor. Recent investigations in our laboratory demonstrate that the timescale of droplet elongation, tip formation, and progeny droplet generation slightly above the Taylor limit is related to the timescale of the oscillations slightly below the Taylor limit. The timescale to initiate FIDI, τ_{FIDI} is approximately 75% the time of an oscillation period, ν^{-1}, as the applied field approaches the Taylor limit as noted by eq (A.2).[4]

$$\tau_{\text{FIDI}} \approx 0.75\left(\nu_{E\to E_c}\right)^{-1} \qquad \text{(A.2)}$$

Thus, models of sub-critical shape oscillations become an important predictor for the timescales of FIDI. In exploring the oscillations of 225 μm methanol droplets below the

Taylor limit, we found good agreement between the experimental shape oscillations and the numerical model of Basaran and co-workers as well as the analytical model of Feng and Beard. Feng and Beard model the oscillation frequency ν_{FB} as a function of the applied field, and the droplet's natural $l = 2$ mode oscillation shown in eq (A.3).[5]

$$\nu_{\mathrm{FB}} = \frac{8^{1/2}}{2\pi}\left[1 - 2.764E^2\left(\frac{\varepsilon_0 r}{2\sigma}\right)\right]\left(\frac{\sigma}{r^3\rho}\right)^{1/2} \qquad \text{(A.3)}$$

The frequency decreases proportionally with E^2 until the Taylor limit is reached, at which point the frequency is given by eq (A.4).

$$\nu_{\mathrm{FB}}(E_c) = \frac{8^{1/2}}{2\pi}\left[1 - 2.764\frac{1.625^2}{8\pi}\right]\left(\frac{\sigma}{r^3\rho}\right)^{1/2} \qquad \text{(A.4)}$$

Equations (A.2) and (A.4) may be combined into eq (A.5) to show an approximate timescale for FIDI as a function of droplet size, density, and surface tension.

$$\tau_{\mathrm{FIDI}} \approx 2.3\left(\frac{r^3\rho}{\sigma}\right)^{1/2} \qquad \text{(A.5)}$$

Equations (A.1) and (A.5) are critical when designing a FIDI source. Likewise, other design factors must be considered regarding the size and separation of the electrodes that establish the electric field. When using a parallel plate capacitor configuration, the electric field is the familiar $E = V / d$ where V is the voltage difference and d is the distance between the electrodes. If design constraints limit the maximum voltage to a value $V_{\max}$, the maximum plate spacing is likewise limited to a value $d_{\max}$, shown in eq (A.6). Here the field necessary for FIDI from (A.1) represents the minimum field that restricts $d_{\max}$.

$$d_{\max} = \frac{2V_{\max}}{1.625}\left(\frac{\pi\varepsilon_0 r}{2\sigma}\right)^{1/2} \qquad \text{(A.6)}$$

As expected, higher voltages afford a greater plate separation. Equation (A.6) also suggests the maximum plate separation increases with $r^{1/2}$ because larger droplets require lower field strengths for FIDI. Unfortunately, the dielectric breakdown limit of air and non-linear field effects also limit plate spacing. For instance, the breakdown of air is ideally ~30 kV cm^{-1}, however arcing often occurs at lower field strengths.

Similarly, the droplet itself will distort the electric field. These distortions may be minimized by maximizing the ratio between the plate spacing, d, and the droplet diameter, $2r$, which is derived from eq (A.6).

$$\frac{d_{\text{max}}}{2r} = \frac{V_{\text{max}}}{1.625}\left(\frac{\pi\varepsilon_0}{\sigma r}\right)^{1/2} \tag{A.7}$$

Although (A.1) predicts that larger droplets require lower fields, eq (A.7) shows that smaller droplets will minimize the field distortions and maximize the plate spacing to droplet size ratio proportionally with $r^{-1/2}$.

Thus when designing a FIDI source, it is important to consider droplet size, E_{c}, V_{max} and τ_{FIDI}. The timescale is important because it determines what electric schematics are necessary for rapidly switching the electric fields. Generally, droplets in the micron size regime have FIDI timescales on the order of tens to hundreds of microseconds. At this speed high voltage solid state switching transistors are necessary to rapidly switch on and off the fields. Larger, millimeter-sized droplets have FIDI timescales on the order of milliseconds. This longer timescale allows the replacement of high voltage transistor circuits with reed relays and more modest electronics.

A.3. Instrument design and description

The single droplet source is mounted in front of the Beauchamp group LCQ Deca (ThermoFinnigan) ion trap mass spectrometer. All discussions are geared towards this implementation and should be taken into consideration when designing a source for a different mass spectrometer.

A.3.1. FIDI hardware

Figure A.1 shows an illustration of the apparatus mounted relative to the LCQ capillary inlet. The FIDI source consists of multiple parts which are all mounted on a 5 by 7 inch acrylic sled that sits on the rails designed for the commercial electrospray source. The FIDI region is defined by a parallel plate electrode and the capillary inlet itself. A mechanically suspended droplet bisects the field. Frame B of Figure A.1 shows this region in greater detail.

The droplet hangs from a 28-gauge stainless steel tube (HTX-28-24, Small Parts, Inc.). The tube connects to a sample line and the syringe through Upchurch Scientific fittings. The solution to be analyzed is fed through the tube until a 1-2 mm diameter droplet forms at the bottom of the tube. The tube and fittings are mounted on a small three-dimensional stage that adjusts to direct the progeny jets into the capillary inlet of the LCQ. The parallel plate electrode is also mounted on an independent three-dimensional stage allowing precise control of *d*, the spacing between the electrode and

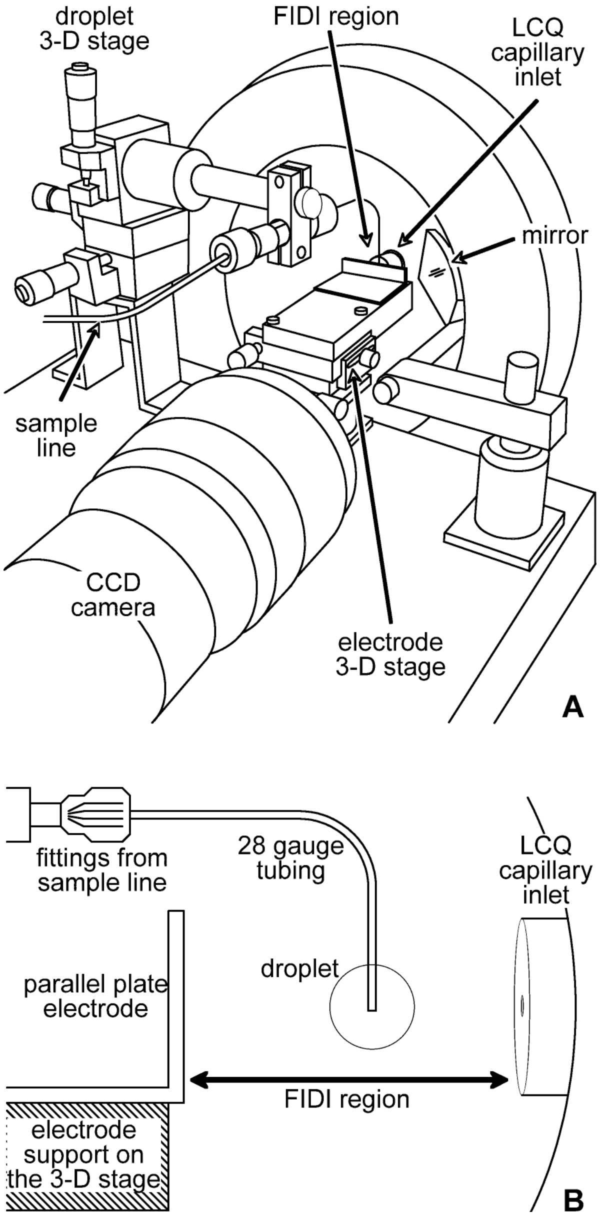

Figure A.1. Diagram of the single droplet FIDI-MS setup. Frame A shows a perspective illustration of the source relative to the capillary inlet on the LCQ mass spectrometer. A sample line delivers solution and analyte to a 28-gauge hypodermic tube forming a droplet on the bottom. At the bottom of the tube, the droplet is mechanically suspended between the LCQ capillary inlet and a parallel plate electrode which establish the FIDI field (Frame B). Both the tubing and the electrode are on separate three-dimensional stages. A mirror and CCD camera enable side-on visualization of the FIDI region.

the capillary. The FIDI region is monitored with a CCD camera and a mirror which are each mounted on the sled. The camera allows a side-on view of the FIDI region that assists with aligning the droplet relative to the electrode and capillary and provides information on droplet size.

Droplets in this study are roughly 1-2 mm in diameter. This is an important parameter for determining the field strengths and durations needed to achieve jetting and progeny formation. At this size, eqs (A.1) and (A.5) predict $E_c \sim 13$ kV cm^{-1} and $\tau_{\mathrm{FIDI}} \sim 9$ ms for aqueous droplets. For a typical organic droplet where $\sigma = 0.020$ N m^{-1} and $\rho = 800$ kg m^{-3}, these equations predict $E_c \sim 7$ kV cm^{-1} and $\tau_{\mathrm{FIDI}} \sim 15$ ms.

Under initial conditions, the capillary, tubing and electrode are maintained at electrical ground. The liquid sample is fed through the tubing to establish the proper droplet size in a field-free environment. At a user-defined point, an electric field is established using two high voltage (HV) switching circuits. The electrode voltage switches from ground to HV and the tubing voltage switches from ground to HV/2. These voltages remain for a time $t \sim \tau$ before returning to ground. Throughout this time, the capillary remains at electrical ground. Typically HV = 7-9 kV and HV/2 = 3.5-4.5 kV. When sampling positively charged droplets into the mass spectrometer for a positive ion mass spectrum, both HV and HV/2 deliver positive voltage. Conversely, negative high voltage settings direct negatively charged progeny into the instrument for a negative ion mass spectrum. Following the time t, the electrode and hypodermic tube return to electrical ground. The parent droplet remains mechanically suspended and may be sampled by FIDI repeatedly until the volume of the droplet decreases such that the applied field is below the Taylor limit given by eq (A.1).

A.3.2. Electronics

The millisecond timescales required for FIDI of 1-2 mm droplets simplifies the electronic circuits. Previous investigations on the dynamics of jetting and progeny formation focused on the behavior of 225 μm diameter methanol droplets. For these droplets, FIDI timescales are between 400 and 700 μs depending on the applied field strength. Such timescales require custom circuitry and high-voltage MOSFET switches to achieve rapid (≤ 1 μs) switching of the high voltage. In the case of 1-2 mm droplets, solid state switching circuitry may be replaced with commercial high voltage reed relays.

Figure A.2 shows the electrical schematic for the experiment. In frame A, a 74LS123 monostable vibrator generates a 5V pulse when a pushbutton switch SW1 is closed by the operator. The capacitor C_{ext} = 30 μF and the R_{ext} = 10 kΩ potentiometer determine a pulse length between 1 and 10 ms. The waveform passes through two inverting Schmitt triggers that are inside a single 74LS14 package. The Schmitt triggers provide a test point (TP1) for a digital oscilloscope that monitors the waveform and pulse length, and proved the necessary current to drive the switching circuitry.

Frames B and C are each a switching circuit connected to the FIDI 28-gauge tube and electrode, respectively. Both switches consist of a 6N135 optoisolator and a 2N6388 Darlington transistor to drive the reed relay from the pulse provided by the monostable multivibrator. Figure A.2B shows the HV/2 switch for the 28-gauge tubing. The input $HV/2_{in}$ refers to an external power supply delivering between 3.5 and 4.5 kV. The circuit uses a Magnecraft W102VX-50 reed relay capable of switching up to 5 kV. The

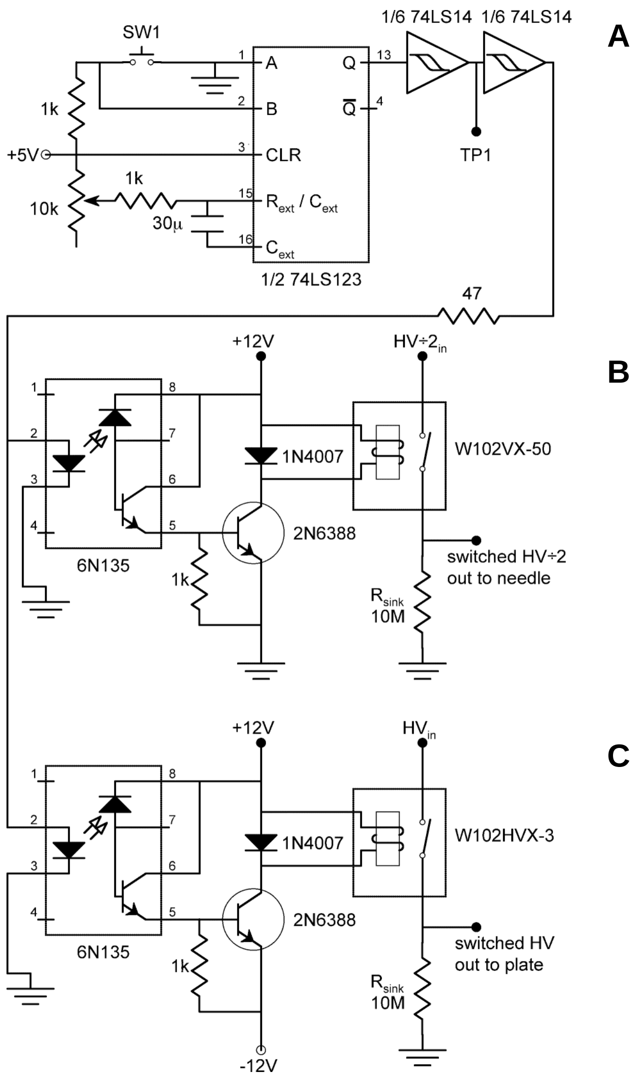

Figure A.2. Schematic diagram of the single droplet FIDI electronics. The FIDI pulse length is determined by capacitor C_{ext} and potentiometer R_{ext} in the 74LS123 monostable vibrator. When the switch (SW1) is closed, the generated pulse passes through two Schmitt triggers to provide a clean test point (TP1) for an oscilloscope and to provide enough current to drive the two high voltage switching circuits in frames B and C. Each switch consists of an optoisolator and a 2N6388 high power Darlington transistor. The switch in frame B provides the HV/2 voltage to the 28-gauge tube and the switch in frame C provides the HV to the parallel plate electrode.

HV switch in Figure A.2C is similar, however it employs a W102HVX-3 relay that may switch up to 10 kV because HV_{in} is typically between 7 and 9 kV. Because both relays are polarity agnostic, directing positive or negative progeny into the mass spectrometer does not require modifications to the circuit; only the polarity of the power supplies need be reversed. Each switch contains a sink resistance, R_{sink}, of 10 MΩ. This resistance is a four-by-four array of 10 MΩ, 1 Watt resistors where four sets of four parallel resistors are arranged in series. In this configuration, each resistor in the array is only sinking one quarter of the total voltage and one sixteenth of the total power. These arrays reduce the total load in accordance with the design limitations of the individual resistors.

A.3.3. LCQ mass spectrometer

A small number of modifications are required for the LCQ to successfully operate with the single droplet FIDI source. The commercial ESI or APCI head must be removed to accommodate the FIDI sled. Because the capillary inlet is grounded in the experiment, the wire delivering voltage to the body of the capillary is disconnected so that sparks and electrical discharges in the FIDI source are not directed through the capillary into the LCQ electronics. The capillary is well connected to an electrical ground.

FIDI acquisition occurs in the same manner as electrospray acquisition with few modifications. In the present design the activation and occurrence of FIDI is not coordinated with the LCQ acquisition. Therefore individual acquisition times are set to high values. Specifically the number of microscans is set to one, and the maximum inject time is set to 1000 ms (one second). The long acquisition time means the FIDI events need not be coordinated with the LCQ acquisition.

The remaining user-controlled instrument parameters are optimized using the same sample with the conventional ESI source. Parameters are tuned according to the built-in capabilities of the instrument.

A.4. Sample mass spectra

Figure A.3 shows the positive ion mass spectrum of α lactalbumin acquired with the single droplet FIDI source. The distribution of peaks is consistent with a multiply-charged protein and resembles an electrospray mass spectrum of the same solution under the same LCQ conditions.

A.5. Conclusions

Single droplet FIDI-MS opens new avenues in chemical and biological research. This chapter describes the single droplet FIDI source as well as design considerations and circuit schematics. Mass spectra from a single droplet of α lactalbumin are presented.

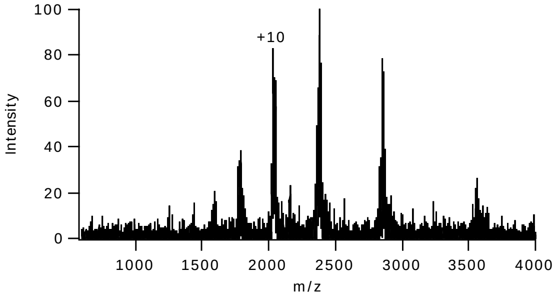

Figure A.3. FIDI-MS spectrum of 10 μm α lactalbumin in 50% water 50% acetonitrile. The distribution of peaks is indicative of a multiply-charged protein.

A.6. References

(1) Taylor, G. *Proc. R. Soc. London, Ser. A* **1964**, *280*, 383.

(2) Taylor, G. *Proc. R. Soc. London, Ser. A* **1966**, *291*, 159.

(3) Basaran, O. A.; Scriven, L. E. *Phys. Fluids A* **1989**, *1*, 799.

(4) Grimm, R. L.; Beauchamp, J. L. *J. Phys. Chem. B* **2005**, *109*, 8244.

(5) Feng, J. Q.; Beard, K. V. *Proc. R. Soc. London, Ser. A* **1990**, *430*, 133.

Appendix B. Experimental schematic and circuit diagrams for the vibrating orifice aerosol generator and the high-speed, high-voltage switch employed in the dynamics experiment

B.1. Introduction

Field induced droplet ionization mass spectrometry (FIDI-MS) is a useful technique with applications to chemical and biological analysis, but many questions remain regarding the chemistry and physics of the process. This appendix serves to more rigorously cover the experimental details of the FIDI dynamics experiment recently published.[1] The vibrating orifice aerosol generator (VOAG) and electronic circuits are presented and discussed in detail. Pertinent design considerations and safety requirements are discussed in the context of designing future dynamics and mass spectrometric applications for field-induced droplet ionization.

Figure B.1 shows a schematic representation of the hardware employed for the study of FIDI dynamics presented in Chapter 7.[1] Briefly, a vibrating orifice aerosol generator breaks a stream of methanol into monodisperse droplets. These droplets pass between two plates that establish a switched high electric field with custom electronics. All of this hardware was produced in-house and discussed below. Section B.2 illustrates

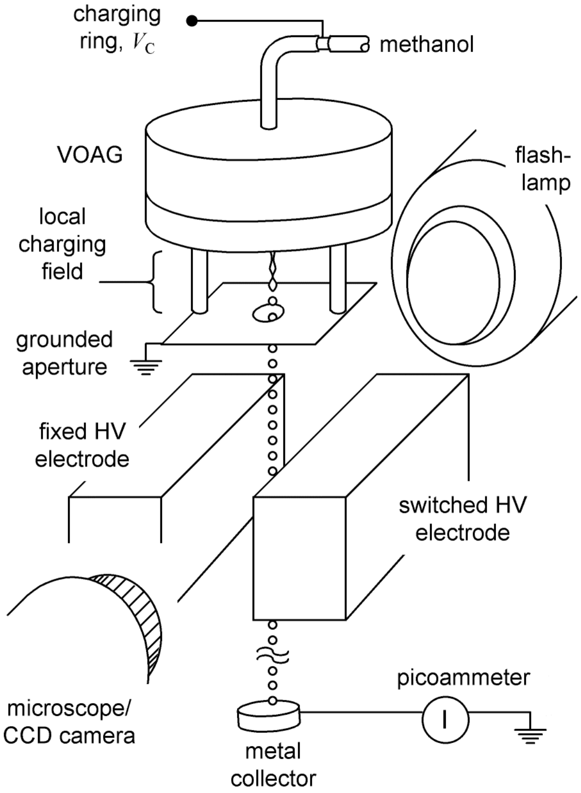

Figure B.1. Schematic of the experimental apparatus employed for the dynamics experiment presented in Chapter 7. Details of the construction of the vibrating orifice aerosol generator are discussed in section B.2. Electronic schematics for the high voltage switching circuit are presented in section B.3. Reprinted from Grimm and Beauchamp.[1]

the design of the VOAG. Section B.3 presents the schematic diagram of the electronic circuits that control the switched electric fields in the experiment. Lastly, section B.4 discusses the considerations and constraints for designing future experiments.

B.2. Vibrating orifice aerosol generator for the dynamics experiment

Vibrating capillary and vibrating orifice aerosol generators produce highly monodisperse liquid aerosols in the micron size range. A brief review by Chen and John details the technique and physics behind this method of aerosol generation.[2] Our VOAG is an in-house design that employs an annular piezoelectric crystal to vibrate a ceramic nozzle.

B.2.1. Aerosol generator design

Capillary instability dictates that the liquid stream exiting the ceramic nozzle will break into droplets at a natural frequency determined by the stream diameter, speed, and surface tension. Without an external influence this breakup is unstable and leads to broad distribution in droplet sizes. When the droplets exit an orifice vibrating at the natural breakup frequency, the superposition vibrations result in steady breakup and monodisperse droplets.

Figure B.2 shows both perspective (A) and cutaway (B) views of the VOAG source. A 1/32 inch inner diameter, 3/32 inch outer diameter silicone tube serves as the sample line that delivers methanol to the VOAG. Liquid is delivered to the sample line from a 500 mL methanol reservoir under ~1-3 psig pressure. This nitrogen backing provides less control but a more steady flow than a syringe pump. Because droplet size is dependent on flow rate, a steady flow is critical to the formation of monodisperse droplets.

A 130 μm I.D. ceramic orifice (4P480-0016-343; Kulicke and Soffa Inc., Willow Grove, PA) is connected to the end of the sample line. The ceramic tip has a 1/16 inch O.D. at the non-orifice side which creates a tight seal with the 1/32 inch I.D. silicone without the need for further clamping or sealing. Smooth flow through the orifice is critical for monodisperse droplet generation with a minimum of satellite droplets. The stability is verified by observing the flow of methanol through the orifice when removed from the VOAG.

The VOAG head consists of a piezoelectric actuator mounted between a piece of Delrin and aluminum. The annular piezoelectric element is 1/4 inch tall with a 1 inch O.D. and a 5/8 inch I.D. The actuator sits in a circular piece of Delrin machined into an upside-down "hat" shape. The actuator is held into place by a disk of aluminum that is 1/8 inch thick. The Delrin hat is mounted to a piece of Teflon on a three-dimensional translation stage that allows precise alignment of the droplet stream relative to the high field region.

The piezo actuator axially expands and contracts imparting a vibration to the entire VOAG head. A 3/32 inch diameter hole though the Delrin and aluminum allows the sample line and ceramic orifice to be positioned inside the VOAG head. The slight expansion of the silicone tubing around the ceramic allows for good mechanical contact with the VOAG head so that the mechanical oscillations are transferred to the orifice. Piezoelectric action is initiated by the application of a square wave to the piezo element.

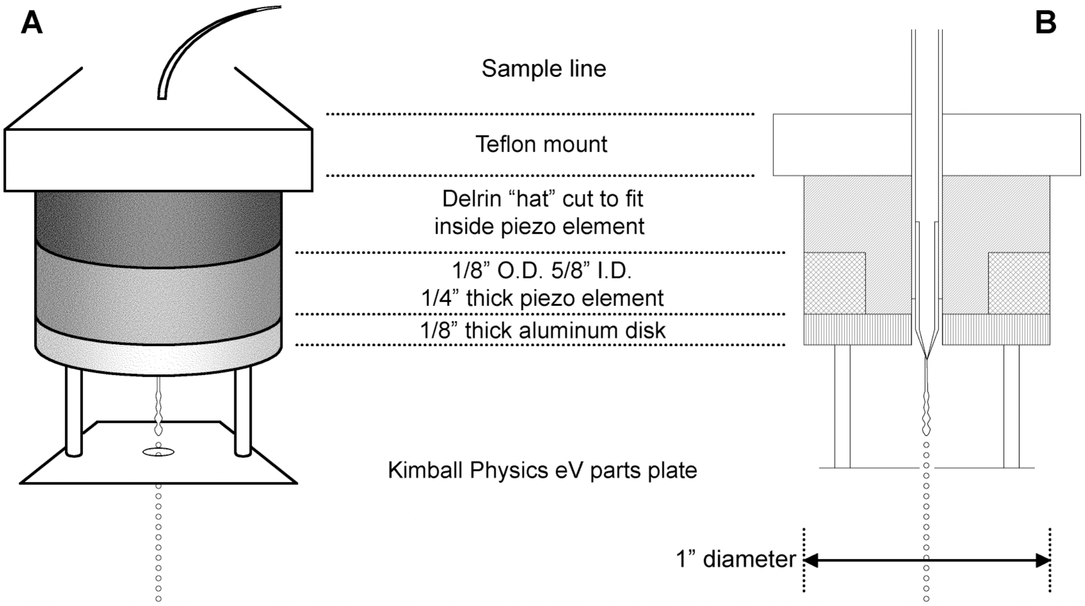

Figure B.2. Perspective (A) and cutaway (B) drawing of the VOAG source.

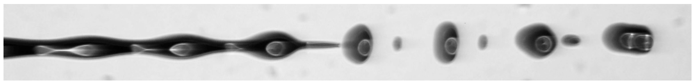

Figure B.3. Capillary instability and droplet formation guided by a vibrating orifice. Primary droplets are 225 μm and are accompanied by smaller satellite droplets.

The 5 V TTL output of a Pentek model 3100 digital frequency synthesizer provides this square wave. The orifice diameter and solution flow rate establish a natural breakup frequency between 9 and 11 kHz for methanol. One side of the piezo element is electrically connected to the aluminum disk which is set at a voltage V_c discussed in section B.2.2. As a result, the square wave must float at V_c and is correspondingly passed through an optoisolator circuit discussed in section B.3.1.

Figure B.3 shows a flashlamp-illuminated image of stream breakup and droplet formation. The stream clearly shows a wave superimposed on the column of liquid prior to breakup. Breakup results both 225 μm methanol droplets and smaller satellite droplets common to vibrating aerosol generators. The droplets move at ballistic speeds with little drag because the air column between the droplets roughly travels along with the droplets.

B.2.2. Generating charged droplets

In an electric-field free environment, droplets produced by a VOAG show a small statistical charge distribution on the order of hundreds of elementary charges. Establishing an electric field in the region where droplets break off of the liquid column allows us to control the net charge on the droplets. In our design, this is accomplished by connecting both the methanol sample line and the aluminum plate to a voltage supply V_c and placing a grounded plate below the point at which the stream breaks into droplets. As shown in Figure B.2, this plate is set 1 cm off of the aluminum disk through the use of nylon screws and ceramic spacers. The voltage V_c was varied between 0 and 600 V resulting in droplets with charge as high as 13% of their Rayleigh limit.

Higher voltages and charges closer to the Rayleigh limit are experimentally attainable but not practical for our dynamics experiment. This is attained by either increasing V_c or by allowing the droplets to evaporate to a higher charge density. At higher charge values, space-charge repulsion between the droplets causes radial movement beyond the droplet stream. This results in a fine mist unsuitable for the experiment. Future experiments could explore the impact of higher droplet charge by using a different technique to generate charged droplets, or by selecting a small number of droplets from the charged droplet “mist”.

B.3. Electric circuits employed in the dynamics experiment

B.3.1. Optoisolator circuits

Optoisolators employ a light emitting diode (LED) to switch a phototransistor within a single, sealed package. Signals are transferred through the LED-phototransistor pair, but cannot go the other way. This has two applications, both of which are employed in the dynamics experiment. Firstly, the input signal is isolated from electrical noise generated by devices connected to the optoisolator output. Noise cannot be transferred back to the controlling circuitry. Secondly, the output stage may be set at a completely different reference voltage than the input stage. Thus signals may be “floated” or sent to a device with a different ground than the controlling circuit.

Figure B.4A shows the schematic configuration of the optoisolators employed in the dynamics experiment. The optoisolator itself is either a 6N135 or an HCPL-4502 which are functionally identical used interchangeably. The LED side contains a 47 ohm resistor that current-limits the incoming signal. The phototransistor is wired in an emitter-follower configuration such that the shape of the output pulse directly mimics the input pulse. A 6V lantern battery supplies the for the output pulse.

In cases where the optoisolator serves to isolate a signal due to electrical noise concerns, the floating high voltage (HV) input is wired to the same ground as the input signal. In cases where the output pulse is floating relative to HV, that voltage is wired to the "floating HV or ground in" connection. As an example, an optoisolator delivers the square wave signal to the piezoelectric actuator in the VOAG. The square wave input is a TTL signal and the output signal is a 6V square wave relative to V_c.

Because this circuit is used often in these experiments, the circuit is designed to be modular and inserted between sources and devices where necessary. In schematics presented later in this chapter, this circuit is approximated by the shorthand notation shown in Figure B.4B.

B.3.2. Synchronization of switched fields and droplet generation

High speed photography of droplets exposed to a high field for a specified period of time requires precision synchronization of field switching, flashlamp firing, and VOAG frequency. Figure B.5 illustrates the pulse sequences within the dynamics experiment. The high voltage and flashlamp control electronics trigger off of the VOAG square wave (Figure B.5A), which is a 5V TTL signal that oscillates at ν_{VOAG}. The square wave signal passes through two "decade" counters that generate square waves of frequencies $\nu_{\mathrm{VOAG}} \div 10$ (Figure B.5B) and $\nu_{\mathrm{VOAG}} \div 100$ (Figure B.5C), respectively. The latter frequency is useful because it has a working period of approximately 10 ms. In this

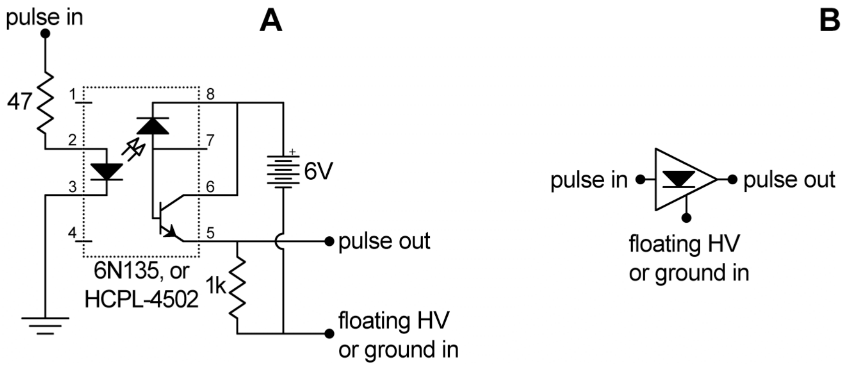

Figure B.4. Schematic diagram of the optoisolator circuit (A). All resistances are in ohms. Frame (B) shows a shorthand notation for this circuit used in other schematics.

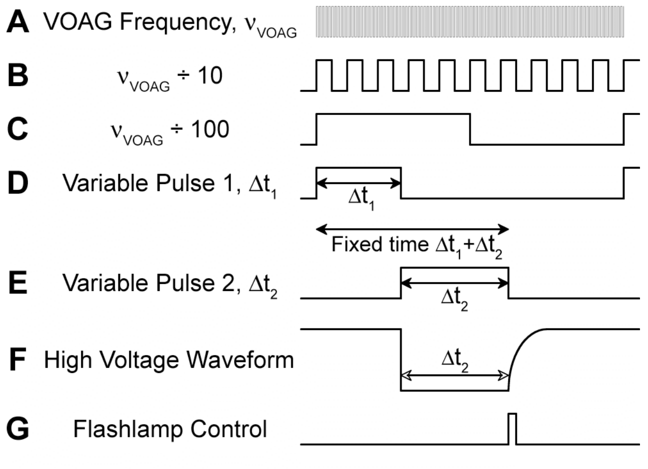

Figure B.5. Pulse sequence for the electronics in the dynamics experiment.

time, the high voltage electronics have plenty of time to switch on, establish a high electric field, switch off, and reset before another period begins.

Two timing pulses set the duration of the high voltage pulse. As shown in Figure B.5D and E, the length of these pulses is variable but the sum of their time lengths remains constant. The high voltage waveform (Figure B.5F) mirrors the second variable pulse, and the flashlamp (Figure B.5G) triggers on the downswing of the second variable pulse, or at the end of Δt_2. In this configuration the timescale of the high voltage waveform is variable, however it always ends at the same time relative to the VOAG frequencies. As a result, the flashlamp always fires in phase with the VOAG, and droplets are repeatedly visualized at a consistent physical location in space.

Figure B.6 shows a schematic diagram of the synchronization circuitry. The VOAG signal is directed into a series of two decade counters to generate the $\nu_{\mathrm{VOAG}} \div 100$ signal in Figure B.5C. A 50 Ω resistor provides a low input impedance to match the output of the PENTEK. The $\nu_{\mathrm{VOAG}} \div 100$ triggers two monostable vibrators in a single 74LS123 integrated circuit that generate the two variable pulses of Figure B.5D and E. Each pulse length Δt is cRC where R is an input resistance, C is an input capacitance, and c is a proportionality constant of the integrated circuit. For the two vibrators, the capacitors are each matched at 23 nF and one common 100 kΩ potentiometer (pot) sets the resistance. The variable connection to the pot is set at 5V and each terminal is connected to a vibrator; thus the variable connection changes the individual resistance however the total resistance remains constant. Since $\Delta t_1 = c\mathrm{R}_1\mathrm{C}_1$, $\Delta t_2 = c\mathrm{R}_2\mathrm{C}_2$, and $\mathrm{C}_1 = \mathrm{C}_2 \equiv \mathrm{C}$; $\Delta t_1 + \Delta t_2 = c\mathrm{C}(\mathrm{R}_1 + \mathrm{R}_2) = constant$ because $\mathrm{R}_1 + \mathrm{R}_2 = 100\mathrm{k}\Omega$. The second

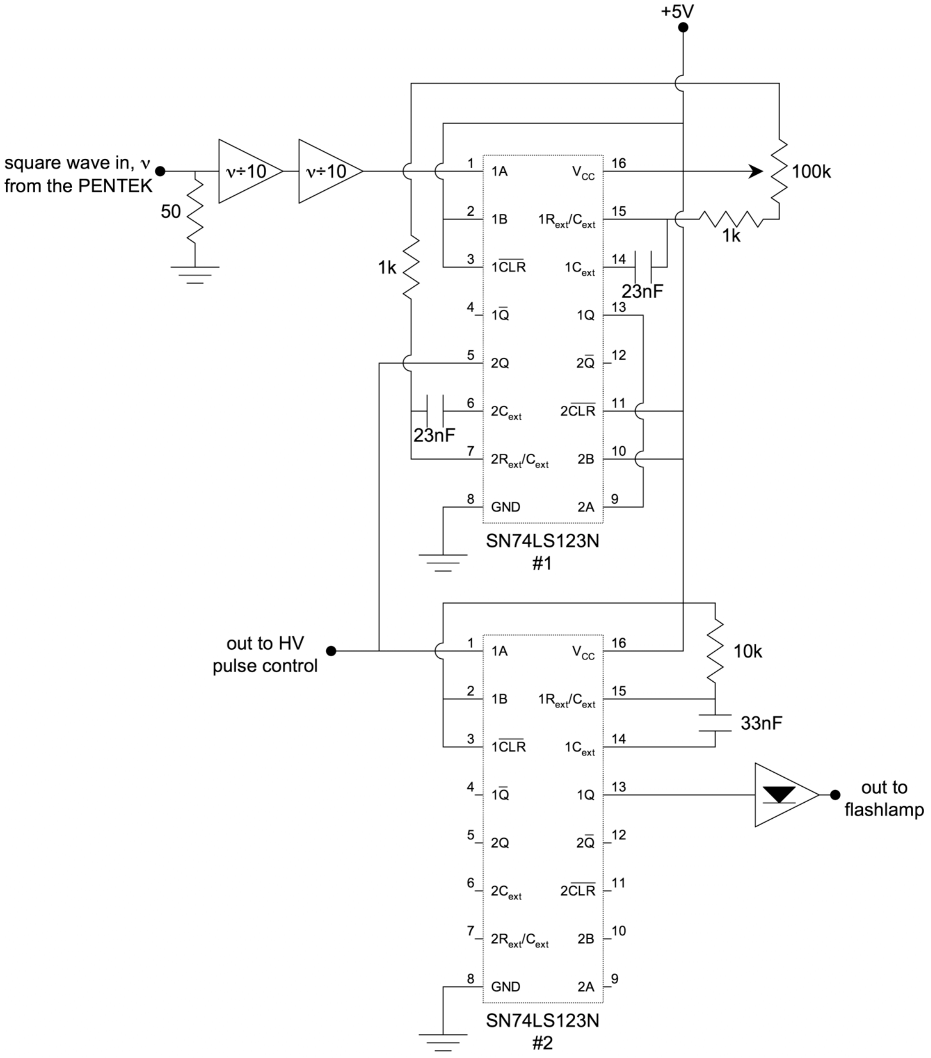

Figure B.6. Schematic diagram of the timing circuitry for the dynamics experiment. The VOAG square wave passes through two decade counters and triggers the 74LS123 monostable vibrators. The vibrators generate output pulses for the high voltage switch and the flashamp.

vibrator generates the control pulse for the high voltage switch discussed in the next section.

The second 74LS123 (#2 in Figure B.6) generates the flashlamp trigger based on the downswing or the end of the high voltage control pulse. The output signal from this vibrator passes through an optoisolator because the flashlamp generates significant electrical noise.

B.3.3. High voltage switching

Figure B.7 shows a schematic of the high voltage pulsing circuit. The HV pulse control from Figure B.6 is sent to four optoisolators. This signal passes through a single Schmitt trigger then breaks into four parallel signals that each pass through a second Schmitt trigger before controlling the optoisolators. In this configuration, the optoisolator driving current comes from the Schmitt triggers rather than the control pulse, and this provides convenient test points for circuit debugging.

Each optoisolator drives a single high voltage MTP1N100E 1kV switching MOSFET. The MOSFETS stack parallel to a chain of 4.7 MΩ resistors. The resistor network at the top of the figure consists of nine parallel 4.7 MΩ resistors in series with ten parallel 4.7 MΩ resistors. This arrangement provides an overall resistance of 1 MΩ, but the voltage drop across individual resistors is less than their 1 Watt rated power. The resistor chain configuration means that the maximum source-drain voltage is only $4.7 / (4.7 \times 4 + 1)$ or ~24% of the total voltage supplied. With a 4kV maximum input voltage provides a maximum switching peak-to-peak pulse of $(4.7 \times 4) / (4.7 \times 4 + 1)$ or ~3800 Volts.

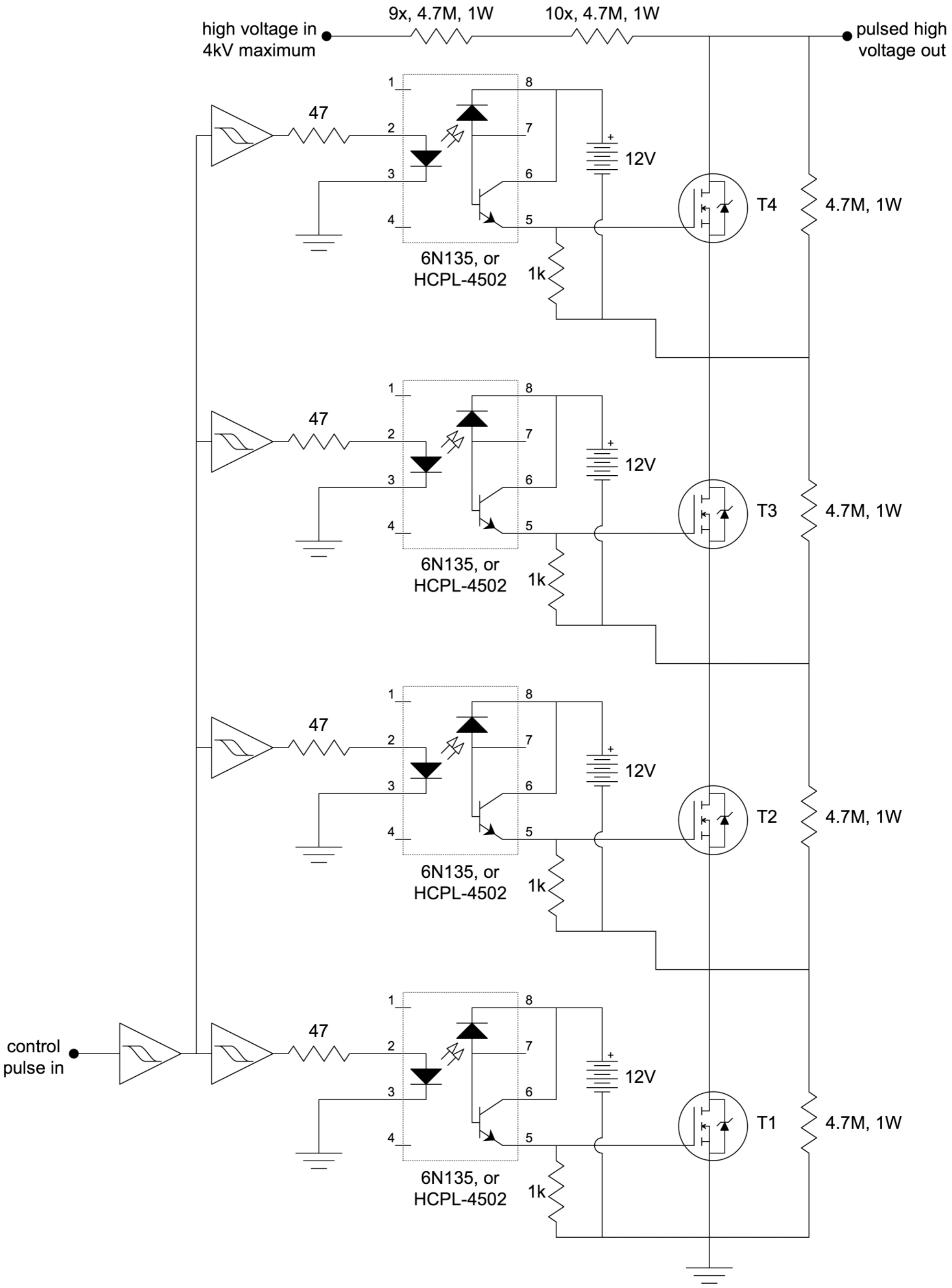

Figure B.7. High voltage pulsing circuit. A control pulse is sent to four optoisolators which each drive a high voltage MOSFET.

B.4. Conclusions and design considerations for future dynamics and FIDI-MS experiments

The FIDI dynamics experiment investigated the dynamics of FIDI using switched high electric fields to enable time-resolved studies of droplet distortion, Taylor cone formation, and charged progeny droplet extraction from neutral and charged 225 micron methanol droplets. Future work may explore this phenomenon on a wider range of solvents and droplet sizes considering the effect of analytes and binary solutions. Additionally, we noted a relationship between the timescale of FIDI and the frequency of shape oscillations that occur below the Taylor limit. We explored this relationship through a single droplet oscillation period which future work may investigate over a longer timescale.

B.5. References

(1) Grimm, R. L.; Beauchamp, J. L. *J. Phys. Chem. B* **2005**, *109*, 8244.

(2) Chen, B. T.; John, W. Instrument Calibration. In *Aerosol Measurement: Principles, Techniques, and Applications*; Baron, P. A., Willeke, K., Eds.; Wiley-Interscience: New York, 2001; pp 627.